

ALMA MATER STUDIORUM  
UNIVERSITÀ DEGLI STUDI DI BOLOGNA

---

---

Dipartimento di Fisica e Astronomia

Dottorato di ricerca in Astronomia  
Ciclo XXVIII

Tesi di Dottorato

**KINEMATICS OF LOCAL AND HIGH-Z GALAXIES  
THROUGH 3D MODELING OF EMISSION-LINE DATACUBES**

CANDIDATO:

Enrico Maria Di Teodoro

RELATORE:

Filippo Fraternali

COORDINATORE:

Lauro Moscardini

Esame finale anno 2015

---

Settore concorsuale: 02/C1 – Astronomia, Astrofisica, Fisica della Terra e dei Pianeti  
Settore scientifico-disciplinare: FIS/05 – Astronomia e Astrofisica



# Contents

<b>Contents</b>	<b>iii</b>
<b>1 Introduction</b>	<b>1</b>
1.1 Historical background . . . . .	1
1.2 Gas kinematics of disk galaxies . . . . .	4
1.2.1 Low-redshift galaxies . . . . .	4
1.2.2 High-redshift galaxies . . . . .	7
1.3 The distribution of matter and the mass decomposition . . . . .	9
1.4 Tully-Fisher relations . . . . .	13
1.5 A short evolutionary picture of disk galaxies . . . . .	15
1.5.1 Gas accretion . . . . .	16
1.6 Brief outline of this thesis . . . . .	19
<b>2 <sup>3D</sup>BAROLO: a software for galaxy kinematics</b>	<b>21</b>
2.1 Emission-line observations . . . . .	22
2.2 The derivation of rotation curves: the tilted-ring model . . . . .	25
2.2.1 Tilted-ring model on velocity fields . . . . .	27
2.2.2 Tilted-ring model on data-cubes . . . . .	29
2.3 The beam smearing effect . . . . .	30
2.4 <sup>3D</sup> BAROLO: the fitting algorithm . . . . .	32
2.4.1 Disk model . . . . .	34
2.4.2 Convolution . . . . .	35
2.4.3 Normalization of the surface density . . . . .	36
2.4.4 Residuals . . . . .	37
2.5 <sup>3D</sup> BAROLO: additional features . . . . .	37
2.5.1 Source finder . . . . .	38
2.5.2 Estimates of the initial parameters . . . . .	40
2.5.3 Masking . . . . .	41

2.5.4	Regularization of the parameters . . . . .	42
2.5.5	Errors . . . . .	42
2.6	Running <sup>3D</sup> BAROLO . . . . .	43
<b>3</b>	<b>HI kinematics of local galaxies</b>	<b>47</b>
3.1	High-resolution data . . . . .	48
3.2	Mid-low resolution data and robustness . . . . .	50
3.3	Very low-resolution data . . . . .	61
3.4	Testing <sup>3D</sup> BAROLO's limits . . . . .	64
<b>4</b>	<b>Gas accretion from minor mergers in local spiral galaxies</b>	<b>69</b>
4.1	Method . . . . .	71
4.1.1	Searching for sources and background statistics . . . . .	71
4.1.2	Accretion and star formation rate estimates . . . . .	72
4.1.3	Major/minor mergers and mass estimates . . . . .	74
4.2	The HI data sample . . . . .	75
4.3	Results . . . . .	77
4.4	Discussion . . . . .	82
4.4.1	Uncertainties . . . . .	82
4.4.2	Comparison to other estimates . . . . .	83
4.4.3	Merger fraction . . . . .	84
4.4.4	Other channels for gas accretion . . . . .	86
4.5	Conclusions and future prospects . . . . .	86
<b>5</b>	<b>Kinematics of high-z galaxies</b>	<b>97</b>
5.1	Data sample . . . . .	99
5.2	Kinematic modeling . . . . .	103
5.3	Results . . . . .	104
<b>6</b>	<b>Concluding remarks and future prospects</b>	<b>111</b>
6.1	Summary . . . . .	111
6.2	Outlook . . . . .	113
	<b>Bibliography</b>	<b>115</b>
	<b>List of Figures and Tables</b>	<b>127</b>

# Chapter 1

---

## Introduction

### 1.1 Historical background

The rotation of galaxies was first observed in the early XX century by Wolf (1914) and Slipher (1914) using stellar absorption lines in the central regions of M81 and M104, respectively. At that time, galaxies were still called “nebulae” and considered as part of the Milky Way. The first *rotation curve*, intended as a plot of the radial velocity as a function of the radius, appeared in 1918 in a study by Pease (1918) on the Andromeda galaxy M31 (Figure 1.1). The variation of the measured stellar velocities along the major axis, compared to the constancy of velocities along the minor axis, was interpreted as a clear sign of the rotation of Andromeda. Emission-lines from HII regions, such as the Balmer series and [OIII] lines, were later used to trace rotation velocities (e.g., Babcock, 1939; Mayall & Aller, 1942), but the detection of these lines required exposure times of several tens of hours.

Babcock (1939) and Oort (1940) first noted that the rotation curves of M31 and NGC3115, respectively, have a different shape than predicted from the observed light distribution, suggesting a growth of the mass-to-light ratio ( $M/L$ ) or an unlikely increase of the dust attenuation with radius. The hypothesis of a large amount of unseen or undetectable matter that does not interact with radiation, hence called “dark matter” (DM), had already been postulated by Oort (1932), based on the or-

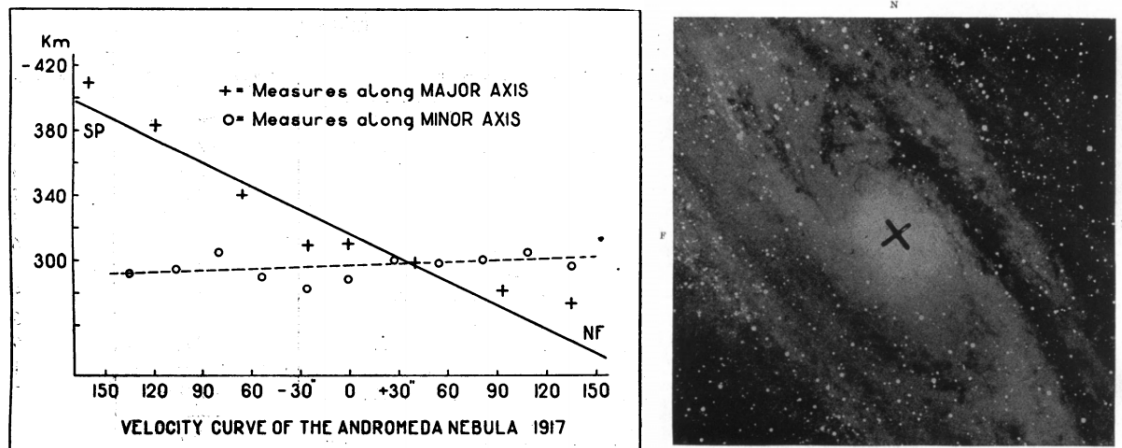


**Figure 1.1:** *Left:* observed radial velocities in the inner regions of M31 obtained with absorption-line stellar spectra taken along the major (crosses) and minor axis (circles). *Right:* diagram showing the length and the position of the slits on an optical image of M31. Both figures are from Pease (1918).

bit velocities of stars in the solar neighborhood, and by Zwicky (1933), on the basis of the virial theorem applied to the Coma cluster. The idea of a massive dark matter component in the outer regions of galaxy disks started to spread in the 1970s as the increasing amount of available optical data confirmed that the rotation curves of most spiral galaxies remain flat and show no signs of the expected Keplerian decline out to very large distances from the galaxy centers (Freeman, 1970; Einasto et al., 1974; Rubin, Thonnard & Ford, 1978). In the same years, the presence of spherical and massive haloes embedding spiral galaxies was postulated by Ostriker & Peebles (1973) to explain the survival of stellar disks to bar instabilities. However, Kalnajs (1983) and Kent (1986) showed that the flatness of optical rotation curves can be entirely reproduced by the distribution of luminous matter by assuming appropriate mass-to-light ratios for bulge and disk, without the need of any additional DM component. Optical rotation curves were therefore not extended enough to firmly establish the presence of dark matter and to study its distribution.

The discovery of the emission-line of neutral hydrogen (HI) at 21-cm wavelength, theoretically predicted by the Oort's student H. van de Hulst in 1944 and first observed by Ewen & Purcell (1951), opened up new possibilities for the study of the kinematics of galaxies. The pioneering HI single-dish observations of M31 by van de Hulst, Raimond & van Woerden (1957) and Argyle (1965) and the following advent of radio-interferometers (e.g., Rogstad & Shostak, 1971; Allen, Goss, & van Woerden, 1973) allowed the derivation of spatially resolved rotation curves and the study of the mass distribution and the related gravitational potential out to very large radii (see Section 1.3). Indeed most stars and gas in spiral galaxies are confined in thin disk-like structures, but neutral hydrogen usually extends much

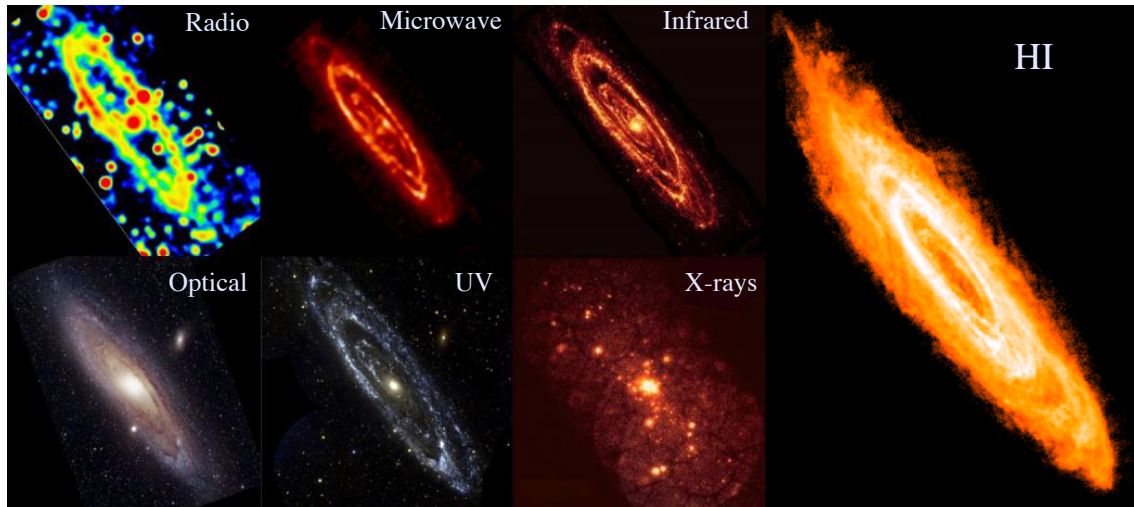


**Figure 1.2:** The Andromeda galaxy (M31) observed at different wavelengths, from radio to X-ray bands. All images have the same spatial scale. The 21-cm emission of the neutral hydrogen (HI) extends about twice farther out than the other baryonic components (e.g., stars, dust and ionized gas) traced by other wavelengths. Image credits: ESA/NASA.

farther out than the stellar disk, making the HI-line a unique tool to trace the large-scale kinematics of galaxies (Figure 1.2). Studies of the kinematics of the neutral gas (e.g., Rogstad & Shostak, 1972; Bosma, 1978; van Albada et al., 1985) have shown how the rotation curves of almost all spiral galaxies stay flat beyond the optical disks out to the last measured point. This constant rotation velocity suggested that the mass increases linearly with radius (see Section 1.3), while the stellar light is observed to fall off exponentially. This evidence led to the now widely accepted idea that spiral galaxies are dominated by dark matter at large radii, even though alternative possibilities, like modified gravity theories (e.g. MOND, Milgrom, 1983), have been proposed. Overall, studies on the rotation curves have largely improved our understanding of the internal dynamical structure and the distribution of matter in galaxies, allowing us to characterize the DM haloes (e.g. their mass density profiles and their gravitational potential) and having a big influence in drawing the current cosmological picture of galaxy formation and evolution.

Modern cosmology is based on the “cold dark matter” (CDM) scenario of structure formation, where DM particles are “cold” in the sense that they move at sub-relativistic velocities. According to this theory, which has its roots in the early works of Peebles (1982), Blumenthal, Pagels & Primack (1982) and Bond, Szalay & Turner (1982), structures formed by the gravitational growth of small density fluctuations, of the order of  $10^{-5}$ , in the primordial Universe. Baryonic and dark matter condensed in regions of higher densities and formed spherical halos that are the seeds of proto-galaxies (Blumenthal et al., 1984). When halos became sufficiently massive, they collapsed under their own gravity and the first generation of stars emerged out

of the central dense gas (see [Section 1.5](#)). Halos successively grew through the continuous merging of smaller structures in a hierarchical process that assembled larger and larger galaxies. The  $\Lambda$ CDM model, i.e. the CDM scenario with an hypothetical force  $\Lambda$  added to account for the accelerated expansion of the Universe (Riess et al., 1998; Perlmutter et al., 1999), is today referred to as the “standard cosmological model”.

In the following Sections, we introduce the astrophysical concepts and problems relevant to this thesis. In [Section 1.2](#), we first review some kinematic properties of star-forming galaxies<sup>1</sup> in the local Universe and then we move to the current view of the kinematics of high-redshift galaxies ( $z > 0.5$ ). In [Section 1.3](#) and [Section 1.4](#), we introduce the two most important fields of application of rotation curves, namely the mass decomposition and the derivation of the Tully-Fisher relation. In [Section 1.5](#) we briefly draw our current understanding of the evolution of disk galaxies, focusing in particular on the problem of gas accretion. A brief outline of this thesis is finally given in [Section 1.6](#).

## 1.2 Gas kinematics of disk galaxies

In this Section, we describe the fundamental kinematic properties of the gaseous components of disk galaxies both in the local and in the high- $z$  Universe. In particular, we focus on their rotation velocity and gas velocity dispersion, which constitute the observable quantities and the basis of any interpretation of their dynamical structure. Whereas local star-forming galaxies show in general well defined kinematic patterns, galaxies at high redshift appear to have a wider kinematic diversity (Glazebrook, 2013). Some seem not dominated by rotation, others have kinematic signatures of on-going mergers. However, how much these diversities are caused by observational biases is yet to be established. Moreover, the evolutionary paths from high- $z$  to low- $z$  disk galaxies are still under investigation.

### 1.2.1 Low-redshift galaxies

Galaxies can be broadly classified in two different types, commonly referred to as the “red sequence” and the “blue cloud” (Strateva et al., 2001; Baldry et al., 2004). This bimodality strongly correlates with galaxy morphology: red-sequence objects are early-type galaxies (ETGs), elliptically shaped, mostly dust and gas free and dominated by an old and red stellar population, whereas blue-cloud objects are late-type galaxies (LTGs), with disk-like structures, spiral arms, gas and dust rich,

---

<sup>1</sup>In this thesis we will use the term “star-forming” galaxy to indicate an object belonging to the population of spiral galaxies or dwarf irregular galaxies. We will also use the terms “spiral” and “disk” galaxy interchangeably.

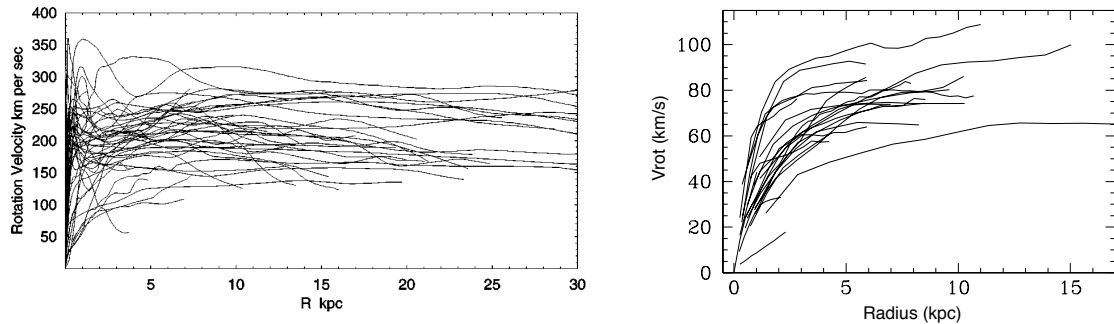


**Figure 1.3:** Rotation curves of several star-forming galaxies in the local Universe. *Left:* rotation curves of spiral galaxies taken from the review of Sofue & Rubin (2001). These curves have been obtained through CO observations in the inner rising regions, optical observations across the stellar disk and HI observations in the outer regions. *Right:* HI rotation curves of a sample of dwarf galaxies from Swaters (1999).

with both old and young stellar populations. In the local Universe, this correlation is so strong that almost every galaxy belonging to the blue cloud is a star-forming rotating disk, even though there is also an uncommon population of redder spirals, belonging to the so-called “green valley” (Martin et al., 2007; Wyder et al., 2007), where the star formation appears to be *quenched*.

Most baryonic matter in spiral galaxies is confined in disk-like structures, where gas and stars approximately move in circular orbits (e.g., Franx & de Zeeuw, 1992) about the galaxy center. The dynamics of spiral galaxies is largely dominated by rotation and the typical  $V/\sigma$  ratio, which is a measure of the relative importance of ordered ( $V$ ) and random ( $\sigma$ ) motions in the dynamical support of galaxies, is larger than 5-10. The rotation in the plane of the disk can vary from a *solid-body-like pattern*, i.e. the orbital velocity linearly increases with radius and the orbital period is constant, to a *differential rotation*, i.e. the orbital velocity is nearly constant and the orbital period increases with radius. The shape of the rotation curves of local galaxies has been found to correlate with the disk surface density (Mo, Mao & White, 1998; Firmani & Avila-Reese, 2000). In particular, rotation curves can be broadly classified in two categories (e.g. Casertano & van Gorkom, 1991), corresponding to galaxies with high surface brightness (HSB) and low surface brightness (LSB, central  $B$ -band surface brightness  $\mu(B) \gtrsim 22 \text{ mag/arcsec}^2$ ). HSBs are usually large and massive spiral galaxies, whereas LSBs roughly correspond to the population of low-mass star-forming dwarf galaxies. HSBs typically show a steeply-rising solid-body rotation curve in the innermost regions followed by a flat part, that usually remains constant out to large radii in low-luminosity spiral galaxies or slowly declines and then flattens in more luminous galaxies (Sofue & Rubin, 2001). LSBs instead have slowly-rising solid-body rotation curves that may reach a flat part or just keep rising

with radius (Swaters, 1999). Typical rotation curves of nearby HSB and LSB star-forming galaxies are shown in Figure 1.3. The former are believed to be dominated by baryons in the inner regions and by DM in the outer parts (see Section 1.3). The latter are thought to be DM-dominated at all radii and they have been used to constrain the inner slope of the density profile of the DM halos (leading to the so-called “cusps vs cores controversy”, e.g. Kuzio de Naray, McGaugh & de Blok, 2008; van Eymeren et al., 2009).

The velocity dispersion is the second key observable to investigate the dynamical state of the galactic disks. The intrinsic velocity dispersion of the gaseous component  $\sigma_{\text{gas}}$  includes both the contribution of the thermal broadening  $\sigma_{\text{th}}$  and the *turbulent* broadening due to internal chaotic motions  $\sigma_{\text{turb}}$ , which can be added in quadrature  $\sigma_{\text{gas}}^2 = \sigma_{\text{th}}^2 + \sigma_{\text{turb}}^2$ . Studies of the velocity dispersion of neutral hydrogen in spiral galaxies have found values of  $\sigma_{\text{HI}} \simeq 8 - 20 \text{ km s}^{-1}$  (e.g., van der Kruit & Shostak, 1982; van Zee & Bryant, 1999), with a contribution from thermal motions of  $\sigma_{\text{th}} \simeq (2kT/m_{\text{H}})^{1/2} \sim 1 - 8 \text{ km s}^{-1}$  for a gas at  $T \simeq 100 - 8000 \text{ K}$  ( $k =$  Boltzmann constant,  $m_{\text{H}} =$  proton mass). The observed  $\sigma_{\text{HI}}$  is, in general, not compatible with only thermal broadening and a significant non-thermal (turbulent) contribution is needed. The values of velocity dispersion are quite uniform across different spiral galaxies in the local Universe (Tamburro et al., 2009), suggesting a common mechanism to feed the turbulence of the interstellar medium (ISM). Proposed energy sources are the feedback from massive stars, such as winds and supernova explosions (e.g., Dib, Bell & Burkert, 2006; Joung & Mac Low, 2006), gravitational instabilities due to spiral arms (e.g., Elmegreen, Elmegreen & Leitner, 2003), magneto-rotational (e.g., Dziourkevitch, Elstner & Rüdiger, 2004) or thermal instabilities (e.g., Hennebelle & Audit, 2007).

Other gas components have  $\sigma_{\text{gas}}$  different from that of the HI gas. For instance, the velocity dispersion of the molecular gas, measured through the CO lines, is  $3\text{--}6 \text{ km s}^{-1}$  (e.g., Wilson et al., 2011). The ionized medium is mainly observed through the recombination  $\text{H}\alpha$ -line at  $6563 \text{ \AA}$ , whose emission is usually dominated by HII regions and traces the recent star formation. Studies of the  $\text{H}\alpha$  velocity dispersion in local galaxies revealed  $\sigma_{\text{H}\alpha} \sim 25 - 30 \text{ km s}^{-1}$  (e.g., Andersen et al., 2006; Epinat et al., 2010), again a value inconsistent with the thermal broadening of the order of  $12 \text{ km s}^{-1}$  at the typical temperature of  $T \simeq 10^4 \text{ K}$ . Also in this case, an important contribution from turbulent motions in HII regions of about  $20\text{--}25 \text{ km s}^{-1}$  is required (Shields, 1990).

The velocity dispersion  $\sigma$  of the disk component in spiral galaxies is also related to its vertical structure through the hydrostatic equilibrium. Local spiral galaxies usually show two disk components: a thin and a thick disk (Figure 1.4, right). The thin disk includes most of the young stars, gas and dust. This is where all star formation currently takes place. In Milky-Way-like galaxies, the young stellar

component has a typical scale-height  $h_z \sim 200 - 300$  pc and  $\sigma_z \sim 20 - 30$  km s<sup>-1</sup> (e.g., Martinsson et al., 2013). The neutral gas has velocity dispersions of about 10 km s<sup>-1</sup> and scale-height of 100 – 150 pc, whereas molecular gas has  $h_z \lesssim 80$  pc. The thick disk is mostly formed by an old stellar population (e.g., Chiba & Beers, 2000; Comerón et al., 2011) and has an exponential scale-height  $h_z \sim 1000 - 1500$  pc, corresponding to a vertical velocity dispersion of  $\sigma_z \sim 40 - 50$  km s<sup>-1</sup>. The origin of thick disks is still debated and a number of formation mechanisms have been proposed, such as merger events or secular evolution (van der Kruit & Freeman, 2011).

### 1.2.2 High-redshift galaxies

The structure and the kinematics of high- $z$  star-forming galaxies are still highly uncertain due to the poor resolution and sensitivity of the data. The detection of stellar absorption lines in high- $z$  galaxies is challenging and the HI line can not be observed because most of the current radio telescopes have not enough sensitivity and/or can not operate at the frequencies corresponding to the redshifted HI line. Therefore, one must resort to different tracers. Most studies at high redshift make use of CO observations of molecular gas or Integral Field Spectroscopy (IFS) observations of optical/IR recombination lines, in particular the H $\alpha$ -line, tracing the warm ionized gas component.

On average, high- $z$  systems have been observed to have higher molecular gas fractions and star formation rates than local galaxies (e.g., Tacconi et al., 2010, 2013) and they often show a larger variety of kinematics. Several studies have attempted to classify these galaxies in kinematic categories, such as rotating disks, perturbed rotators, dispersion dominated systems, complex kinematics due to mergers, but the actual fraction of each kinematic type is debated. In particular, the fraction of rotating disks seems to rise as the quality and the spatial resolution of the observations improves, moving from an initial value of  $\sim 30\%$  (Genzel et al., 2006; Förster Schreiber et al., 2006, e.g.) to more than 80% (e.g., Wisnioski et al., 2015). Moreover, Newman et al. (2013), comparing an extended sample of galaxies observed with adaptive optics (AO) to a non-AO sample, found that the fraction of dispersion-dominated galaxies dramatically drops as the spatial resolution increases. This evidence suggests that these classifications are strongly biased by instrumental effects, in particular by the so-called “beam smearing” (see Section 2.3).

Rotation velocities measured in high- $z$  disks are in the range 100 – 300 km s<sup>-1</sup> (e.g., Cresci et al., 2009; Gnerucci et al., 2011), similarly to the rotation of local spiral galaxies (see Figure 1.3, left). Measured H $\alpha$  velocity dispersions are instead unexpectedly high, ranging from 50 km s<sup>-1</sup> to more than 100 km s<sup>-1</sup> (e.g., Genzel et al., 2008; Förster Schreiber et al., 2009; Law et al., 2009), a factor 2-4 higher than local disks, and showing an increasing trend with redshift. If this dispersion is a

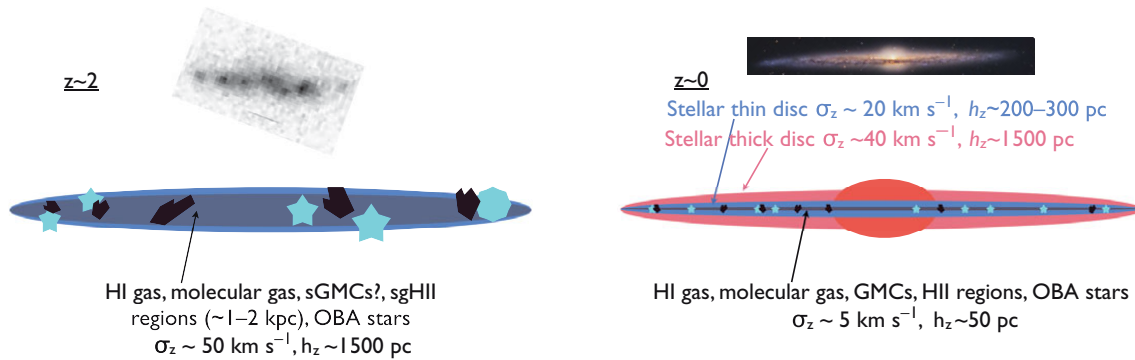


**Figure 1.4:** This illustrative sketch shows the different structures of high- $z$  (*left*) and low- $z$  (*right*) disk galaxies in an edge-on perspective, from Glazebrook (2013). High-redshift disks are believed to be thick ( $\sim 1$  kpc scale-height) and highly turbulent, made by high fractions of molecular gas, young stars, super-Giant HII regions (clumps of star formation with kpc scales) and possibly super-Giant Molecular Clouds. Local spiral galaxies typically show a stellar thick disk and a thin disk, containing young stars, molecular and neutral gas, HII regions and Giant Molecular Clouds.

measure of the gas turbulence, then a strong energy source is needed. A number of physical processes have been advocated to explain these high velocity dispersions, like cosmic gas accretion, highly effective star-formation feedback and clump formation (e.g., Green et al., 2010). On the other hand, there may still be residual instrumental effects due to the low spatial resolution of the data (see Section 2.3). The evolution of velocity dispersions with redshift is often interpreted as an evolution of the disk stability, related to the evolution of galaxy properties like gas fractions, gas depletion times and star formation rates (e.g., Genzel et al., 2014; Wisnioski et al., 2015).

Although a number of uncertainties still persist, the general picture is that early disks were morphologically different and dynamically hotter than present-day galaxies, with decreasing  $V/\sigma$  with time. A schematic comparison between disks at low and high redshift is shown in Figure 1.4. Turbulent and thick ( $h_z \sim 1000 - 2000$  pc) high- $z$  disks (*left* sketch), with high fraction of molecular gas and giant clumps of star formation, evolved into low- $z$  disks (*right* sketch), made by a thin (gas, dust and young stars) and a thick disk component (old stars). The evolutionary paths from high- $z$  disks to the dynamically cooler galaxies of today are anything but obvious. A suggestive scenario proposed by Bournaud, Elmegreen & Martig (2009) is that early gas-rich high-dispersion disks evolve into the thick disk of local galaxies, which would have been therefore formed *in situ* and not by accretion of satellites or secular evolution.

### 1.3 The distribution of matter and the mass decomposition

The study of the disk gas kinematics is one of the most powerful tools to unveil the dynamical structure of spiral galaxies. The mass distribution and the gravitational potential can be inferred by decomposing the observed rotation curve  $V_{\text{rot}}(R)$  into the contribution given by the different matter components in a galaxy, i.e. gas, stars and dark matter (e.g. van Albada et al., 1985). Assuming axial symmetry, from the centrifugal equilibrium we have:

$$V_c^2(R) = -R \left( \frac{\partial \Phi(R, z)}{\partial R} \right)_{z=0} \quad (1.1)$$

where  $\Phi$  is the gravitational potential and  $V_c(R)$  is the circular velocity at radius  $R$  in the plane of the disk ( $z = 0$ ). In this thesis, we will use the circular velocity  $V_c$  as a measure of the potential. In contrast, the observed rotation velocity will be referred to as  $V_{\text{rot}}$ . In rotation-dominated systems, like local spiral galaxies with  $V/\sigma > 5 - 6$ , the pressure support due to random motions is negligible compared to the rotation support and  $V_c \simeq V_{\text{rot}}$ . In galaxies with lower  $V/\sigma$ , like dwarf galaxies, a correction for pressure support must be taken into account (*asymmetric drift*) and  $V_c^2 \simeq V_{\text{rot}}^2 + \sigma_D^2$ . This asymmetric drift correction  $\sigma_D$  depends on the partial derivatives with respect to the radius of both the surface density and the velocity dispersion of the tracing gaseous or stellar component (e.g., Meurer et al., 1996). For HI gas, this correction is usually neglected.

The rotation velocity  $V_{\text{rot}}$  can be decomposed into the contribution of the three main mass components and it can be written as:

$$V_{\text{rot}}^2(R) = V_g^2(R) + \Upsilon_* V_*^2(R) + V_{\text{DM}}^2(R) \quad (1.2)$$

where  $V_*$ ,  $V_g$  and  $V_{\text{DM}}$  are the rotation velocities of the stars, the gas and the dark matter halo, respectively. In Equation 1.2 the stellar mass-to-light ratio  $\Upsilon_* \equiv M_*/L_*$  has been introduced as we can only measure the distribution of the light of the stellar component, rather than the required mass. Instead, the mass of the gas, HI in particular, can be directly estimated from the observed flux under the assumption of negligible optical thickness. Once we have  $V_g$  and  $V_*$ , the rotation velocity and the shape of the potential of the dark matter halo can be derived through a fit of Equation 1.2 to the observed rotation curve  $V_{\text{rot}}$ .

The gas and the stellar component are usually assumed to be confined in a disk structure. A spherical component for galaxies with prominent bulges can be additionally considered for stars in the central regions. For an exponential disk with surface mass-density  $\Sigma(R) = \Sigma_0 \exp(-R/R_d)$ , being  $\Sigma_0$  the central surface density and  $R_d$  the disk scalelength, the circular speed can be written as (Freeman, 1970):

$$V_d^2(R) = 4\pi G \Sigma_0 R_d y^2 [I_0(y)K_0(y) - I_1(y)K_1(y)] \quad (1.3)$$

where  $y = 0.5R/R_d$ ,  $K_n$  and  $I_n$  are modified Bessel functions. This rotation curve rises from the center out to the maximum value of  $V_{\max} \simeq 0.88(\pi G R_d \Sigma_0)^{1/2}$  at a radius  $R = 2.2R_d$  and then declines, slowly approaching a Keplerian fall. For the stellar component, the surface density is derived from the surface brightness profile, assuming or fitting an appropriate mass-to-light ratio  $\Upsilon_*$ . For the gas component, the surface density can be directly derived from the HI observations. The  $\Sigma_{\text{HI}}$  is usually multiplied by a factor 1.3-1.4 to take into account a contribution of helium to the gas mass. When available, CO observations can be added to trace the contribution of molecular gas, whereas the ionized gas is usually considered negligible.

The density profile of the dark matter halo have to be assumed *a priori* and then fitted to reproduce the observed rotation curve. Most used DM halos are the isothermal sphere,

$$\rho_{\text{ISO}}(r) = \rho_0 \left[ 1 + \left( \frac{r}{r_C} \right)^2 \right]^{-1} \quad (1.4)$$

where  $\rho_0$  is the central density and  $r_C$  is the core radius of the halo, and the Navarro-Frenk-White halo (NFW, Navarro, Frenk & White, 1996, 1997),

$$\rho_{\text{NFW}}(r) = \frac{\rho_i}{(r/r_s)(1 + r/r_s)^2} \quad (1.5)$$

where  $r_s$  is the characteristic radius of the NFW halo and  $\rho_i$  is related to the density of the Universe at the time of the halo formation. The NFW profile arises from  $N$ -body simulations of structure formation in a CDM cosmology. Both the isothermal and NFW halos are assumed to be spherical, but a correction for the halo flattening can be additionally taken into account. The density profiles (1.4) and (1.5) produce the following contributions to the rotation curve in the plane of the disk (written in cylindrical coordinates), respectively:

$$V_{\text{DM, ISO}}^2(R, z=0) = 4\pi G \rho_0 R_C^2 \left[ 1 - \frac{R_C}{R} \arctan \left( \frac{R}{R_C} \right) \right] \quad (1.6a)$$

$$V_{\text{DM, NFW}}^2(R, z=0) = V_{200}^2 \left[ \frac{\ln(1+cx) - cx/(1+cx)}{x[\ln(1+c) - c/(1+c)]} \right] \quad (1.6b)$$

where  $x = R/R_{200}$ ,  $V_{200}$  is the rotation velocity at  $R_{200}$ , namely the radius inside

which the average density is 200 times the critical density of the Universe, roughly corresponding to the virial radius. The parameter  $c = R_{200}/R_s$  is the halo concentration, inversely proportional to the mass and the redshift, which means that low mass halos at low redshifts have higher concentrations (e.g., Ludlow et al., 2014).

The largest uncertainty in the above-mentioned procedure of mass decomposition lies in the stellar mass-to-light ratio  $\Upsilon_*$ , which scales the stellar velocity by some linear factor (Equation 1.2). This scaling gives rise to a well-known degeneracy between the DM halo parameters and  $\Upsilon_*$  as equally well fitting mass models can be obtained for a wide range of mass-to-light ratios. This degeneracy led van Albada & Sancisi (1986) to introduce the hypothesis of “maximum disks”. The maximum disk assumption maximizes the baryonic contribution by using the maximum value of  $\Upsilon_*$  allowed by the observed rotation curve. On the contrary, a “minimum disk” would minimize the contribution of baryonic matter and maximize that of the dark matter halo. The fit of maximum disks in massive HSB galaxies usually returns mass-to-light ratios that are compatible with stellar-population synthesis models (Bell & de Jong, 2001; Portinari, Sommer-Larsen & Tantalo, 2004), for instance  $\Upsilon_{*,V} \sim 2 - 3$  in the  $V$ -band. Thus, massive disks are possibly “maximal”, i.e. they are dominated by the baryonic component in the inner regions and by the DM halo only in the outer parts. In contrast, a maximum disk fit applied to a LSB galaxy would require unrealistic mass-to-light ratios ( $\Upsilon_{*,V} \gtrsim 10$ ). This evidence suggests that dwarf galaxies with slowly-rising rotation curves must have a dominant contribution by dark matter also in the inner regions. The maximum disk hypothesis has been successfully used to reproduce the inner shapes of rotation curves in several HSB galaxies (e.g., Athanassoula, Bosma & Papaioannou, 1987; Begeman, 1989; Palunas & Williams, 2000). An additional support to the maximum disk hypothesis for massive galaxies comes from the fact that some features in rotation curves have been observed to correspond to features in the luminosity profiles (e.g., Kent, 1986). However, it is not undoubtedly evident that all these disks are maximal and several studies have rather found indications of sub-maximal disks (e.g., Bottema, 1993; Pizagno et al., 2005; Martinsson et al., 2013).

Two examples of rotation curve decompositions taken from de Blok et al. (2008) are shown in Figure 1.5 for the HSB galaxy NGC 3198 (*left panels*) and for the LSB galaxy DDO 154 (*right panels*). The contributions of the gas (*dotted lines*) and stellar (*dashed lines*) disks were derived using high-resolution HI observations and NIR images at  $3.6\mu\text{m}$ , respectively. Mass-to-light ratios were estimated and fixed following the relation with  $(J - K)$  colors by Bell & de Jong (2001). The dark matter haloes (*full lines*), with isothermal (*upper panels*) or NFW density profiles (*lower panels*), were then fitted to match the observed rotation curves. Note that the LSB galaxy has a dominant contribution of the DM halo at every radius, whereas in the HSB galaxy, stars dominate the inner rising region and DM the outer part of the

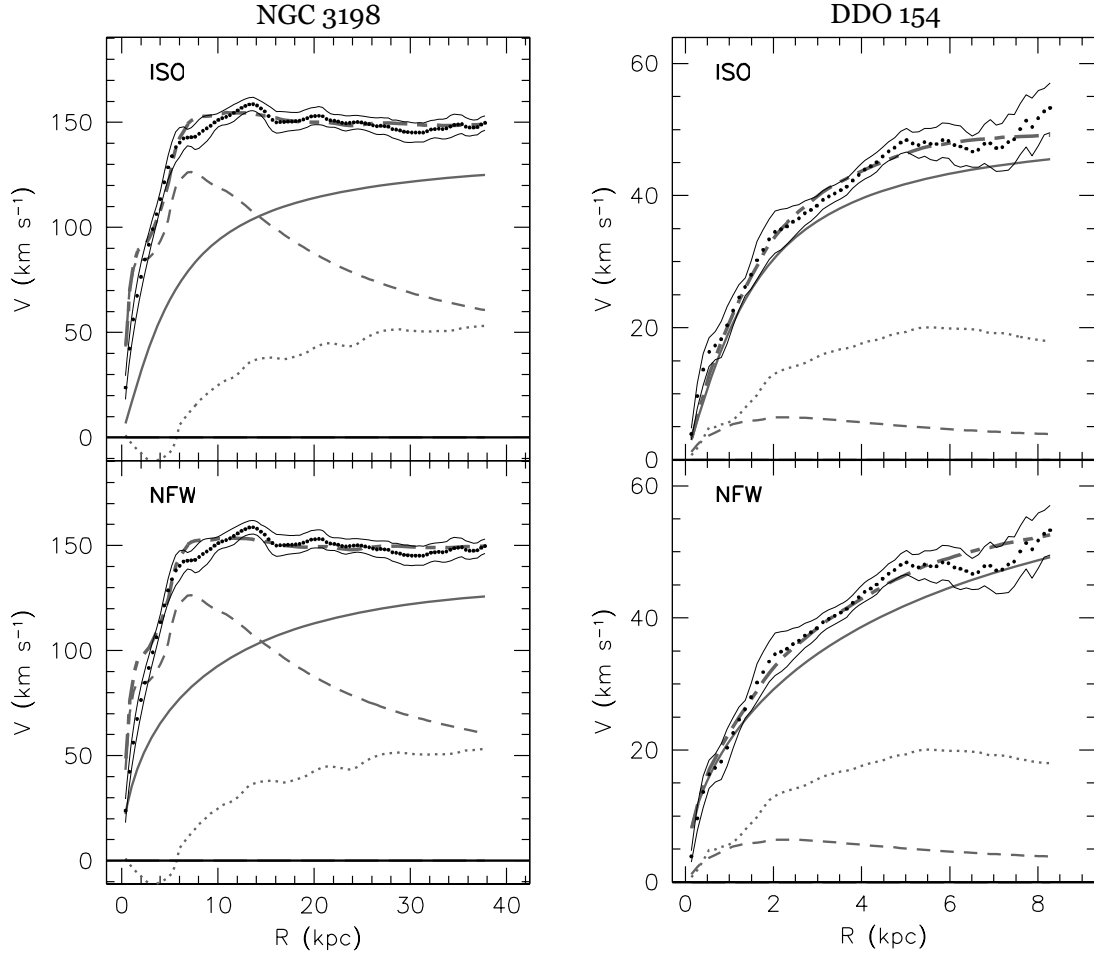


**Figure 1.5:** Rotation curve decompositions for the large spiral galaxy NGC 3198 (*left*) and the dwarf galaxy DDO 154 (*right*). Plots are taken from de Blok et al. (2008). For each galaxy, a fit with the isothermal (*top*) and the NFW (*bottom*) dark matter halo is shown. In all panels black dots represent the observed curve and the thin full lines represent the uncertainties. The gray dotted curve shows the rotation curve of the HI gas  $V_g(R)$  and the thin dashed gray curve shows the rotation curve of the stellar disk  $V_*(R)$  with fixed  $\Upsilon_*$  (see text). Thick, gray full curves show the rotation curve of the halo  $V_{DM}$ . The thick long-short dashed curve shows the best-fit model to the observed rotation curve  $V_{rot}(R)$  from Equation 1.2.

curve. In general, the flatness of the rotation curve in massive spiral galaxies, like NGC 3198, seems to be related to a “lucky” smooth transition between the disk and the halo domination regions (the so-called “disk-halo conspiracy”, e.g. Bahcall & Casertano, 1985). The disk-halo conspiracy is a problem that remains to be satisfactorily solved, even if mechanisms like the adiabatic contraction of the halo when the disk was formed (Blumenthal et al., 1986) are partially able to justify it.

## 1.4 Tully-Fisher relations

The Tully-Fisher relation (TFR) is the fundamental scaling relation for spiral galaxies and it is likely related to the mechanisms of disk assembly. The original relation was proposed between the inclination-corrected width of the global HI line profile  $W_{\text{HI}}^i$  and the absolute magnitude of the galaxy. It was found by Tully & Fisher (1977) using HI observations of a sample of galaxies in the Local Group, the M81 group and the M101 group.

Currently, the TFR is referred to as a correlation between the rotation velocity and the luminosity of a galaxy in the form of a power law:

$$L = AV^\alpha \quad (1.7)$$

where  $A$  is the zero-point and  $\alpha \sim 4$ . The Tully-Fisher relation has been deeply studied in the local Universe, using several determinations for the luminosity in different bands. In particular, it has been observed that the power-law exponent varies from about 3 in the  $B$ -band to 4-4.5 in the  $H$ -band, with a decreasing scatter towards redder/IR filters (Sakai et al., 2000). This is likely due to the fact that the radiation at lower wavelengths is more affected by dust extinction and by ongoing star formation. The rotation velocities can be measured in different ways, e.g. through the inclination-corrected width of the HI global profile  $W_{\text{HI}}^i$ , the maximum rotation velocity  $V_{\text{max}}$  or the velocity of the flat part  $V_{\text{flat}}$  of the rotation curve. Verheijen (2001) found the tightest relation using the  $V_{\text{flat}}$  as a kinematic measure, hence this proxy is preferably used when extended rotation curves are available.

The classical TFR can also be seen as a relation between the dynamical mass (traced by  $V_{\text{rot}}$ ) and the stellar mass  $M_*$ , since stars dominate the bolometric luminosity of disk galaxies. McGaugh et al. (2000) noticed that the classical TFR breaks down for low-mass galaxies ( $V_{\text{rot}} \lesssim 90 \text{ km s}^{-1}$ ), which are underluminous and relatively more gas-rich. However, they found that the relation can be restored by taking into account also the mass of the gas (Figure 1.6). The resulting ‘‘Baryonic TFR’’, i.e.  $M_{\text{b}} = (M_* + M_{\text{gas}})$  vs  $V_{\text{rot}}$ , is a relation that spans over five orders of magnitude in baryonic mass (from about  $10^7$  to  $10^{12} M_{\odot}$ ) with a surprisingly small scatter ( $< 0.25$  dex, McGaugh, 2012).

In the last years, the improvements in the instrumentation suitable to observe high- $z$  galaxies opened up the possibility to study the TFR and its evolution throughout cosmic time. A conspicuous number of high- $z$  studies have been carried out using both long slit and integral field spectroscopy. However, although the low-redshift TFRs are well constrained (e.g., Bell & de Jong, 2001; Meyer et al., 2008; Zaritsky et al., 2014), the TFRs at intermediate/high redshifts are affected by the technical challenges mostly due to the low spatial resolutions. As a result, the relation has a larger scatter and there are discrepant conclusions about its evolutionary trend

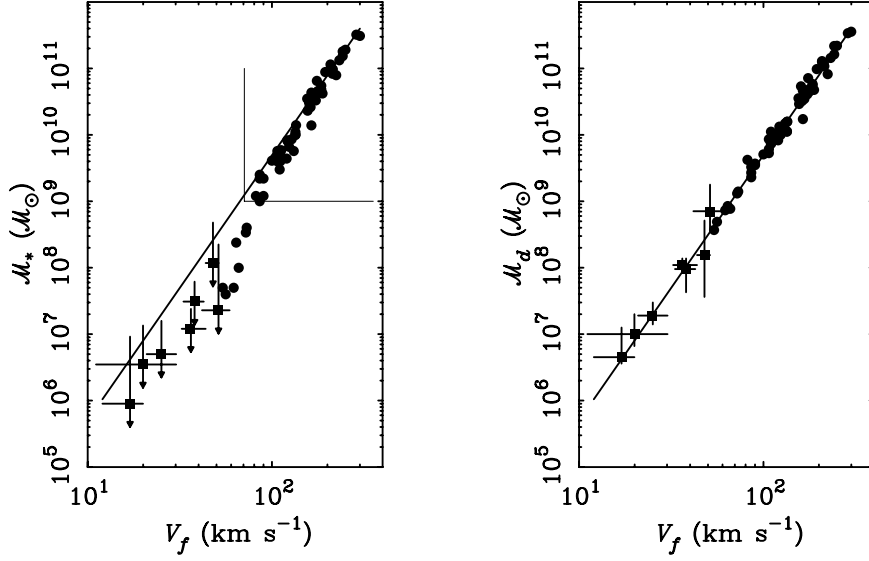


**Figure 1.6:** Stellar mass (*left*) and baryonic (*right*) Tully-Fisher relations from McGaugh (2005). Both TFRs are derived from the same galaxy sample. Dwarf galaxies ( $V_{\text{flat}} < 90 - 100 \text{ km s}^{-1}$ ) follow the linear relation of massive galaxies when the total baryonic mass (stars plus gas) is used instead of the stellar mass.

in the literature: some studies claimed a substantial evolution (e.g., Weiner et al., 2006; Puech et al., 2008), other studies found no convincing evolution (Conselice et al., 2005; Flores et al., 2006; Miller et al., 2012).

The physical origin of the Tully-Fisher relation is still not completely understood, but it is likely based on the dynamical equilibrium of self-gravitating systems. For a small particle of mass  $m$ , like a gas cloud, gravitating with a rotation velocity  $V_{\text{rot}}$  at radius  $R$  around a mass  $M$ , we can write:

$$\frac{V_{\text{rot}}^2}{R} = \beta \frac{GM}{R^2} \implies M = \frac{RV_{\text{rot}}^2}{\beta G} \quad (1.8)$$

where  $\beta$  is of the order of unity and takes into account departure from spherical symmetry. Introducing a constant mass-to-light ratio  $\Upsilon$  and assuming that all galaxies have the same central surface brightness  $I_0$ , so that  $L = 2\pi R^2 I_0$  (exponential disk), we have:

$$L = \left(\frac{L}{M}\right)^2 \frac{M^2}{L} = \frac{1}{2\pi I_0 \beta^2 G^2 \Upsilon^2} V_{\text{rot}}^4 \quad (1.9)$$

which reproduces the scaling of the Tully-Fisher relation. Although this simple argument is far from a proper derivation of the TFR and it is based on the potentially questionable assumptions of constant  $\Upsilon$  and  $I_0$  for all galaxies, it nevertheless jus-

tifies somehow the existence of such scaling relation. However, it is curious to note that, in Equation 1.9,  $\Upsilon$ ,  $I_0$  and  $V_{\text{rot}}$  are quantities related to the disk, whereas in the observed TFR the rotation velocity, in particular  $V_{\text{flat}}$ , is driven by the DM halo.

The Tully-Fisher relation can be used to estimate the distances of local galaxies by simply measuring their rotation velocity and their apparent magnitude, which can be converted to absolute magnitude through the relation. Moreover, the TFR constrains galaxy formation theories both in the standard  $\Lambda$ CDM picture (e.g. Mo, Mao & White, 1998; Bullock et al., 2001) as well as in modified gravity theories (e.g., Mannheim & Kazanas, 1989; Moffat, 2006). Reproducing the relation is a challenging task: early semi-analytic models (e.g., van den Bosch, 2000) and  $N$ -body simulations (e.g., Benson et al., 2003) produced galaxies with rotation velocities at a given luminosity much higher than observed. Simulations with increasing resolution and the introduction of more sophisticated treatments of the baryonic component, like recipes for star formation, supernova feedback, radiative cooling and radiative transfer (e.g., Governato et al., 2007; Portinari & Sommer-Larsen, 2007; Agertz, Teyssier & Moore, 2011), brought significant improvements in reproducing the TFR. Although a few recent studies claimed to reproduce the local observed scaling values of the relation (Schaye et al., 2015; Santos-Santos et al., 2015), accounting for them is still problematic in most simulations (Dutton et al., 2010; Marinacci, Pakmor & Springel, 2014). The TFR is therefore a severe testing ground for galaxy formation theories and it is important to minimize the observational uncertainties on its evolution in order to constrain cosmological simulations.

## 1.5 A short evolutionary picture of disk galaxies

As mentioned, according to the hierarchical scenario of structure formation, galaxies form from the collapse of over-dense regions of matter and grow through an almost uninterrupted accretion of smaller substructures of both baryonic and dark matter. The conventional picture of galaxy formation in the CDM cosmological framework, developed at the turn of 1970s and 1980s, arises from the first models of collapse and gas cooling within dark matter structures (Rees & Ostriker, 1977; Silk, 1977; White & Rees, 1978). According to this standard model, diffuse baryonic gas is trapped into dark-matter potential wells and falls towards the center of the massive haloes. During the collapse, shocks heat the gas to approximately the virial temperature  $T_{\text{vir}} = 10^6 (V_c [\text{km/s}]/167)^2$  K out to a radius  $R_{\text{vir}}$  (Kereš et al., 2005), forming an isotropic and spherical halo in quasi-hydrostatic equilibrium. In the central and denser regions, hot and virialised gas starts to radiate away its thermal energy and quickly cools down from the inside out. While gas cools, it loses the pressure support against gravity, it contracts and condenses to higher densities, until it settles

into a disk-like structure supported by the centrifugal force due to its own angular momentum (Fall & Efstathiou, 1980). This gaseous disk is then converted into a stellar disk by the star formation process. Physical properties of the collapsing gas, such as its angular momentum, density and temperature, deeply affect the morphology and the structural parameters of the end-product galaxies.

In this classical picture, the evolution of galaxies following the initial collapse is mainly driven by merger events and by the so-called “cycle of baryons”. Once accreted from the intergalactic medium (IGM) to the interstellar medium (ISM), baryonic matter cools down and forms stars. These stars return back into the ISM and possibly to the IGM a fraction of their metal-enriched gas through supernovae explosions and stellar winds (stellar feedback). The physical details of the mechanisms of gas accretion and stellar feedback are still not completely understood. Unlike the evolution of dark matter structures, which is only driven by gravitation, a proper treatment of baryonic structures must include complex physical processes, such as gas heating and cooling, star formation and chemical enrichment. These processes have important effects on scales so small that can not be resolved by modern cosmological simulations. The most challenging goal of today simulations is indeed to include recipes for the unresolved baryonic physics in order to reproduce the properties of real galaxies (e.g., Agertz et al., 2013; Stinson et al., 2013; Hopkins et al., 2014).

A comprehensive description of the physical mechanisms driving star formation (Kennicutt & Evans, 2012), stellar feedback (Dale, 2015) and AGN feedback (Fabian, 2012) is well beyond the purposes of this introductory Chapter. In the next section, we just quickly describe the problem of gas accretion in galaxies as a background for [Chapter 4](#).

### 1.5.1 Gas accretion

The collapsed gas constitutes the reservoir from which stars can form. In disk galaxies, the fuel for star formation throughout the Hubble time has to be continuously provided by gas accretion, otherwise spiral galaxies would have exhausted their initial gas reservoirs in a few Gyrs (e.g., Hopkins, McClure-Griffiths & Gaensler, 2008). While gas is accreted and new stars formed, the galaxy progressively grows and increases its disk-scale length. Gas accretion can take the form either of a steady-state and slow accretion or of a stochastic and rapid accretion through mergers.

The IGM constitutes a large reservoir of gas for star formation (e.g., Bregman, 2007). The inhomogeneities in the temperature of the cosmic microwave background (e.g., Pryke et al., 2002) and the matching between primordial nucleosynthesis models and measurements of the chemical abundances in galaxies (e.g., Walker et al., 1991) show that baryons account for about 16% of the total fraction of matter in the

Universe ( $\Omega_m = 0.315$ ,  $\Omega_b = 0.049$ , Planck Collaboration et al., 2014). Observations at various wavelengths show that today only a small fraction (about 10%) of baryons is contained in stars ( $\Omega_* \sim 0.004$ ) and in the interstellar medium ( $\Omega_{\text{HI}} = 0.0004$ ) of galaxies. Most of baryons must therefore still reside in a diffuse warm-hot intergalactic medium (WHIM) at temperatures of  $10^5$ - $10^7$  K.

It is commonly accepted that the accretion from the IGM can occur in two “modes”, called “hot” and “cold” mode accretion. In the hot mode, the infalling gas starts in a diffuse phase, goes through a shock-heated phase and reaches the cold galactic phase by cooling and condensing processes, similarly to the above-mentioned classical disk formation theory (White & Rees, 1978). In this case, the accretion time is set by the cooling time of the gas shocked to the virial temperature. For a Milky-way-like galaxy, with  $T_{\text{vir}} \sim 2 \times 10^6$  K, the cooling time is  $\tau_{\text{cool}} \simeq (3kT)/(n\Lambda(T)) \sim 6$  Gyr, where  $k$  is the Boltzmann constant,  $n \simeq 2 \times 10^{-4} \text{ cm}^{-3}$  is the gas density (e.g., Gatto et al., 2013) and  $\Lambda(T_{\text{vir}}) \simeq 2 \times 10^{-23} \text{ erg cm}^3 \text{ s}^{-2}$  is the cooling function at metallicity  $Z \simeq 0.1 Z_{\odot}$ . In the cold mode accretion, the gas falls onto the galaxy following anisotropic and filamentary streams through the halo without being heated to the virial temperature and remaining relatively cold during the accretion process (Binney, 1977). In this case, the time scales of accretion are of the order of the free-fall time  $\tau_{\text{ff}} \lesssim 1 - 2$  Gyr. The cold mode is usually more efficient than the hot mode, since in many cases  $\tau_{\text{ff}} < \tau_{\text{cool}}$ .

High-resolution cosmological simulations (e.g., Kay et al., 2000; Kereš et al., 2005; Ocvirk, Pichon & Teyssier, 2008) suggest that the dominant accretion mode depends on the total dynamical mass of the structure and that the transition between dominant cold and hot modes occurs at a halo mass of about  $M_{\text{h, thresh}} \sim 2 - 3 \times 10^{11} M_{\odot}$  or at a baryonic mass of the galaxy of about  $M_{\text{b, thresh}} \sim 2 - 3 \times 10^{10} M_{\odot}$ , even though galaxies slightly above the transition masses can also have cold gas filaments that penetrate into the halo and that may continue to directly feed the central galaxy (Figure 1.7). The general explanation is that stable virial shocks can not form in low mass halos because of the short cooling times of the gas (Birnbom & Dekel, 2003). Cold mode accretion should dominate the global growth of galaxies at high redshifts ( $z \sim 2$ ) and the growth of lower mass objects at later times, corresponding to the population of today low-mass star-forming galaxies. The hot mode dominates in massive structures and in general at low redshifts. However, the relative importance of hot and cold modes seems to significantly depend on the implementation of the baryonic physics in different codes (e.g., smoothed particle hydrodynamics, adaptive mesh refinement, etc.) and recent simulations suggest that the cold mode is likely less important than previously thought (Nelson et al., 2015). The Milky Way, with an estimated halo mass of  $M_{\text{h}} \simeq 1.3 \times 10^{12} M_{\odot}$  (Piffi et al., 2014), is expected to be today in the regime where the hot mode dominates.

The second channel of gas accretion is through merger events, which can be

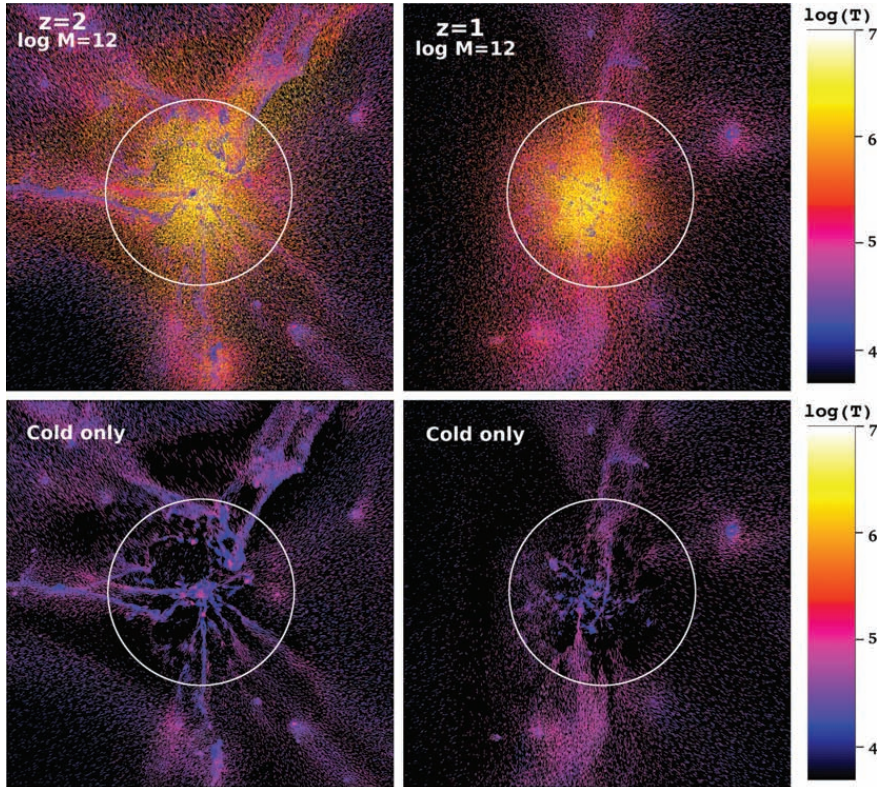


**Figure 1.7:** Temperature snapshots of a cosmological  $\Lambda$ CDM simulation of a Milky-Way like galaxy from Kereš et al. (2009). *Left panels* are snapshots at  $z = 2$  ( $M_{\text{halo}} = 1.1 \times 10^{12} M_{\odot}$ ), *right panels* at  $z = 1$  ( $M_{\text{h}} = 1.2 \times 10^{12} M_{\odot}$ ). The box region is  $1 h^{-1}$  Mpc (comoving) on a side and  $1 h^{-1}$  Mpc (comoving) in projected depth. Upper panels show all the gas particles, lower panels show only the gas with  $T < 10^5$  K but with the same colour scale (indicated on the right-hand side). The white circle shows the virial radius. In this simulation, filamentary structures of the cold mode accretion persist even above the transition mass at  $z = 1$ , but progressively decrease as the halo mass increases.

roughly described by the extended Press-Schechter formalism, where galaxies, during their lifetime, experience a small number of major mergers, more common at high redshifts, and an almost continuous infall of dwarf galaxies and gas clouds (e.g., Lacey & Cole, 1993). In a major merger, where the mass ratio of the larger galaxy (1) to the smaller galaxy (2) is  $M_1/M_2 \lesssim 4$ , the interaction can be quite dramatic. The resulting merged galaxy is largely determined by the violent relaxation of the two merging systems (Toomre & Toomre, 1972; Schweizer, 1982), which settles it in a new virial equilibrium. In this case, the final structure can resemble or not the initial morphology of the merging galaxies. Minor mergers ( $M_1/M_2 > 4$ ) are less violent, the more massive galaxy usually is just perturbed by the less massive one and it retains its initial structure. During a merger, the stellar component can penetrate freely, but the gaseous components collide and large amounts of gas can be driven to the center of the larger galaxy (e.g., Mihos, Richstone & Bothun, 1992),

causing an intense star formation over a short timescale or “starburst” (Schweizer, 1998). The high fraction of starburst galaxies observed in the high- $z$  Universe (e.g., Sub-millimeter galaxies, see Lagache, Puget & Dole, 2005) suggests a rapid growth of early systems due to mergers. In the local Universe, where major interactions are infrequent, only minor mergers could have a substantial contribution to gas accretion.

## 1.6 Brief outline of this thesis

All the fields of study mentioned in the previous Sections, from the mass distribution of dark matter haloes to the scaling relations and galaxy interactions, require a precise determination of the kinematic and dynamical properties, from the innermost to the outermost parts of galaxy disks. Both rotation velocities and velocity dispersions are fundamental parameters to correctly understand the dynamical support of galaxies. The measurement of both these quantities is usually not a trivial task, especially for data lacking adequate spatial/spectral resolution.

In this thesis, we developed a new code, named  $3^{\text{D}}$ BAROLO, to derive the kinematics of disk galaxies from emission-line observations. Although our approach perform as well as the traditional techniques for high spatial resolution observations, it is specifically targeted to work with very low resolution data, where other techniques fail. In [Chapter 2](#), we review the standard fitting techniques to derive the kinematics of disk galaxies and describe in detail the main fitting algorithm and the additional modules available in  $3^{\text{D}}$ BAROLO.

[Chapter 3](#) is devoted to several applications and tests using both HI observations in the nearby Universe and mock galaxies. In particular, we start from high resolution data and gradually move to lower and lower resolutions, down to barely resolved galaxies. We compare the rotation curves and the velocity dispersion profiles obtained with  $3^{\text{D}}$ BAROLO to those derived using more traditional approaches, showing how the latter become unreliable in galaxies with less than 15-20 resolution elements across the disk. In addition, we test the effects of the spectral resolution and noise on the derivation of kinematic models with  $3^{\text{D}}$ BAROLO and discuss the limitations of our code.

In [Chapter 4](#), we present a further scientific application of  $3^{\text{D}}$ BAROLO in the local Universe. Taking advantage of the source finder implemented in the code, we look for dwarf galaxies around massive star-forming galaxies in a large sample of HI observations. Under the assumption that all the detected satellites will be accreted in the shortest possible time, we calculate the maximum contribution of future minor mergers to the total gas accretion and we compare it to the star-formation rates of the main spiral galaxies in the sample.

**Chapter 5** deals with the kinematics of normal star-forming galaxies in the high- $z$  Universe. We use <sup>3D</sup>BAROLO to derive rotation curves and velocity dispersions in a small sample of galaxies at  $z \sim 1$  observed in the H $\alpha$  line with the VLT/KMOS spectrograph. We furthermore discuss the kinematic evolution of disk galaxies and of the Tully-Fisher relation from  $z \sim 1$  to now.

Finally, a summary of the main results and a brief outlook to future applications is presented in **Chapter 6**.

## $3^{\text{D}}$ BAROLO: a new software to derive the kinematics of galaxies<sup>†</sup>

ABSTRACT — In this Chapter, we present  $3^{\text{D}}$ BAROLO, a new code that derives rotation curves of disk galaxies from emission-line observations. This software fits 3D tilted-ring models to spectroscopic data-cubes and can be used with a variety of observations: from HI and molecular lines to optical/IR recombination lines. The fitting method is unaffected by beam smearing and it is very powerful in disentangling rotation velocity from velocity dispersion. We describe in detail the structure and the features of the main fitting algorithm. We also discuss some additional functions, like the source-detection and first-estimate modules, which make it possible to automatically run  $3^{\text{D}}$ BAROLO on large 3D datasets. The software, installation and usage guides are publicly available at  $3^{\text{D}}$ BAROLO’s website: <http://editeodoro.github.io/Bbarolo>.

The derivation of kinematic properties of galaxies is fundamental to understand their dynamical state and evolution. In this context, spectroscopy plays a primary role since it can naturally trace the motion of matter thanks to the Doppler shift of the emission and absorption lines. In this Chapter, we start with a description of the data products of emission-line observations (Section 2.1) and we introduce the tilted-ring model approximation for disk galaxies, illustrating how this model can be fitted to the data and used to derive the galaxy kinematics (Section 2.2). We discuss the main advantages and limitations of the current methods, in particular problems related to instrumental biases (Section 2.3).

The second part of the Chapter (Sections 2.4, 2.5 and 2.6) is devoted to present the new 3D software specifically developed for this thesis and named  $3^{\text{D}}$ BAROLO, which stands for “3D-Based Analysis of Rotating Objects from Line Observations”.

---

<sup>†</sup>Based on E. M. Di Teodoro & F. Fraternali, 2015, MNRAS, 451, 3021

This code works with 3D FITS images (see [Section 2.1](#)) having two spatial dimensions and one spectral dimension. <sup>3D</sup>BAROLO builds a number of models in the form of artificial 3D observations and compares them with the input cube, finding the set of geometrical and kinematic parameters that best describes the data. Our purpose is to provide an easy-to-use software that might be applicable to a wide range of emission-line observations, from radio-HI data of local galaxies to sub-mm and optical/IR lines of galaxies up to high redshift, from high to very low spatial resolution. Unlike the majority of other fitting algorithms, <sup>3D</sup>BAROLO is specifically designed to work on low spatial resolution data, where the kinematic information is largely biased by the size of the beam or Point Spread Function (PSF).

## 2.1 Emission-line observations

The interstellar medium is made of ions, atoms, molecules and dust particles. Our knowledge of the ISM mostly derives from observations of the infrared continuum emitted by the dust and of different atomic and molecular transition lines. Molecular gas can be traced especially with the CO lines, neutral gas can be seen in hyper-fine HI line at 21 cm in the local Universe and in fine-structure lines, like the C<sup>+</sup> line at 158 $\mu$ m, detectable also in galaxies at high redshift. Ionized gas emits several optical/NIR recombination lines, such as the Balmer series of hydrogen (e.g., H $\alpha$ , H $\beta$ , etc.), nitrogen N and oxygen O forbidden lines. In integral field spectroscopy, like radio and mm/submm synthesis observations or Integral Field Unit (IFU) observations, the emission lines can be used to study not only the distribution, but also the kinematics/dynamics of the ISM.

The data products of integral field spectroscopy observations have typically three dimensions, namely two spatial dimensions, which represents the coordinates of the galaxy onto the plane of the sky, and one spectral dimension, expressed as a velocity, a frequency or a wavelength. These 3D observations are usually referred to as “data-cubes” and they contain information about the intensity, the spatial position and the velocity of the line emission. A data-cube therefore can be read as a collection of 1D line profiles, namely one spectrum per each spatial position or, equivalently, as a collection of 2D images, called “channel maps”, that represent the position on the sky of the line-emitting material at a given Doppler shift with respect to the reference ([Figure 2.1](#)). A single 3D volume element  $(x, y, v)$  of a data-cube is often referred to as a “voxel”, whereas a 2D spatial pixel  $(x, y)$  is also called “spaxel”.

Two dimensional maps of the line intensity ( $I$ ), bulk mean velocity ( $\langle v \rangle$ ) and velocity dispersion ( $\sigma_v$ ) can be extracted from 3D data-cubes using different projection approaches. The simplest way is the evaluation of the moments of the 1D

line-profile distributions:

$$I = M_0(x, y) = \int I_\nu(v)(x, y) dv = \sum_v I(v)(x, y) \Delta v$$

$$\langle v \rangle = M_1(x, y) = \frac{\int I_\nu(v)(x, y)v dv}{\int I_\nu(v)(x, y) dv} = \frac{\sum_v I(v)(x, y)v}{\sum_v I(v)(x, y)}$$

$$\sigma_v = M_2(x, y) = \sqrt{\frac{\int I_\nu(v)(x, y)(v - M_1)^2 dv}{\int I_\nu(v)(x, y) dv}} = \sqrt{\frac{\sum_v [I(v)(x, y)(v - M_1)^2]}{\sum_v I(v)(x, y)}}$$

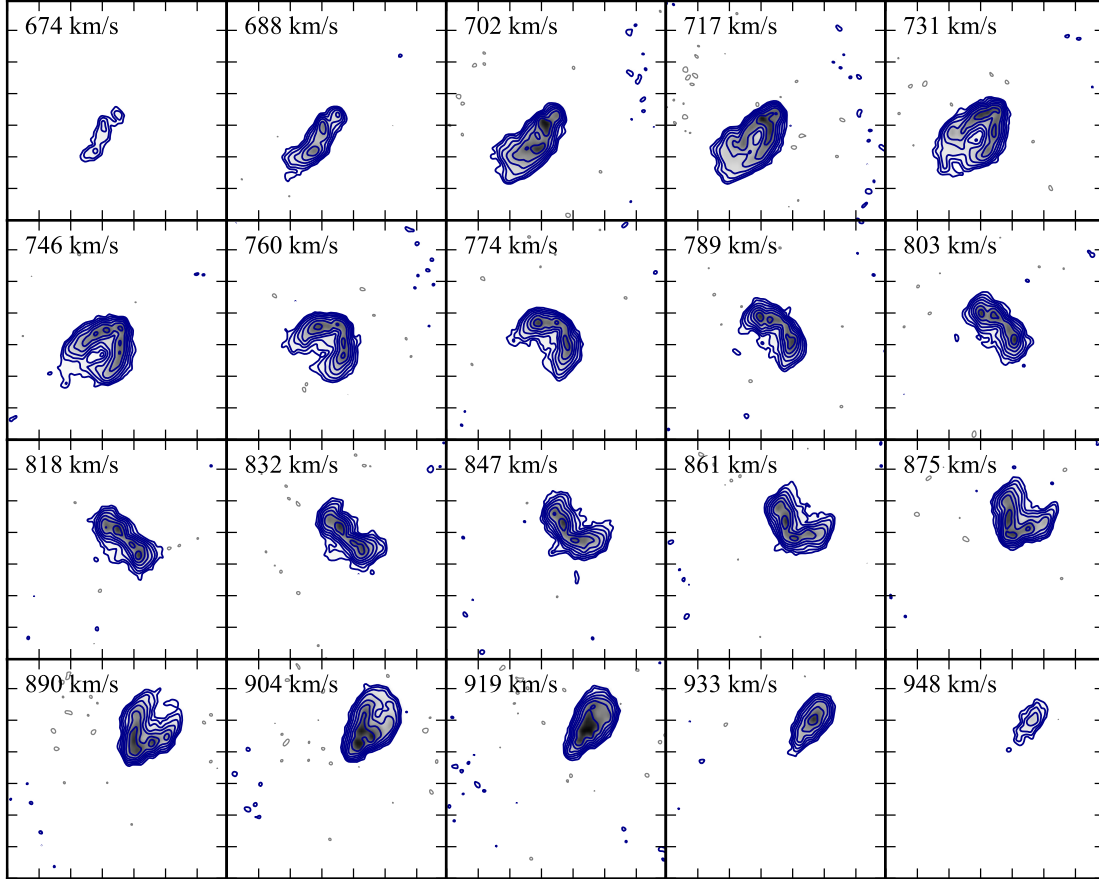


**Figure 2.1:** HI data-cube for the spiral galaxy NGC 4559 visualized as 2D channel maps, each showing the HI emission at a given velocity along the line of sight. The data are from Barbieri et al. (2005) and have been taken with the Westerbork Synthesis Radio Telescope (WSRT). The systemic velocity is  $810 \text{ km s}^{-1}$ . Blue contours are at  $2^n \times 3\sigma_{\text{noise}}$  levels, being  $\sigma_{\text{noise}}$  the spread of the noise distribution and  $n = 0, 1, \dots, 7$ , grey contours are at  $-3\sigma_{\text{noise}}$  level.

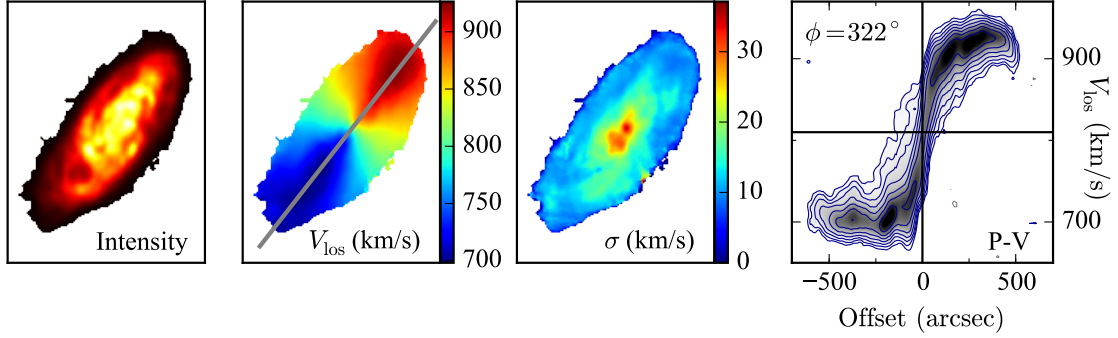


**Figure 2.2:** From *left to right*: HI intensity map, velocity field, velocity dispersion map and position-velocity diagram for the galaxy NGC 4559, derived from the data-cube shown in [Figure 2.1](#). The P-V diagram is extracted along the major kinematic axis (grey thick line on the velocity field) and the contours are as in [Figure 2.1](#). Data are from Barbieri et al. (2005).

where  $M_n$  denotes the  $n$ th moment. The 0th-order term is the total flux intensity  $I$ , the 1st-order term is the characteristic recession velocity  $\langle v \rangle$  and the 2nd-order term is the velocity dispersion  $\sigma_v$ . Higher-order moments, usually parametrized as Gauss-Hermite coefficients  $h_3$  and  $h_4$ , can be further evaluated in order to study asymmetries in the distributions. In the above equations,  $I_\nu(v)(x, y)$  is the flux density at the spatial  $(x, y)$  position and velocity  $v$ . Applied to actual data-cubes, the integrals are converted to summations over the channels. Examples of the so-called “moment maps” are shown in [Figure 2.2](#).

A second technique to derive maps from data-cubes is to fit Gaussian line profiles in the spectral direction (e.g., Begeman, 1987; Swaters, 1999). The mean velocity gives the recession velocity and the standard deviation the dispersion. The integral gives the line intensity. Depending on the complexity of the line profiles, more sophisticated methods have been used, such as multiple Gaussian line profiles (Oh et al., 2008) and/or including a skewness term (e.g.  $h_3$  and  $h_4$  Gauss-Hermite polynomials, van der Marel & Franx, 1993). This latter is particularly useful for kinematic maps derived from stellar absorption lines of ETGs (e.g., Emsellem et al., 2004; Cappellari et al., 2011).

The global profile or global spectrum of a source is the spatially-integrated line emission of the galaxy as a function of the line-of-sight velocity:

$$I_{\text{tot}}(v) = \int I(v)(x, y) dx dy = \sum_x \sum_y I(v)(x, y) \Delta x \Delta y \quad .$$

Spiral galaxies usually have broad global profiles with a typical double-horned shape indicative of flat rotation curves, whereas dwarf galaxies show narrower emission and their profiles tend to resemble Gaussian functions. It is worth noticing that

in the literature, the expression “velocity dispersion” is sometime used to refer both to the dispersion of the single line profiles and the integrated dispersion over larger areas in the galaxy disk. The first one is a measure of the random motions of gas around the mean rotation field at each position, assuming that the spatial/spectral resolution is good enough (see [Section 2.3](#)). The second one includes the contributions from any bulk motions of the gas, such as rotation. In this thesis, we will always refer to the “velocity dispersion” of the gas ( $\sigma_{\text{gas}}$ ) as the intrinsic line broadening of the single profiles corrected for the instrumental broadening  $\sigma_{\text{instr}}$ . Thus, this velocity dispersion is a measure of the gas turbulence (see [Section 1.2.1](#)). In other circumstances we will call it “line broadening”. We will then use the width at the 20% of the peak intensity flux ( $W_{20}$ ) as a measure of the broadening of the global line profile.

Finally, in this thesis we will make a wide use of position-velocity diagrams (P-Vs), which are slices through the spectral dimension taken along some preferential spatial direction. Most used P-Vs are extracted along the major kinematic axis, since they naturally trace the rotation curve projected along the line of sight. An example of such P-V is shown in [Figure 2.2](#) (*rightmost* panel).

## 2.2 The derivation of rotation curves: the tilted-ring model

A rotation curve of a galaxy is the one-dimensional representation of the circular velocity as a function of radius. Stellar and gas rotation curves can be derived using different observations. The rotation of the stellar component can be traced using strong stellar absorption lines, such as the H-K doublet of the singly-ionized Calcium. In late-type galaxies, prominent emission lines of the ISM, like HI, CO and H $\alpha$  lines, are typically used to trace the gas rotation. The derived stellar and gas kinematics agree in most galaxies, but, in some cases, stars and gas show misalignment in the rotation (e.g., counter-rotating disks, polar rings, see [Corsini, 2014](#)), suggesting a merging or a gas accretion scenario (e.g., [Algorry et al., 2014](#)).

The simplest and most used way to describe the kinematics of disk galaxies is through the so-called “tilted ring model”, first employed by [Rogstad, Lockhart & Wright \(1974\)](#) to trace the prominent warp of M83, and then widely used in most kinematic studies of spiral galaxies (e.g., [Binney, 1978](#); [Begeman, 1987](#); [Lovelace, 1998](#)). In a tilted-ring model, the galaxy disk is decomposed in a number of rings with different radii  $R$ , as shown in [Figure 2.3](#). Each ring is considered as an infinitely thin annulus where the matter in a given orbit is confined and moves at a constant circular velocity  $V_{\text{rot}}(R) \simeq V_{\text{c}}(R)$  (see [Section 1.3](#)) around a common center  $(x_0, y_0)$ . This approximation is very good for local disk galaxies without bars as their orbits are nearly circular, with a typical face-on axis ratio  $b/a > 0.9$  (e.g., [Franx & de Zeeuw, 1992](#); [Schoenmakers, Franx, & de Zeeuw, 1997](#)). Orbits projected onto the

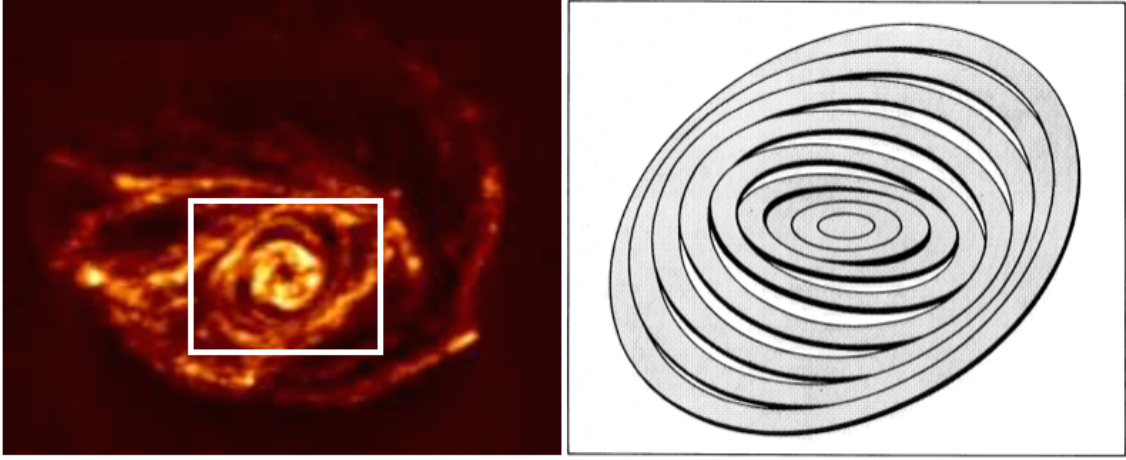


**Figure 2.3:** *Left:* HI total intensity map of the spiral galaxy M83 from Park et al. (2001). *Right:* Tilted-ring description of M83 by Rogstad, Lockhart & Wright (1974). The model refers to the region highlighted with the white rectangle.

plane of the sky are seen as ellipses described by an inclination angle  $i$ , which gives the tilt of the ring, and a position angle  $\phi$ , which gives the orientation of the ring on the sky. The galaxy moves as a whole at a systemic velocity  $V_{\text{sys}}$ , so that, because of the Doppler shift, the approaching half of each ring has line-of-sight velocities smaller than  $V_{\text{sys}}$  and the receding half has velocities larger than  $V_{\text{sys}}$  (Figure 2.2). Each ring is therefore entirely defined by four geometrical parameters and three kinematic parameters that depend only on  $R$ :

- $(x_0(R), y_0(R))$ : the coordinates of the ring center.
- $i(R)$ : the *inclination angle*, defined as the angle between the plane of the galaxy and the line of sight ( $i = 90^\circ$  for edge-on).
- $\phi(R)$ : the *position angle* of the projected ellipse of a ring on the plane of the sky, measured between the north direction and the major axis of the receding half of the galaxy, in anti-clockwise direction.
- $V_{\text{sys}}(R)$ : the *systemic velocity*, defined as the heliocentric velocity of the center of each ring.
- $V_{\text{rot}}(R)$ : the *rotational velocity* at radius  $R$ .
- $V_{\text{exp}}(R)$ : the *expansion velocity* in the radial direction for each ring, used to add non circular motions.

Fitting a tilted-ring model to a galaxy allows us to derive its rotation curves and infer the mass distribution (see Section 1.3). Furthermore, studying the  $i(R)$  and

$\phi(R)$  functions, we can detect and characterize peculiarities of the gas distribution, like outer warps. A tilted ring-model described by the above-mentioned parameters is usually fitted to emission-line observations. In particular, there are two main approaches to perform this task: fitting the model to the 2D velocity fields and fitting the model to the full 3D data-cubes.

### 2.2.1 Tilted-ring model on velocity fields

The standard approach to link the tilted-ring model to observations is through the fit of 2D velocity fields, extracted from 3D data-cubes (see [Section 2.1](#)). The derived velocity map can be written in terms of a generic harmonic expansion (e.g., Franx, van Gorkom, & de Zeeuw, 1994), which represents the decomposition into multiple harmonic terms of sine and cosine of the observed line-of-sight velocities along the tilted rings. With this prescription the line-of-sight velocity is:

$$V_{\text{los}}(R) = A_0(R) + \sum_{n=1}^N \left( A_n(R) \cos(n\theta) + B_n(R) \sin(n\theta) \right) \quad (2.1)$$

where  $N$  is the maximum order used,  $\theta$  is the azimuthal angle in the plane of the disk,  $A_n$  and  $B_n$  are the coefficients of the harmonic term of order  $n$ . Under the assumption of the dominance of circular motions, the velocity field can be fully described by including only  $n = 0$  and  $n = 1$  terms. In this particular case, the zero-th order harmonic components is the systemic velocity  $A_0(R) = V_{\text{sys}}(R)$  and the first order coefficients are the projected circular and streaming radial velocities onto the plane of sky, i.e.  $A_1(R) = V_{\text{rot}}(R) \sin i$  and  $B_1(R) = V_{\text{exp}}(R) \sin i$ , with  $i$  inclination angle of the disk. Under these assumptions, from [Equation 2.1](#), the velocity along the line of sight at a given coordinate  $(x, y)$  on the velocity field can be written as:

$$V_{\text{los}}(x, y) = V_{\text{sys}} + V_{\text{rot}}(R) \cos \theta \sin i + V_{\text{exp}}(R) \sin \theta \sin i \quad (2.2)$$

where the angle  $\theta$  is defined from the major axis, i.e.  $\theta = 0^\circ$  for major axis, and related to the four geometrical parameters  $i$ ,  $\phi$ ,  $x_0$  and  $y_0$  through:

$$\begin{aligned} \cos \theta &= \frac{-(x - x_0) \sin \phi + (y - y_0) \cos \phi}{R} \\ \sin \theta &= \frac{-(x - x_0) \cos \phi - (y - y_0) \sin \phi}{R \cos i} \end{aligned}$$

where  $R = \sqrt{(x - x_0)^2 + (y - y_0)^2} / (\cos i)^2$  denotes the face-on radius of the galaxy projected on the plane of the sky.

It is straightforward to fit Equation 2.2 to a velocity field by using any of the numerous non-linear least-squares fitting techniques (e.g., Press et al., 2007, Chap. 15), finding for each ring of radius  $R$ , the combination of  $V_{\text{sys}}$ ,  $V_{\text{rot}}$ ,  $V_{\text{exp}}$ ,  $x_0$ ,  $y_0$ ,  $i$  and  $\phi$  that best describes the observed velocity field. There are several available algorithms that perform this fit to velocity fields. The most used is ROTCUR (van Albada et al., 1985; Begeman, 1987), which can be found in data analysis packages like AIPS (Fomalont, 1981), GIPSY (van der Hulst et al., 1992) and NEMO (Teuben, 1995). ROTCUR simply fits the function of Equation 2.2 by using a Levenberg-Marquardt solver (Levenberg, 1944; Marquardt, 1963). In the last decades, several new codes have refined this basic 2D approach by experimenting with different fitting techniques and by extending the harmonic expansion to higher-order terms to take into account asymmetries and non-circular motions. These 2D fitting algorithms include RESWRI (Schoenmakers, 1999), RINGFIT (Simon et al., 2003) and DISKFIT (Spekkens & Sellwood, 2007; Sellwood & Sánchez, 2010).

All the above 2D algorithms are fast from a computational point of view and do return excellent kinematic models and reliable rotation curves when applied to high-resolution velocity fields. Some drawbacks however exist. The most severe problem in deriving the kinematics from the velocity field is the spatial resolution and the beam smearing, that we will discuss in more detail in Section 2.3. The second issue is related to the derivation of the velocity field. Velocity fields are not the original data set, but they are themselves derived from a data-cube. This requires the intermediate step of extracting a characteristic velocity from the line profile at each spatial pixel, which is not necessarily a trivial task. First, the derivation of an unambiguous velocity is difficult or even not possible whenever the line profiles are not symmetric (de Blok et al., 2008). Moreover, a unique characteristic velocity is meaningless when the line of sight with respect to the observer intersects the disk twice or more, like in nearly edge-on systems or in the presence of thick disks, outer flares and line-of-sight warps. Second, the line profiles can be severely distorted and broadened by instrumental effects, primarily by the spatial resolution (Section 2.3), but also by the instrumental spectral function or instrumental dispersion  $\sigma_{\text{instr}}$ . A velocity profile can therefore have a complex structure, depending both on the intrinsic properties of the galaxy and on the properties of the instrument, and velocity fields derived with different methods (see Section 2.1) can significantly deviate from each other and be inadequate to describe the actual rotation pattern of the galaxy.

One additional limitation of the 2D fitting techniques is the number of independent data points along a given ring on the velocity fields, which usually is too small to satisfactorily constrain all the free parameters together. A number of assumptions are typically made, especially about the geometry of the galaxy, which can be for instance estimated from the available photometric information before the tilted-ring fit. Most used assumptions include a common rotation center and systemic velocity

for all rings, a coplanar disk in the inner regions, namely a fixed inclination angle, and the absence of non-circular motions ( $V_{\text{exp}} = 0$ ). The common fitting strategy implies a number of runs to evaluate the galaxy geometry and subsequent runs, fixing more and more parameters, to derive a reliable rotation curve (Verheijen, 1997; Gentile et al., 2003; de Blok et al., 2008).

### 2.2.2 Tilted-ring model on data-cubes

An alternative approach to find rotation curves is the modeling of the full data-cubes, which consists in artificially reproducing a 3D spectral observation of the emitting material in a galaxy and to compare it with the true observation. This 3D approach is not affected by the systematic effects and above-mentioned issues of 2D fitting methods and gives larger opportunities for describing galaxies. Edge-on galaxies and kinematic features, like line-of-sight warps and thick disks, can in principle be accurately described and incorporated in the fit. Moreover a 3D method can be used at very low spatial resolution and it is almost unaffected by the beam smearing, since the instrumental effects are introduced in the model through a convolution step (see Section 2.4.2). The main drawback is the computational slowness. Unlike the 2D tilted-ring modeling, an analytic form for the fitting function in 3D does not exist and the model is instead constructed by a Monte-Carlo extraction (see Section 2.4.1). Thus, the fit must be performed with algorithms that do not require the knowledge of any partial derivative (e.g., Press et al., 2007, Chap. 10). Such techniques are known to be computationally expensive and they may converge to a local minimum of the function. In addition, the minimization is not just performed on a single map, but on the whole data-cube, which consists of  $n$  maps, where  $n$  is the number of channels. On the other hand, the increasing number of independent data point is a benefit because it helps to constrain the model parameters and to reduce the systematic errors. Finally, a larger number of parameters than in 2D is needed to describe the model, including also the surface brightness distribution, the disk scale-height and the gas velocity dispersion (see Section 2.4.1).

Even if a 3D technique is applicable by means of a simple least-square fit, the direct 3D modeling has been scarcely used in the past mostly because of the missing computational power, which is no more a limitation with today's computers. The visual comparison between the data-cube and an artificial model-cube has been used as an additional step to improve the results of the 2D tilted-ring model and correct for beam smearing, especially in the investigation of the shape of dark matter profiles in the inner regions of galaxies (e.g., Swaters, 1999; Gentile et al., 2004) or in the analysis of complex disk structures (e.g., Fraternali et al., 2001). A pioneering attempt to directly use a 3D approach was made by Corbelli & Schneider (1997) in a study on the outer warp of M33.

A currently available algorithm that can directly fit a 3D tilted-ring model to data-cubes is the Tilted Ring Fitting Code (TiRiFiC, Józsa et al., 2007). TiRiFiC has been mainly developed to work with HI data and to study local galaxies with a detailed description of peculiarities, such as warps, spiral arms and lopsidedness. TiRiFiC has reached a considerable degree of sophistication and it has been successfully used to study the kinematics of nearby galaxies with peculiar features, in particular strong warps and extra-planar gas (Józsa et al., 2009; Zschaechner et al., 2012; Gentile et al., 2013). A recent upgrade of TiRiFiC, named Fully Automated TiRiFiC (FAT, Kamphuis et al., 2015), provides a module to estimate the initial fitting parameters that should allow the user to automatically model large samples of galaxies.

A 3D approach is also used in the Galaxy Parameters and Kinematics code (GalPak<sup>3D</sup>, Bouché et al., 2015), a recent tool targeted to high-redshift galaxies. GalPak<sup>3D</sup> assumes some functional forms for the galaxy parameters, in particular a Sérsic profile for the radial flux intensity and a constant velocity dispersion. The rotation curve is modeled as an arc-tangent  $V_{\text{rot}} = V_{\text{max}} \arctan(R/R_t)$  (Puech et al., 2008), an inverted exponential  $V_{\text{rot}} = V_{\text{max}}[1 - \exp(-R/R_t)]$  (Feng & Gallo, 2011) or a hyperbolic tangent  $V_{\text{rot}} = V_{\text{max}} \tanh(R/R_t)$  (Andersen & Bershadsky, 2013), where  $V_{\text{max}}$  is the maximum rotation velocity and  $R_t$  is the turnover radius between the rising and the flat part of the rotation curve. Best fit parameters are found through a Markov-Chain Monte-Carlo (MCMC) sampler, which is very computational expensive and suitable to be used only on small data-cubes. GalPak<sup>3D</sup> has been successfully used to derive the kinematics of a handful of high- $z$  galaxies (Bacon et al., 2015; Bolatto et al., 2015).

## 2.3 The beam smearing effect

The beam smearing is the main limitation to the derivation of the kinematics of disk galaxies at low spatial resolution, in particular for tracing the inner shape of the rotation curves. This effect has been extensively investigated in HI observations (e.g., Bosma, 1978; Begeman, 1987). In general, the determination of changes in velocity in the inner parts of a rotation curve is difficult when the Point Spread Function (PSF), or beam (radio data), of the telescope is larger than the scale over which the change takes place. This is why the central regions of galaxies should be studied with very high resolution HI observations, or, in many cases, through CO and optical observations, which typically guarantee a higher spatial resolution than current HI data.

In practice, the finite size of the beam of a telescope causes the line emission to be smeared on the adjacent regions. As a consequence, the observed line profile

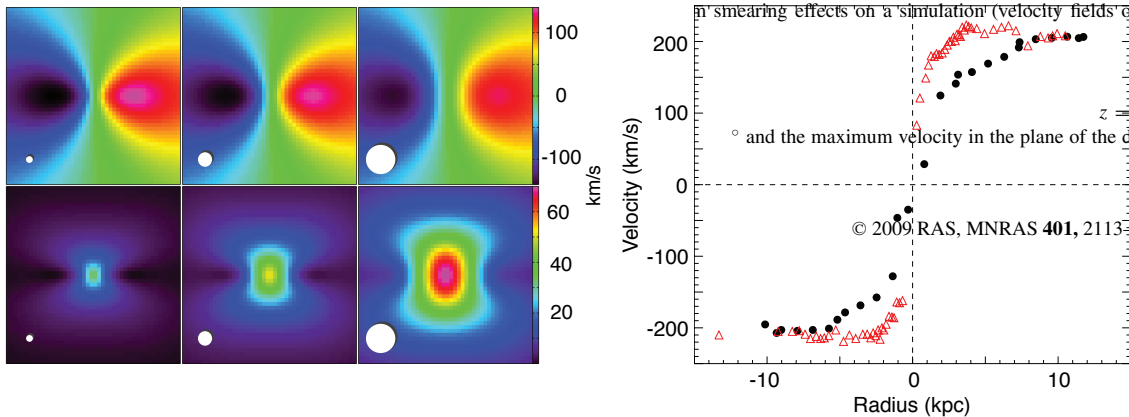


**Figure 2.4:** *Left:* beam smearing effects on a simulated velocity field (*top line*) and velocity dispersion map (*bottom line*) depending on an increasing beam size, represented by the white full circle. The size of the fields is  $5'' \times 5''$ , the pixel size is fixed at  $0.125''$ . From left to right, the beam FWHM increases from  $0.25''$  to  $1''$ . Increasing the beam size causes the velocity gradient along the major kinematic axis to flatten and the velocity dispersions to significantly increase. *Right:* example of a rotation curve obtained for the same galaxy as observed in the local Universe (red open triangles) and at  $z \sim 1$  (black dots), i.e. with a spatial resolution degraded by a factor about 4. The rotation curve derived from the velocity fields rises more slowly as the spatial resolution decreases. Images are adapted from Epinat et al. (2010).

at a certain spatial position, which is given by the convolution of the true intensity distribution and the instrumental PSF, receives contributions from adjacent areas and become broader and potentially asymmetric. Thus the extracted characteristic velocity along a single pixel is not representative of that region, but it rather represents an intermediate velocity in an area of the size of the PSF. Moreover regions with higher flux intensity, typically the internal regions of galaxies, end up to be over-represented in both flux and velocity. The beam smearing may have a large effect on the kinematic maps, since the gradients in the extracted velocity fields tend to become flatter and the values of the velocity dispersion maps larger.

In [Figure 2.4](#) (*left panel*), we show the effect of beam smearing on velocity (*top panels*) and velocity dispersion (*bottom panels*) maps. With the increase of the PSF by a factor 4 (*left to right*), the velocity fields tend to show a more solid-body-like rotation pattern, while the derived velocity dispersions increase by a factor 2-3 on large portions of the field. In other words, part of the rotation velocity is turned into line broadening that can be erroneously interpreted as gas velocity dispersion, producing a degeneracy between these two quantities (see [Section 3.3](#)). The typical effect of the beam smearing is that the derived rotation curves will rise more slowly in the inner regions ([Figure 2.4](#), *right panel*) with potentially dramatic consequences for the dynamical interpretation (e.g., Lelli, Fraternali & Sancisi, 2010). For example, a galaxy with an actual steeply-rising rotation curve can be interpreted as a

dark-matter dominated galaxy in light of the derived slowly-rising rotation curve (Section 1.3), or the measured velocity dispersion can be interpreted as an actual pressure support due to highly turbulent motions of the gas. The beam smearing effect becomes more and more pronounced as the inclination angle of the galaxy increases.

## 2.4 <sup>3D</sup>BAROLO: the fitting algorithm

Here we present a new algorithm to fit tilted-ring models to data-cubes via a residual minimization. <sup>3D</sup>BAROLO can work with any emission-line observation at very different spatial resolutions, however it is specifically targeted to derive a reliable kinematics from very low resolution data, in a situation where 2D techniques can not be used. For this reason, we kept the disk model as simple as possible and we restrain the number of parameters to the bare minimum.

<sup>3D</sup>BAROLO simulates data-cube observations, starting from the model of a rotating gaseous disk, and compares them with real data. The disk is made up by a number of concentric rings with non-zero thickness. The emission from the gas in each ring is generated in a 6D domain (three dimensions for the spatial location and three for the components of the velocity in cylindrical coordinates) and these rings are then projected into a 3D “observational” space (i.e. two spatial and one spectral dimensions). The comparison with the data is performed ring by ring. At each step, if the model is good enough (see below), the algorithm moves to the following ring, otherwise it updates the disk parameters until the best match between model and observations is reached.

The minimization between model and data is performed with the multidimensional downhill simplex solver, also known as the Nelder-Mead method (Nelder & Mead, 1965) for the minimization of non-analytic functions. The user supplies a number of initial guesses for each ring from which the function to be passed to the minimization algorithm is built. Input parameters can be defined either globally or ring-by-ring. If no guess is given, the algorithm will autonomously estimate the initial parameters for the fit (see Section 2.5). The function to minimize is an indicator of how the model and the data differ from each other and its construction occurs through four main steps:

1. *Disk model.* The disk model is built by a Monte-Carlo reproduction of the gas distribution both in the space and the velocity domain. This function derives from the GALMOD routine (Sicking, 1997) implemented in GIPSY.
2. *Convolution.* The model is degraded to the same spatial resolution of the data via a convolution with a 2D Gaussian representing the observational Point

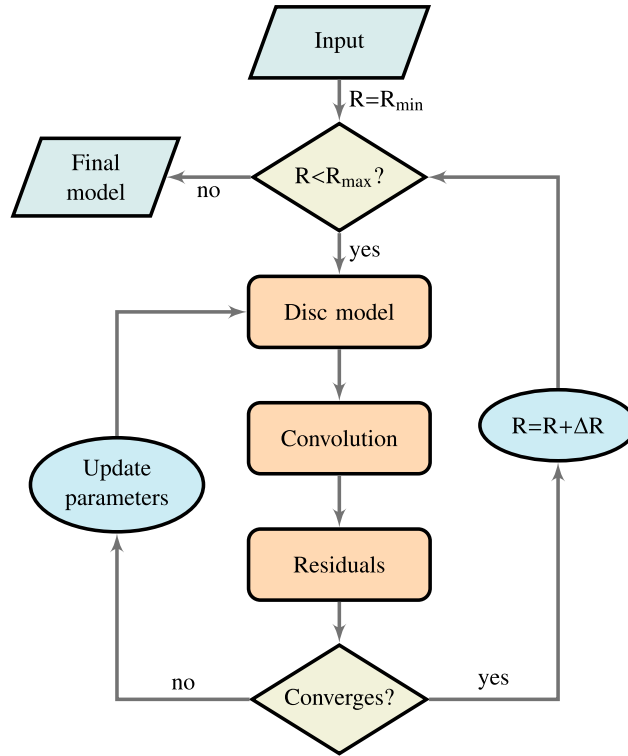


**Figure 2.5:** Flowchart of the <sup>3D</sup>BAROLO main algorithm. For each ring  $R$ , the code builds a 3D model, convolves it with the observational beam/PSF and compares it with the data. If no convergence has been achieved, <sup>3D</sup>BAROLO updates the parameters and starts over. When the algorithm converges to the minimum, it moves to the next ring. The optional normalization step takes place after the convolution step.

Spread Function (PSF). The spectral broadening is instead taken into account in the model construction (see [Section 2.4.1](#))

3. *Normalization.* The model is normalized to the 0th moment map of the observations pixel-by-pixel or azimuthally. This step can be skipped and the density profile supplied by the user or fitted.
4. *Residuals.* Comparison between the model and the data pixel-by-pixel. The sum of the residuals is returned to the minimizing algorithm.

A schematic flowchart of the main fitting algorithm is shown in [Figure 2.5](#). In the following sections, we describe the most important steps and the main features of the code.

### 2.4.1 Disk model

The artificial gaseous disk is constructed with a 3D tilted-ring model by using a stochastic function that randomly populates the space with emitting gas clouds, from which line profiles are built. Each ring of radius  $R$  and width  $\Delta R$ , is described by the following geometrical and kinematic parameters:

- Spatial coordinates of the center  $(x_0, y_0)$ .
- Systemic velocity  $V_{\text{sys}}$ .
- Inclination angle  $i$  with respect to the observer ( $90^\circ$  for edge-on).
- Position angle  $\phi$  of the major axis on the receding half of the galaxy, taken anticlockwise from the North direction on the sky.
- Rotational velocity  $V_{\text{rot}}$ .
- Velocity dispersion  $\sigma_{\text{gas}}$ .
- Face-on gas column density  $\Sigma$ .
- Scale-height of the gas layer  $z_0$ .

All these quantities are allowed to vary from ring to ring. The first six parameters are the same required by 2D fitting algorithms like ROTCUR. The geometry of the tilted-ring model is shown in [Figure 2.6](#). Each ring is filled with gas clouds whose spatial position is given in cylindrical coordinates by a radius  $R_c$  (with  $R - \Delta R/2 < R_c < R + \Delta R/2$ ), an azimuthal angle  $\theta_c$  ( $0 \leq \theta_c \leq 2\pi$ ) and a height  $z_c$  above the plane of the disk. Radius and azimuth are randomly and uniformly chosen, the height is selected as a random deviate from a given vertical distribution of the gas density (available functions are Gaussian,  $\text{sech}^2$ , exponential, Lorentzian and box layer). The position of the clouds is then rotated and projected onto the plane of the sky with a given orientation with respect to the observer, according to the position angle and inclination at that radius.

Once the positions of the clouds are determined, the observed velocities along the line of sight are calculated as a combination of systemic, rotational and random motions. The velocity profile at each location is built around the average velocity by dividing the clouds into a number of sub-clouds with velocities distributed as a Gaussian with dispersion  $\sigma^2 = \sigma_{\text{gas}}^2 + \sigma_{\text{instr}}^2$ , being  $\sigma_{\text{gas}}$ <sup>1</sup> the intrinsic gas dispersion and  $\sigma_{\text{instr}}$  the instrumental broadening. These velocities are then discretized and the contribution of the sub-clouds is recorded in a model cube with the same sizes of the data-cube. <sup>3D</sup>BAROLO uses by default  $\sigma_{\text{instr}} = W_{\text{ch}}/\sqrt{2 \ln 2}$ , where  $W_{\text{ch}}$  is the

<sup>1</sup>We assume that  $\sigma_{\text{gas}}$  is isotropic, being the gaseous disk a collisional system.

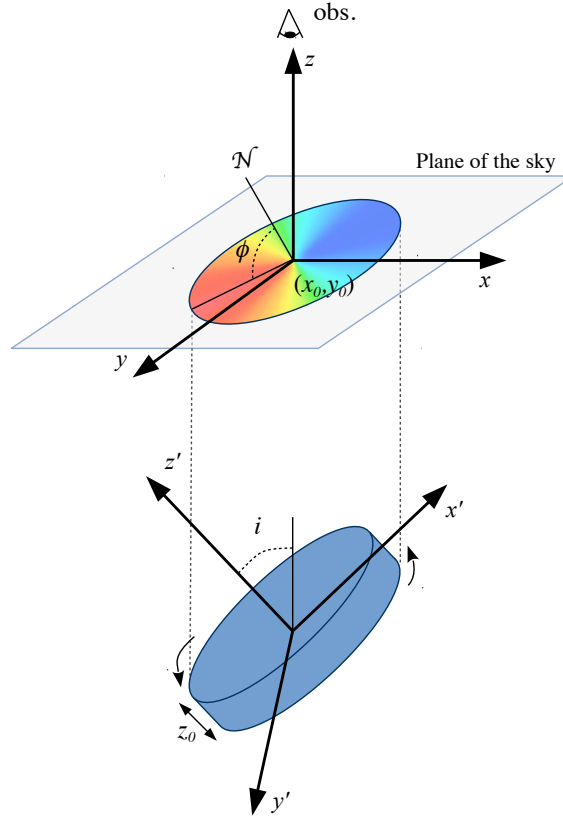


**Figure 2.6:** Geometrical parameters of the disk model. The galaxy disk in the  $x'y'z'$  space is projected into an ellipse in the  $xy$  plane of the sky. The inclination angle  $i$  is taken with respect to the line of sight, the position angle  $\phi$  identifies the position of the major axis on the receding half of the galaxy and it is taken counterclockwise from the North direction.

channel width of the data-cube. This is usually a good assumption in HI data-cubes where Hanning smoothing has been applied (Verheijen, 1997). Otherwise, the user can supply an own value for the spectral resolution.

### 2.4.2 Convolution

The model has a nominal spatial resolution of one single pixel and it needs to be smoothed to the same spatial resolution of the data. This requires to perform a spatial convolution by the observational PSF, or beam, for each spectral channel. We approximate the PSF as a two-dimensional Gaussian function, which is an adequate choice for most radio, millimeter/submillimeter and optical/IR observations. The Gaussian function is defined by three parameters that characterize the elliptical cross-sectional shape of the kernel: the full-width half-maximum (FWHM) of both the major and minor axes ( $a$  and  $b$ , respectively), and the position angle of the major axis ( $\psi$ ), measured anticlockwise from the vertical direction. The kernel of

the two-dimensional Gaussian is defined by the function:

$$k(x, y) = \frac{1}{2\pi\lambda_\kappa\lambda_\eta} \exp \left[ -0.5 \left( \frac{\kappa^2(x, y)}{\lambda_\kappa^2} + \frac{\eta^2(x, y)}{\lambda_\eta^2} \right) \right] \quad (2.3)$$

where  $(x, y)$  are the offsets from the center of the Gaussian and  $\lambda_\kappa$  and  $\lambda_\eta$  are the standard deviations along  $(\kappa, \eta) = (x \sin \psi - y \cos \psi, x \cos \psi - y \sin \psi)$ , the position-angle-rotated frame of reference. The FWHMs ( $a = \sqrt{8 \ln 2} \lambda_\kappa$  and  $b = \sqrt{8 \ln 2} \lambda_\eta$ ) and the position angle are usually read from the FITS header as the BMAJ, BMIN and BPA keywords, respectively, but they can also be manually supplied. In addition, for IFU data, <sup>3D</sup>BAROLO can receive as input an image (or data-cube) of a star, usually observed at the same time of the scientific target. The star is then used to determine the PSF by fitting it with a 2D Gaussian.

This smoothing step is the bottleneck of the fitting algorithm, since the convolution is a computationally expensive operation and <sup>3D</sup>BAROLO needs to perform it for each calculated model. To speed-up this step with Fast-Fourier transforms, we used the shared-memory parallel OPENMP implementation of the FFTW3 library. The user is however advised to use data-cubes with suitable sampling in order to save computational time.

### 2.4.3 Normalization of the surface density

The normalization allows the code to exclude one parameter from the fit, namely the surface density  $\Sigma$  of the gas. We have currently implemented two different kinds of normalization: 1) pixel-by-pixel and 2) azimuthally averaged. In the first case, the model is normalized in such a way that the column density maps of model and observations are the same. In other words, we impose that the integral of each spatial pixel along the spectral dimension in the model is equal to the integral of the correspondent spatial pixel in the observations. This type of normalization allows to have a non-axisymmetric model in density and avoids that untypical regions, like areas with strong and clumpy emission or holes, might affect the global fit (see e.g., Lelli et al., 2012). In the second case, the model is instead normalized to the azimuthal-averaged flux in each ring. According to our tests, the pixel-by-pixel normalization is often a more advisable solution, so this is the default in <sup>3D</sup>BAROLO. The azimuthal-averaged normalization is useful to determine the inclination angle of the outer rings. The normalization step can also be turned off, in this case the user can supply a surface density profile or leave it free to be fitted together with the other parameters.

#### 2.4.4 Residuals

The residuals are calculated by comparing the model and the data pixel-by-pixel. The number  $F$ , which is returned to the minimization algorithm and defines whether a model is suitable or not (i.e. whether convergency is reached, see [Figure 2.5](#)) is the averaged sum of the residuals over each pixel:

$$F = \frac{1}{n} \sum_{i=1}^n \Delta r_i w(\theta_i) \quad (2.4)$$

where  $n$  is number of pixels for which the residuals  $\Delta r_i$  are evaluated and  $w(\theta_s)$  is a weighting function. To be considered, a pixel must either have a non-zero flux in the model or be part of the identified emission region of the galaxy. <sup>3D</sup>BAROLO provides three kinds of residuals:

$$\Delta r = \frac{(M - D)^2}{\sqrt{D}} \quad (2.5a)$$

$$\Delta r = |M - D| \quad (2.5b)$$

$$\Delta r = \frac{|M - D|}{(M + D)} \quad (2.5c)$$

where  $M$  and  $D$  are the flux values of the model and the data, respectively. The (2.5a) residual is a kind of  $\chi^2$  without however a conventional statistical meaning. When  $D$  is a blank pixel, in (2.5a) we set  $D$  equal to the root mean square value (rms) of the cube. The (2.5c) residuals give more weight to regions where the emission is faint and diffuse, the (2.5b) residual is intermediate. The weighting function in [Equation 2.4](#) is  $w(\theta) = |\cos \theta|^m$ , where  $\theta$  is the azimuthal angle ( $0^\circ$  for the major axis) and  $m = 0, 1, 2$ . With  $m \neq 0$ , the residual gives prominence to regions close to the major axis, i.e. where most of the information on the rotation motions lies. As an option, [Equation 2.4](#) can be multiplied by a factor  $(1 + n_b)^p$ , where  $n_b$  is the number of pixels where the model is present but not the observations, in order to penalise models that extend farther than the data. This option is useful, for instance, to estimate the inclination of the outer rings. As mentioned, this choice should be combined with an azimuthal normalization of the surface density.

## 2.5 <sup>3D</sup>BAROLO: additional features

Here, we list and briefly describe some other useful tools available inside <sup>3D</sup>BAROLO. In particular, the source finder and the algorithm for automatically estimating the initial parameters allows <sup>3D</sup>BAROLO to be blindly run on large 3D data sets.

### 2.5.1 Source finder

An utility for the identification of emitting sources is implemented inside <sup>3D</sup>BAROLO. Such a source finder allows <sup>3D</sup>BAROLO to identify all the galaxies within a given data-cube and automatically fit each of them. The searching algorithm is derived from *Duchamp* (Whiting, 2012), a code dedicated to three-dimensional source detection in HI data. The basic idea behind this algorithm is to locate and connect groups of bright and contiguous pixels that lie above some flux threshold, without imposing any size or shape requirement to the detection. The search is performed using either a two-dimensional raster-scanning algorithm (Lutz, 1980) or a one-dimensional research along each individual spaxel spectrum. Three-dimensional sources (two spatial dimensions and one spectral) are then built up on the basis of adjacency or neighborhood criteria both in the velocity and in the spatial domain.

The source detection goes through five main steps, hereinafter briefly described.

1) *Statistics and threshold evaluation.* The first step of the searching algorithm is the determination of the flux threshold above which a pixel can be considered as part of a source. In order to do this, <sup>3D</sup>BAROLO needs to estimate the central value  $M$  and width (spread)  $S$  of the noise distribution in the data-cube. The former should be zero or very close to zero for emission-line data-cubes without systematics (due for instance to problems with the data reduction), where the continuum has been subtracted. <sup>3D</sup>BAROLO calculates the full statistics of the data-cube, namely the mean  $\mu$ , the median  $m$ , the standard deviation  $\sigma_{\text{noise}}$  and the median absolute deviation from the median MADFM. The mean and the standard deviation are normal statistics, whereas median and MADFM are robust estimators and they are less sensitive to the presence of pixels much brighter than the noise. In most cases, the usage of robust statistics, namely the median as noise middle and the MADFM as a proxy for noise spread, is recommended with respect to normal statistics. For a Gaussian distribution, the standard deviation can be written in term of the MADFM as  $\sigma_{\text{noise}} = \text{MADFM}/0.6745$  (for details, see Whiting 2012 and references therein). The threshold  $\tau$  is determined with a simple sigma-clipping, i.e., it is set to a number  $n$  of noise spread  $S$  above the central value  $M$ :

$$\tau = M + nS \quad (2.6)$$

where  $M = \mu$  and  $S = \sigma_{\text{noise}}$  in case of normal statistics,  $M = m$  and  $S = \text{MADFM}/0.6745$  for robust statistics. The value  $\tau$  is the minimum flux that a pixel must possess to be selected by the algorithm. Alternatively to the sigma-clipping, there is also the possibility of manually inserting the value of the threshold.

2) *Pixel detection.* The data-cube is scanned using one of the above-mentioned techniques and a list of all pixels with a flux greater than the threshold is produced. The one-dimensional search examines the data-cube along each single spectrum, looking for and then storing connected sets of channels that meet the threshold requirement for each spaxel. The two dimensional search (Lutz, 1980) analyses the data-cube one channel map at a time: each image is raster-scanned and searched row by row; then, objects detected in each row are compared to objects in subsequent rows, and combined if they are connected in a eightfold sense. This means that, if we have two detected pixels  $A$  and  $B$ , they are considered connected only if  $B$  lies within a 3x3 square around  $A$ , or, to be more precise, if  $B$  is one of  $A$ 's eight horizontal, vertical or diagonal neighbors. The 1D technique is less computationally expensive, but it can bring to spurious detections. On the contrary, the 2D Lutz algorithm is generally more reliable at the price of some computational slowness.

3) *Merging objects.* The searching algorithms described create lists of 1D or 2D objects, neglecting the third dimension. The detected pixels that are considered close to each other based on spatial and spectral requirements are merged together to create 3D objects. The algorithm merges detections which lie within a specified range of pixels or channels. For instance, the user can decide to merge together all those detections that are separated by less than  $n$  pixels in the spatial domain and  $m$  pixels in the spectral domain. The spatial requirement can be replaced with a stricter but more realistic criterion, i.e. only pixels that are adjacent can be merged together. The merging process is repeated twice: in the first stage, each new detection is compared with the sources already detected and it is merged with the first one judged to be the closest. When the searching is completed, the second stage of merging begins: the list of detections is iterated through, looking at each pair of objects and merging them appropriately. Finally, the merged objects are included in the examination to see if a merged pair is suitably close to a third one. After this step, a list of three-dimensional sources is produced.

4) *Growing objects.* All pixels in the detections have a flux higher than the threshold at this stage, which means that objects have a sharp transition with respect to the background. To avoid this, the size of the detections can be increased by adding pixels at the edges of the objects that are above some secondary threshold (again either through a sigma-clipping lower than the primary one or manually inserted) and within a secondary neighborhood criterion in spatial and spectral domains. If the detections are grown, they are sent through the merging algorithm a second time, to pick up any detections that should be merged at the new lower threshold. This step guarantees a smooth transition between the source and the background, allows us to detect the fainter edges of galaxy disks and avoids that sources stay detached in substructures.

5) *Rejecting objects.* The last step is to reject those detections that can not be considered reliable. The user can decide to require for instance a minimum or a maximum number of voxels, spaxels or channels in each detected object. A rejection criterion based on the angular size of the sources is also available. Objects that do not meet the requested criteria are erased from the detection list. Usually, the minimum spatial criterion must have at least the size of the spatial beam of the observations, whereas the minimum number of channels should be chosen to be larger than the typical velocity dispersion of the observed line or the spectral resolution.

### 2.5.2 Estimates of the initial parameters

<sup>3D</sup>BAROLO can automatically estimate the initial parameters of the fit. These initial estimates allow <sup>3D</sup>BAROLO to be run automatically, but the user can also decide to set some parameters and let the code estimate the others. A number of output plots, like channel maps and position-velocity diagrams along the major and minor axes, are provided to allow the user to check the quality of the automatic fits.

The algorithm starts by isolating the galaxy through the source finder described in the previous section. For each detected object, the geometrical and kinematic parameters are guessed in the following order and ways:

- $(x_0, y_0)$ : the coordinates of the center are taken as the flux-weighted average positions (centroids) of the source. This method fails in some situations, for instance when the line emission is not peaked in correspondence to the galaxy center (e.g., star-formation clumps in H $\alpha$  observations at high-redshift), when the galaxy is gas deficient in the internal regions or heavily lopsided. Adopting optical centers/IR, tracing the stellar component, can be a more reliable choice in these cases.
- $V_{\text{sys}}$ : the characteristic velocity of the system is estimated from the global emission-line profile, by taking the midpoint velocity between the two velocities corresponding to the 20% of peak levels on each side of the spectrum. A typical uncertainty for the systemic velocity is of the order of the channel width.
- $\phi$ : the position angle is estimated from the velocity field as the straight line that maximizes the gradient in velocity along the line of sight. For each detected source, the algorithm extract a velocity field as the 1st moment (see [Section 2.1](#)). Then splits the velocity field in  $N$  squared sub-maps, with  $N$  depending on the size of the map, and calculates the median of the velocities for each square. Once the sub-maps where the median velocities are the highest and the lowest have been identified, they are fitted with a linear regression and the first guess for the position angle is found. The value of  $\phi$  is then fine tuned so that the minor axis, defined as the straight line through the center  $(x_0, y_0)$

and perpendicular to the major axis, passes through the largest number of velocity squares near  $V_{\text{sys}}$ . For regular galaxies, the error in the first estimate of the position angle is usually within a few degrees.

- $i$ : the inclination is calculated by fitting a beam-convoluted disk model to the total column density map, extracted as a 0th moment map. The gas density profile is extracted from the observed map along elliptical rings defined by  $(x_0, y_0)$ ,  $\phi$  and  $i$ . A model map is then built from the density profile, smoothed to the same spatial resolution of the data and the inclination  $i$  is fitted to reproduce the observed map. Our tests on mock galaxies show that this method can recover the true inclination with errors of about 1 – 5 degrees in the range  $30^\circ < i < 70^\circ$ , regardless of the spatial resolution. Nevertheless, in most cases, it is advisable to manually provide an initial guess for the inclination, which is also the most critical parameter to fit (see also Begeman, 1987).
- $V_{\text{rot}}$ : the initial rotation velocity is calculated as the inclination-corrected half-width of the global line profile at 20% of the peak flux ( $W_{20}$ ). This is a measure of the maximum circular velocity reached by the rotation curve.
- $\sigma_{\text{gas}}$  and  $z_0$ : default values for the velocity dispersion and the disk thickness are  $8 \text{ km s}^{-1}$  and  $150 \text{ pc}$ , respectively. Unlike the geometrical parameters, the initial values for  $V_{\text{rot}}$ ,  $\sigma_{\text{gas}}$  and  $z_0$  do not usually affect the goodness of the fit.

### 2.5.3 Masking

In order to obtain a good fit, <sup>3D</sup>BAROLO builds a mask to identify the regions that are ascribable to the galaxies in the data-cube. Only these regions are used during the minimization procedure, hence the choice of the mask is very important to obtain the best kinematic models. The mask should not exclude parts of the galaxy emission belonging to the most extreme velocity channels, which contain information on the rotation velocity.

The default algorithm takes advantage of the source finder and builds the mask directly on the identified emission regions. In this case, the user can set the parameters of the mask through the parameters of the searching algorithm, in particular the primary threshold for source identification and the secondary threshold for source growing (see Section 2.5.1). A simple sigma-clipping or threshold-clipping is also possible. As an alternative to have larger masks, <sup>3D</sup>BAROLO can smooth the original data-cube by a factor  $n$  and consider only the regions where the flux is higher than  $m$  times the spread of noise distribution in the smoothed data-cube. Default values are  $n = 2$  and  $m = 3$ , but they can be changed by the user. Finally, the users

can provide their own made mask in the form of a FITS file or decide to not use a mask.

#### 2.5.4 Regularization of the parameters

Fitting the geometrical parameters together with the kinematic parameters can lead to unphysical results, like discontinuities or jumps in the derived rotation curve. The fits of the inclination and the position angle, in particular, often show unrealistic oscillations and numerical scatter. The usual approach for dealing with this issue, also in the 2D tilted-ring model, consists in dividing the kinematic modeling via a series of fitting runs. Initial runs are used to constrain the geometrical parameters, progressively reducing the number of free parameters to fit. Once the geometry of the disk is satisfactorily determined, the final run can be performed by fitting only the rotation velocity. In this last step, geometrical parameters can be fixed to some constant value or assumed to vary accordingly to some functional form that can describe, for instance, a warp in the external regions. <sup>3D</sup>BAROLO can automatically perform a similar parameter regularization in two steps. After a first fitting run, <sup>3D</sup>BAROLO can interpolate the trend of geometrical parameters by using a polynomial function of degree  $m$  (chosen by the user, default  $m = 3$ ) or a Bezier function. The second fitting step is then performed by leaving free only the rotation velocity and the velocity dispersion and fixing everything else to the derived functional form. This two-stage fitting approach usually guarantees a better stability of the final solution (see [Section 3.1](#)).

#### 2.5.5 Errors

There is no direct way to calculate the errors on the fitted parameters in the 3D approach. In 2D tilted-ring models the quoted errors are usually the sum of the nominal error on the fit, the difference between the values obtained by fitting the entire disk at the same time and the values obtained by individually fitting the approaching and the receding halves of the disk (e.g., Swaters, 1999). In a 3D modeling, such a procedure would be expensive from a computational point of view, since it would require at least three fitting runs.

We rather decided to estimate the errors via a Monte-Carlo method. Once the minimization algorithm converges to the best set of parameters, <sup>3D</sup>BAROLO calculates a number of models by changing the parameters with random Gaussian draws centered on the minimum of the function. All the parameters are varied together, including those that have been kept fixed during the fit. This allows the code to oversample the parameters space close to the minimum. In this region, the residuals usually have the behavior of a polynomial function. Errors for each parameter are taken as the range where this function shows a residuals increase

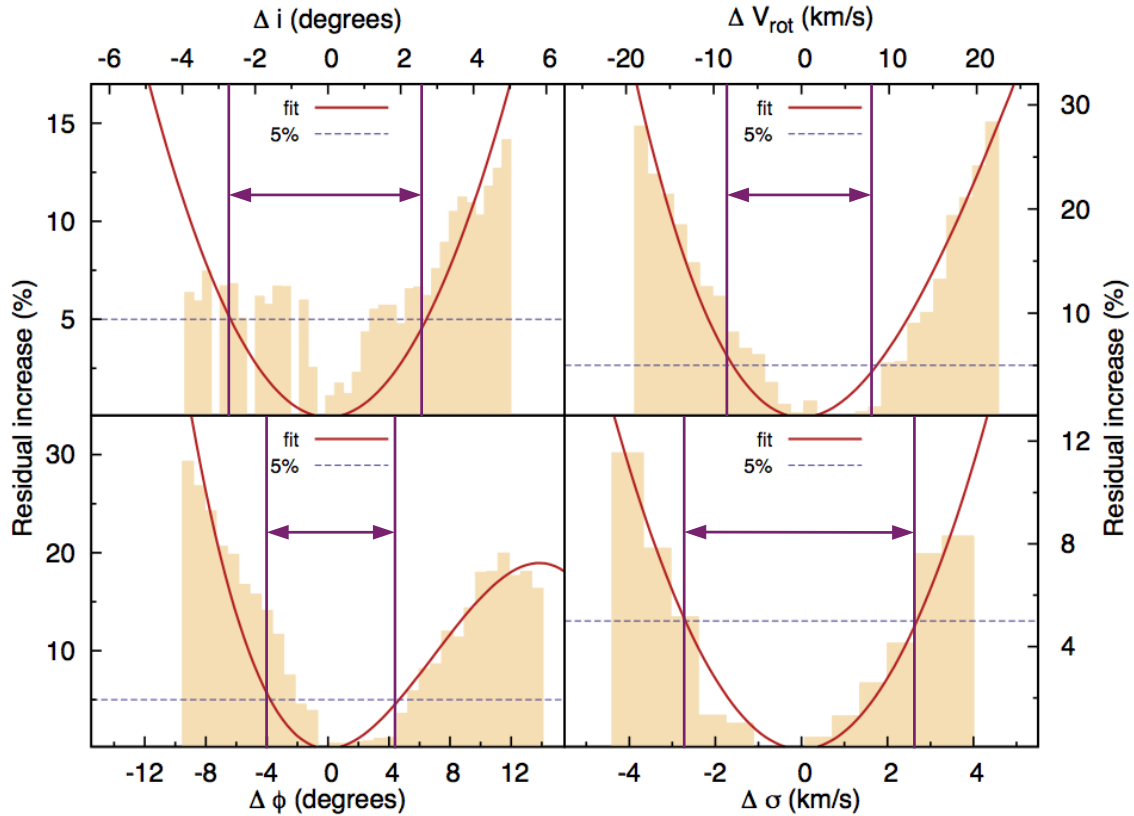


**Figure 2.7:** Error estimate in  $3^{\text{D}}$ BAROLO for the fit at a certain radius of the galaxy NGC 3198 (see Section 3.1). Orange histograms show the residual increase for four model parameters, i.e.  $i$ ,  $\phi$ ,  $V_{\text{rot}}$  and  $\sigma_{\text{gas}}$ . The red lines represent a least-square interpolation with a polynomial function of third degree, dotted lines indicate the 5% increase of residuals with respect to the minimum. The error intervals derived for each parameter are shown by the purple arrows.

of a  $n$  percentage with respect to the minimum (default value is 5%), as shown in Figure 2.7. The advantage of this method is that the error on the single parameter is determined by the errors of all other parameters together, since the parameters of the model are not independent from each other. Albeit this procedure is not optimal and slightly computationally expensive, it returns errors which are in good agreement with those obtained with more standard methods used for the 2D modeling.

## 2.6 Running $3^{\text{D}}$ BAROLO

$3^{\text{D}}$ BAROLO can be downloaded at the website <http://editeodoro.github.io/Bbarolo>, in the form of pre-compiled binaries, supporting Linux/GNU and MacOS X operating systems, or source code to be compiled for any UNIX-based machine.  $3^{\text{D}}$ BAROLO is written in C/C++ programming languages and requires a few external libraries, i.e. CFITSIO library for FITS file handling, WCSLIB library for celestial coordinates

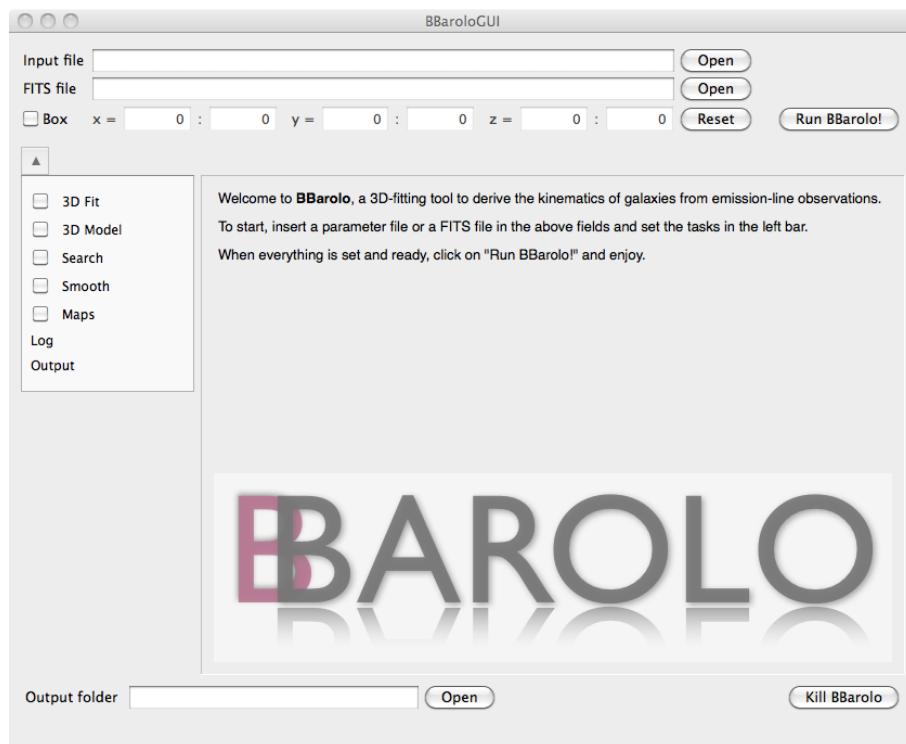


**Figure 2.8:** Graphical User Interface of  $3^{\text{D}}$ BAROLO. The user can select the utility to run from the list on the left and then set the appropriate parameters. Available utilities are the main 3D fitting algorithm, the built of a simple 3D model similarly to GALMOD routine in GIPSY (no fit), the source finder, the smoothing utility and the extraction of moment maps and P-Vs diagrams. While running, textual outputs from the command-line utility are shown in the “Log” tab. The “Output” tab displays the real-time plots of the fitted parameters when the 3D fitting algorithm is selected.

and FFTW3 library for Fast-Fourier transforms. GNUPLLOT and PYTHON, with ASTROPY and MATPLOTLIB packages, are required to produce the output plots.

The main program runs as a command-line utility. Instructions are passed through an input textual file at the run-time. We also provided a friendly graphical user interface (GUI), based on the QT toolkit, to help the user to set all the necessary parameters to run  $3^{\text{D}}$ BAROLO (Figure 2.8). The GUI works as a front-end to write a proper parameter file and to launch the command-line utility. All the parameters for the different routines available in  $3^{\text{D}}$ BAROLO can be intuitively inputted through an appropriate mask, which provides also some basic instructions. While the program is running, the GUI shows real-time plots to the user, useful to check the goodness of the on-going fit.

$3^{\text{D}}$ BAROLO can be otherwise run directly in the command line through:

```
> BBarolo -option file
```

where `-option` depends on the input that the user wishes to give to  $3^{\text{D}}$ BAROLO. A

brief guide with a list of possible input options can be obtained by setting `-h` as option argument. In this context, `file` is either a FITS file or a parameter file.

In order to execute a fit in automatic mode, the user can simply type:

```
> BBarolo -f file.fits
```

where `file.fits` is the FITS data-cube to be analyzed. With this option, <sup>3D</sup>BAROLO searches for sources in the data-cube, estimates the initial parameters and performs the two-steps fit for each detected galaxy. A more customizable way to run <sup>3D</sup>BAROLO is by the following command:

```
> BBarolo -p paramfile
```

where `paramfile` is a text file containing a list of parameters and their values, using the following syntax:

```
par1Name    par1Value  
par2Name    par2Value  
...         ...
```

A list of available parameters with their default values can be obtained by running `BBarolo -d`. A deeper description of the 3D fitting parameters is available at the <sup>3D</sup>BAROLO website.

At the end of a fitting run, <sup>3D</sup>BAROLO produces a number of standard outputs, including a FITS data-cube of the model, a FITS data-cube of the mask, FITS images of the position-velocity diagrams along the major and minor axes of both the data and the model, comparative data-model plots of the channel maps, P-V diagrams and moment maps, a plot and a textual file of the model parameters.



## HI kinematics of local star-forming galaxies<sup>†</sup>

**ABSTRACT** — In this Chapter, we use the software <sup>3D</sup>BAROLO to derive rotation curves and velocity dispersion profiles of local galaxies using HI data from high to very low spatial resolution. By comparing interferometric and single-dish observations and using simulated galaxies, we show that <sup>3D</sup>BAROLO can recover the true rotation curve and the intrinsic velocity dispersion even in barely resolved systems ( $\sim 2$  resolution elements per galaxy side) provided that the S/N of the data is larger than 2-3. In some cases, the rotation curves derived with <sup>3D</sup>BAROLO rise more steeply than those derived before with other techniques. Intrinsic velocity dispersions are always of the order of 10 km/s and do not significantly increase in the inner regions.

In the previous Chapter, we have presented <sup>3D</sup>BAROLO and described its functionality and features. In this Chapter, we show the potentiality of our 3D fitting algorithm in different observational situations and discuss its points of strength and weakness with respect to the traditional 2D techniques.

To date, <sup>3D</sup>BAROLO has been extensively tested both on simulated galaxies and on over one hundred real galaxies, mostly observed in the HI line and in optical recombination lines, in particular the H $\alpha$  line and the [OII]-line doublet. In this Chapter, we use <sup>3D</sup>BAROLO to derive the kinematics of several nearby galaxies from HI data-cubes with a wide range of spatial resolutions. As mentioned in [Section 2.2](#), the main limitation of 2D approaches is the beam smearing, an effect that is more and more pronounced as the size of the observational PSF increases. We therefore compare our results with those obtained using the traditional 2D techniques and we study how <sup>3D</sup>BAROLO and 2D algorithms perform at different spatial resolutions.

---

<sup>†</sup>Based on [E. M. Di Teodoro & F. Fraternali, 2015, MNRAS, 451, 3021](#)

We start with high-resolution interferometric observations of a sample of well-known spiral galaxies (Section 3.1) and we verify that <sup>3D</sup>BAROLO’s results are consistent with those obtained from 2D velocity fields. In Section 3.2, we use <sup>3D</sup>BAROLO in a semi-blind fashion to derive the rotation curves of a sample of late-type dwarf galaxies at mid-low resolution. We discuss <sup>3D</sup>BAROLO’s efficiency and reliability in this situation where a 2D approach would have required a manual and time-consuming revision to properly handle the beam smearing effect. In Section 3.3, we test the performance of <sup>3D</sup>BAROLO in very-poor spatial-resolution data. We use single-dish observations of local galaxies with 2-4 resolution elements across the whole disk and we show that <sup>3D</sup>BAROLO can still recover the true values of rotation velocities and velocity dispersions that we find with high-resolution data. Finally, in Section 3.4, we test the accuracy and the limits of <sup>3D</sup>BAROLO by running it on simulated galaxies, both with flat and with slowly-rising rotation curves, “observed” with different spatial/spectral resolutions, inclination angles and noise levels.

### 3.1 High-resolution data

We run <sup>3D</sup>BAROLO on several high-resolution galaxies from the available HI-surveys, like The HI Nearby Galaxy Survey (THINGS, Walter et al., 2008), the Very Large Array - ACS Nearby Galaxy Survey Treasury (VLA-ANGST, Ott et al., 2012) and the Hydrogen Accretion in LOcal GALaxies Survey (HALOGAS, Heald et al., 2011). We verified that <sup>3D</sup>BAROLO can successfully model all these high-resolution galaxies and that the derived rotation curves agree very well with the already published 2D rotation curves.

Here we focus on the automatic modeling of four well-known nearby spiral galaxies: NGC 2403, NGC 2903, NGC 3198 and NGC 5055. Among these, NGC 5055 is an interesting and difficult case because it has a prominent warp in the outer disk (Bosma, 1978; Battaglia et al., 2006). We used natural-weighted data-cubes from the THINGS survey<sup>1</sup>. Natural-weighted data-cubes are more sensitive to surface brightness than robust-weighted data (Briggs, 1995), whereas robust-weighted data-cubes guarantee a higher spatial resolution. The beam FWHMs are 8'' for NGC 2403 (about 0.12 kpc, assuming a distance of  $D = 3.2$  Mpc), 15'' for NGC 2903 (0.65 kpc at  $D = 8.9$  Mpc), 11'' for NGC 3198 (0.65 kpc at  $D = 13.8$  Mpc) and 10'' for NGC 5055 (0.49 kpc at  $D = 10.1$  Mpc). Typical channel width for all galaxies is  $5 \text{ km s}^{-1}$ . The modeling of the same four galaxies but observed at very low spatial resolution with single-dish telescopes will be later shown in Section 3.3.

We run <sup>3D</sup>BAROLO by supplying only initial guesses for the inclination and the

---

<sup>1</sup>Natural and robust weighted HI data-cubes and moment maps are publicly available at the THINGS website: <http://www.mpia.de/THINGS/Data.html>

position angle.  ${}^3\text{D}$ BAROLO automatically identifies the galaxy emission in the data-cube through the source finder (Section 2.5.1), builds the mask (Section 2.5.3), estimates the initial guesses for all the other parameters (Section 2.5.2), performs the first fitting step for each radius with all the parameters free and the second fitting step with only  $V_{\text{rot}}$  and  $\sigma_{\text{gas}}$  free, after the regularization of the other parameters by Bezier functions (inclination and position angle) or constant values (Section 2.5.4).

Figures 3.1, 3.2, 3.3 and 3.4 show the comparison between the observations and the final best-fit models and the resulting values of the fitted parameters. All plots are standard outputs of  ${}^3\text{D}$ BAROLO. Upper panels show data-model comparisons through seven representative channel maps (*top panel*) and position-velocity diagrams taken along major and minor axes (*middle panel*). The channel closest to the systemic velocity is shown in the center. Both channel maps and P-Vs are extracted from data-cubes smoothed at  $30''$ , in order to improve the graphical representation. Models are shown in red, observations in blue. On the major axis P-Vs we overlapped the projected rotation curves (green dots) derived with  ${}^3\text{D}$ BAROLO. These observations have an uneven noise distribution, with large negative bands around the galaxy emission, very evident in NGC 2403 and NGC 5055. Despite this,  ${}^3\text{D}$ BAROLO is able to reproduce the data very well. In particular, for NGC 5055, the model traces the details of the prominent warp visible as a deformation of the channel maps in the outer regions of the galaxy (Figure 3.4). The inspection of the P-Vs along the major axes reveals that all these galaxies have some amount of extra-planar gas. This gas is visible as emission at anomalous line-of-sight velocities (see e.g., Figure 3.2), which is often referred to as the galaxy “beard” (Sancisi et al., 2001). Our single-disk model can not reproduce this kinematic feature, but it can be useful to separate the disk component from the anomalous extra-planar component (see Fraternali et al., 2002).

The bottom panels of Figures 3.1 - 3.4 show the resulting values of the derived parameters in the first (grey dots) and in the second (red) fitting steps. We compare our findings with the results of de Blok et al. (2008), shown in cyan and obtained by a tilted-ring fit on the velocity fields extracted from the same datasets. Note how the regularization of the geometrical parameters improves in some cases the final rotation curves, for example removing the unphysical oscillations around 28 and 47 kpc in NGC 5055. Overall, our final rotation curves are in very good agreement with those derived by de Blok et al. (2008). The main differences arise from kinematic asymmetries between the approaching and the receding halves of the galaxies. While the 2D tilted-ring model applied to the entire disk in an asymmetric galaxy mainly results in a rotation curve usually averaged between the approaching and the receding side,  ${}^3\text{D}$ BAROLO always finds the model that has the lowest residuals with respect to the data. This may result in a rotation velocity that is the average between the two halves, or that follows more closely one side rather than the other.

This is what happens to our rotation curves, as it is evident looking, for instance, at the P-V diagram along the major axis of the galaxy NGC 2403, where the model preferentially follows the receding side of the galaxy (Figure 3.1).

The computational time with a regular dual-core laptop for running <sup>3D</sup>BAROLO on these THINGS data-cubes, sized  $1024 \times 1024 \times n$  pixels, with  $n$  ranging from 60 to 90, is about 1-2 days. High-resolution observations are also suitable to study asymmetries and peculiarities on the sub-kpc scale, such as streaming motions, lopsidedness and extra-planar gas. <sup>3D</sup>BAROLO always models galaxies with a single rotating disk and it is not designed to handle these peculiarities. In this context, the newest 2D fitting codes, like DISKFIT (Spekkens & Sellwood, 2007; Sellwood & Sánchez, 2010), might be a more desirable choice, since they guarantee larger possibilities for modeling kinematic and/or geometrical anomalies. The 3D TiRiFiC code (Józsa et al., 2007) also provides for wide possibilities of complex modeling, even for those systems where the 2D approach can not be used, like galaxies close to edge-on or having thick disks (e.g. Kamphuis et al., 2013; Schmidt et al., 2014).

### 3.2 Mid-low resolution data and robustness

Only a fraction of local galaxies can be observed with a spatial resolution comparable to that of the THINGS survey. Most emission-line observations of galaxies, both from radio-interferometers and IFU instruments, currently have less than a dozen resolution elements throughout the entire disk. In these conditions, the beam smearing could heavily affect the derivation of rotation curves with 2D techniques. <sup>3D</sup>BAROLO is instead conceived to work with these low-resolution data.

We made a robustness test by using a sample of galaxies from the Westerbork HI survey of Irregular and Spiral galaxies Project (WHISP, van der Hulst, van Albada & Sancisi, 2001). WHISP comprises approximately 350 galaxies in the Local Universe observed in HI with the Westerbork Synthesis Radio Telescope (WSRT). We selected 32 galaxies with published reliable rotation curves (Swaters, 1999). The sample only contains dwarf late-type galaxies, with  $V_{\text{rot}} \lesssim 100 \text{ km s}^{-1}$ , that usually have a poor spatial resolution and a relatively low signal-to-noise ratio (S/N). For these galaxies, Swaters derived rotation curves using the following procedure that includes a correction for the beam smearing. For each galaxy, a first estimate of the rotation curve was determined by interactively fitting the rotation velocity, position angle and inclination as a function of radius simultaneously to a set of six position-velocity diagrams taken at different angles. This was done by using the INSPECTOR routine in the GIPSY package, which allows to visually inspect different slices and manually tune up the parameters. Centres were fixed to the optical values, the systemic velocities were determined from a tilted-ring fit to the velocity field with

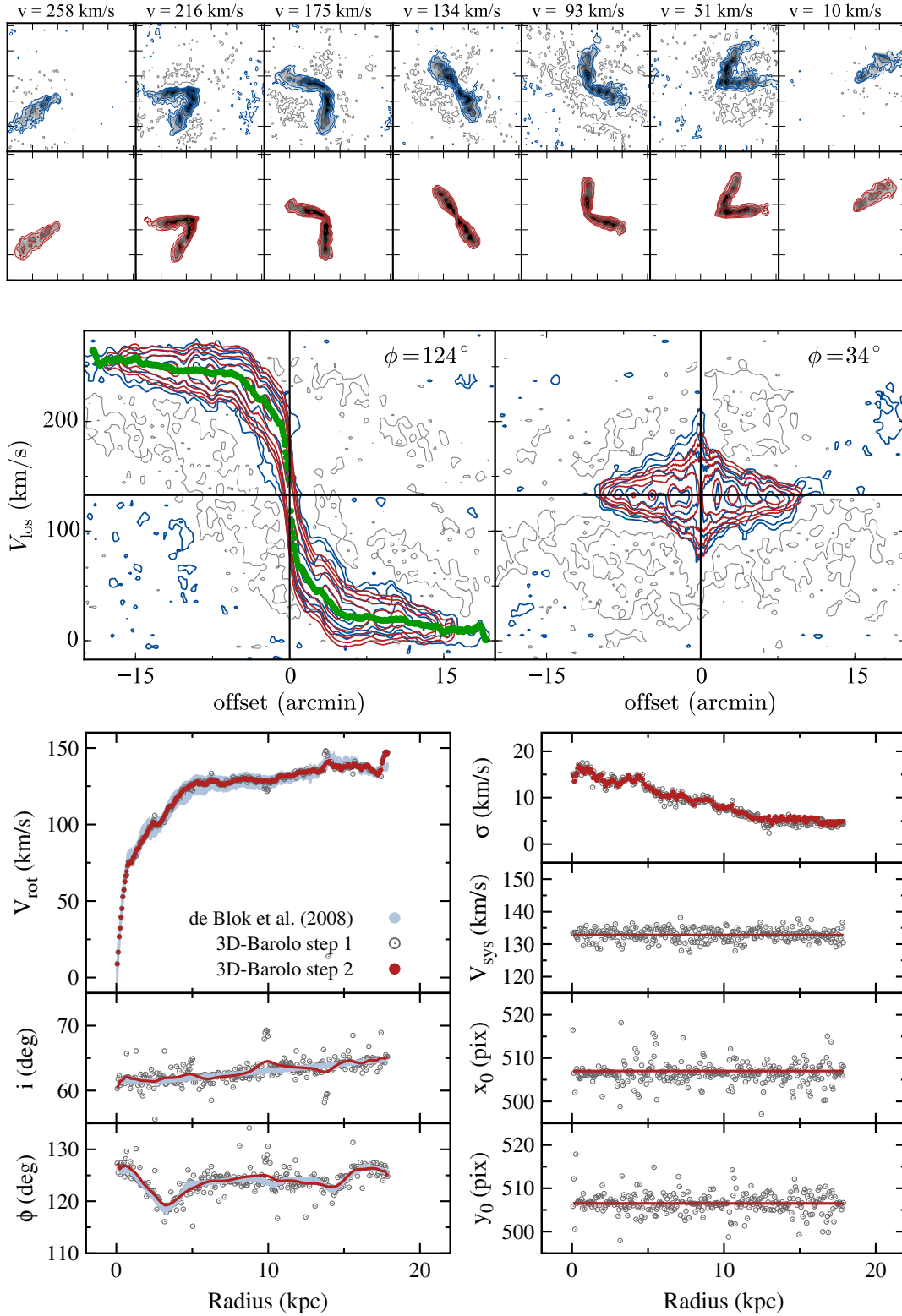


**Figure 3.1:**  $3^{\text{D}}$  BAROLO automatic fit of the galaxy NGC 2403 from THINGS data. *Top and middle panels:* comparison between model (red) and data (blue) through seven channel maps and P-V diagrams, respectively. Lower contours are at  $l = 2.5\sigma_{\text{noise}}$  level, following contours are  $2^n \times l$ . Negative contours at  $-2^n \times l$  are in grey. The projected rotation curve is shown in green on the major axis P-V. *Bottom panels:* derived tilted-ring parameters. The grey-empty dots represent the first fit with all parameters kept free. The red full dots or lines represent the second fit of  $V_{\text{rot}}$  and  $\sigma_{\text{gas}}$  after the regularization of the other parameters (Bezier interpolation for  $i$  and  $\phi$ , constant value for  $V_{\text{sys}}$ ,  $x_0$  and  $y_0$ ). The cyan-shadowed region and the cyan-dashed lines are the rotation curve (with errors) and the geometrical angles derived by de Blok et al. (2008) with a 2D fit.

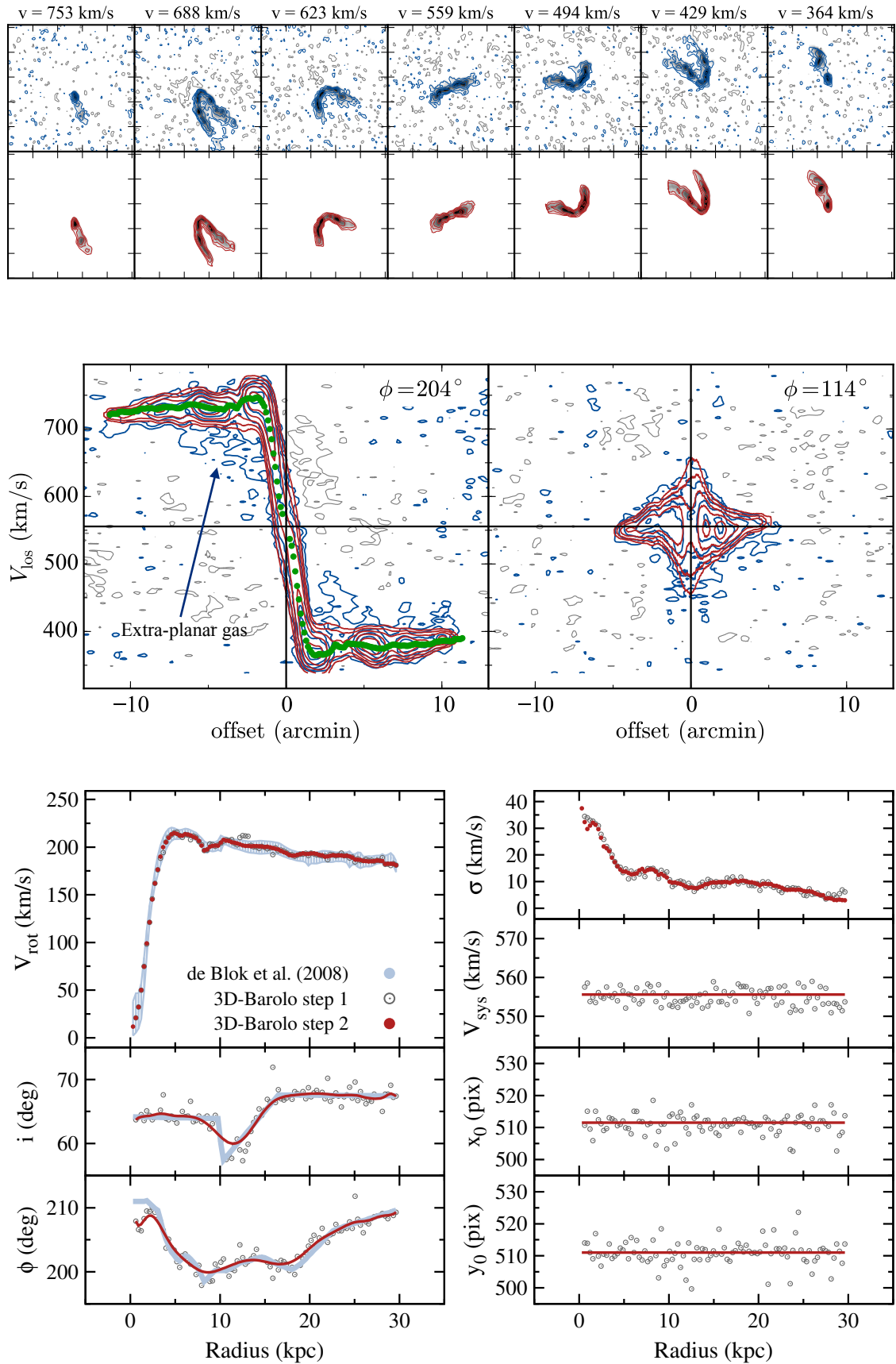


Figure 3.2: Same as Figure 3.1 for the galaxy NGC 2903 from THINGS data.

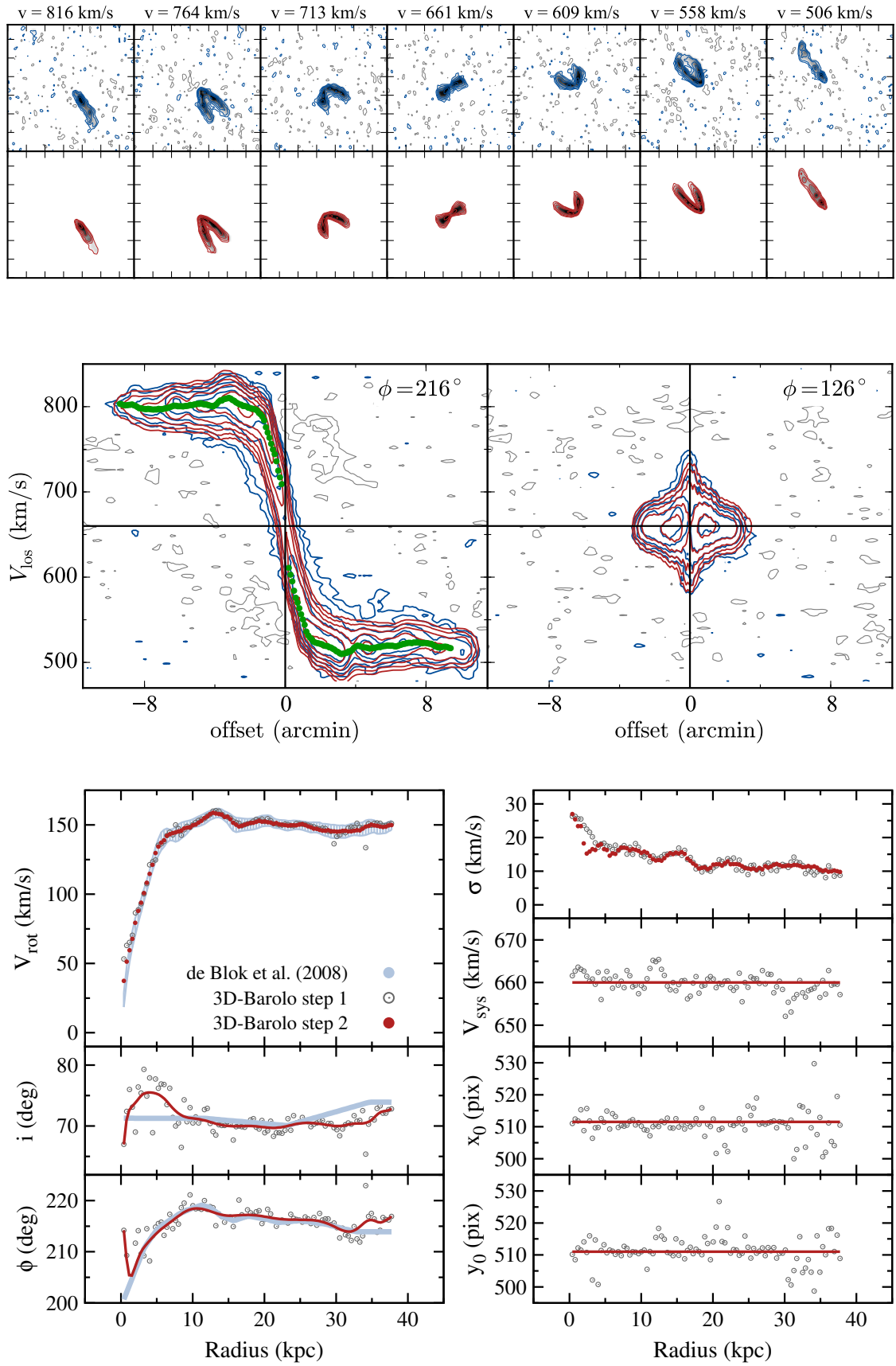
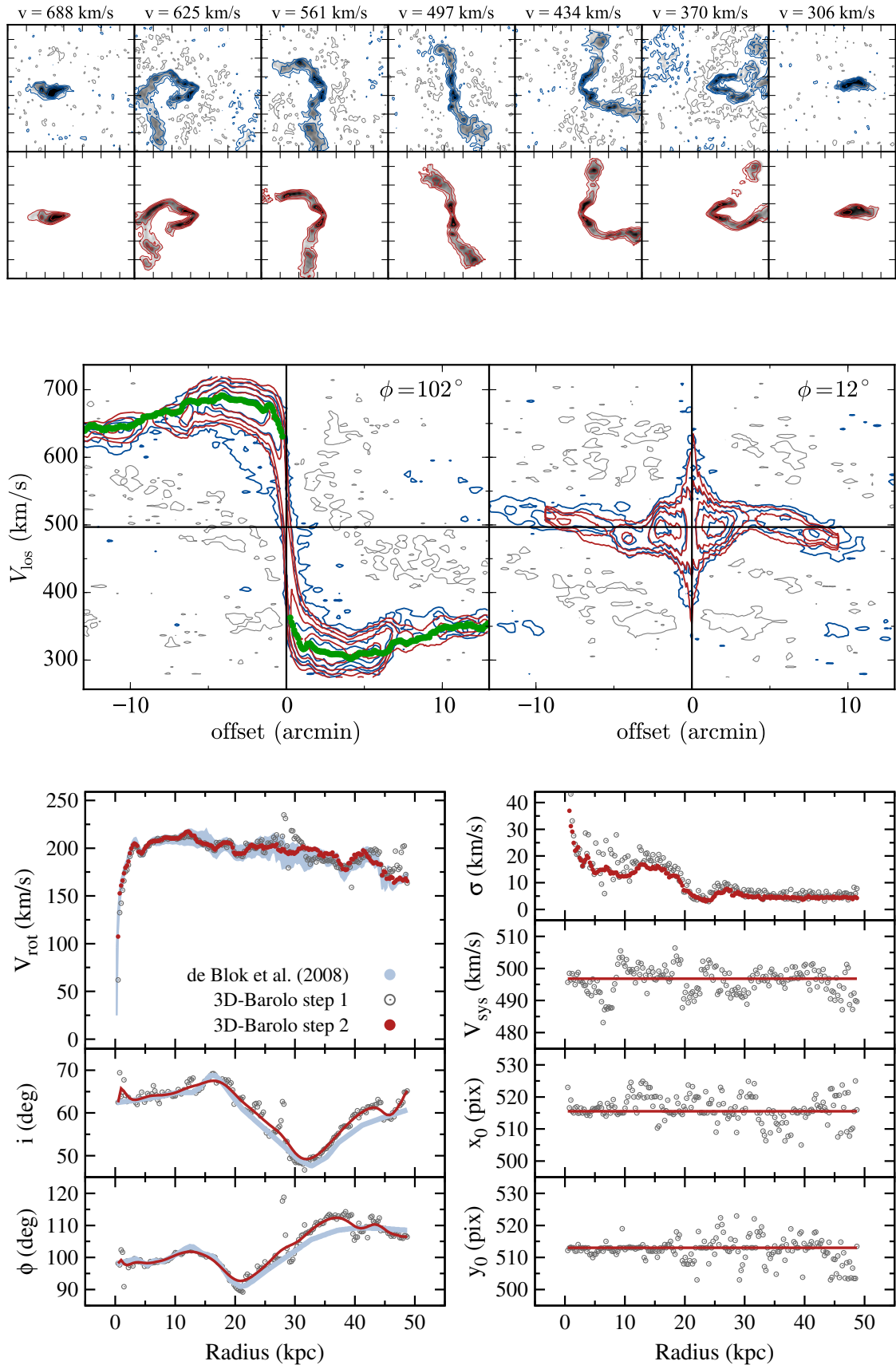


Figure 3.3: Same as Figure 3.1 for the galaxy NGC 3198 from THINGS data.



**Figure 3.4:** Same as Figure 3.1 for the warped galaxy NGC 5055 from THINGS data.

the centre fixed. Then, [Swaters](#) constructed a 3D model (using GALMOD in GIPSY) from the estimated parameters and he visually compared it with the observations, iteratively adjusting the input rotation curve and building a new 3D model until the match between model and observation was satisfactory. Such a procedure takes a long time for each galaxy and it may be subjective, but it was the only way to take into account the beam smearing effect and derive reliable rotation curves in these low-resolution data. The approach of <sup>3D</sup>BAROLO is analogous, but every step is automatically performed and the best model is quantitatively determined.

We run <sup>3D</sup>BAROLO in a semi-blind fashion on the sample of 32 dwarf galaxies. We used 30'' smoothed data-cubes<sup>2</sup> and we set a ring width of 15'', following [Swaters \(1999\)](#). The systemic velocities and the coordinates of the centre of the galaxies were automatically estimated through the source finding algorithm and fixed to those values. In each case, values perfectly compatible with those of [Swaters \(1999\)](#) were obtained: the maximum deviations from Swaters values are  $\Delta V_{\text{sys}} < 2 \text{ km s}^{-1}$  and  $\Delta x_0 \simeq \Delta y_0 < 1 \text{ pixel} = 10''$ . Global initial estimates for rotation velocities, velocity dispersions and thicknesses of the disks were set to  $V_{\text{rot}} = 50 \text{ km s}^{-1}$ ,  $\sigma_{\text{gas}} = 8 \text{ km s}^{-1}$  and  $z_0 = 200 \text{ pc}$  for all galaxies, while the initial inclinations and the position angles were taken from Tab. A1, Chap. 4 of [Swaters \(1999\)](#). We used the  $|M - D|$  residuals with a  $\cos(\theta)$  weighting function (see [Section 2.4.4](#)). Masks were built by smoothing the data by a factor 2 and considering only those regions with flux  $> 3\sigma_{\text{noise}}$ , being  $\sigma_{\text{noise}}$  the root mean square (noise) of the smoothed data-cube. <sup>3D</sup>BAROLO performed a first step by fitting  $V_{\text{rot}}$ ,  $\sigma_{\text{gas}}$ ,  $i$  and  $\phi$  and a second step by fitting only  $V_{\text{rot}}$  and  $\sigma_{\text{gas}}$  and fixing  $i$  and  $\phi$  to a 2<sup>nd</sup> degree polynomial function. The execution time is less than a minute per galaxy on a regular laptop.

Position-velocity diagrams along major and minor axes for all galaxies are shown in [Figure 3.5](#). A comparison between Swaters' rotation curves and ours is shown in [Figure 3.6](#). In general, the agreement is very good. Most differences in the rotation velocities can be attributed to asymmetries in the kinematics between the receding and approaching halves of the galaxies. It is interesting to notice that in some galaxies our rotation curves rise more steeply than those of Swaters in the inner regions (e.g. UGC 5272, UGC 6446, UGC 9211). Since the main effect of the beam smearing is to reduce the velocity gradients in the rising part of the rotation curve, it is possible that the correction manually made by [Swaters](#) was not quite sufficient in those cases.

Out of 32 data-cubes, <sup>3D</sup>BAROLO failed in determining acceptable models for 4 galaxies, either not converging or deriving wrong kinematics. Two cases (UGC 3966, UGC 8837) can be attributed to a wrong fit of the inclination in the first step and fixing it to the initial value led to a good model (see [Figure 3.6](#)). In the last two cases, UGC 7690 and UGC 8490, we could not make the code working

---

<sup>2</sup>Datacubes available at <http://www.astron.nl/wow/>.

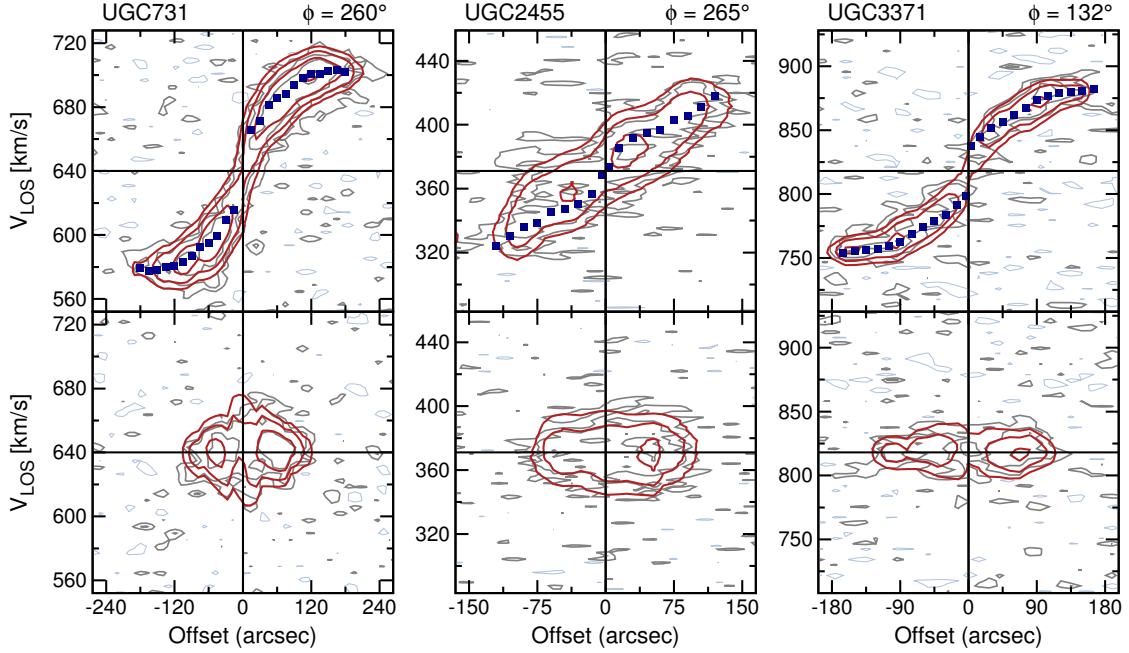


**Figure 3.5:** Comparison between our best models and the HI observations of 30 dwarf galaxies selected from the WHISP sample. For each galaxy we show slices along major and minor axes (outputs of  $3^{\text{D}}$ BAROLO). Data are shown in grey and cyan (negative contours) and the model in red. Dark-blue square are the derived rotation curves. The name of the galaxies and the position angles are shown on the top of the diagrams.

manually neither. The first galaxy is very faint and the fit is hampered by the noise. The galaxy UGC 8490 has a huge warp in inclination and the algorithm tries to reproduce it by varying the rotation velocity rather than the inclination angle. The final model looks good, but the rotation curve is probably unphysical. In addition, from the inspection of the position-velocity diagrams along the minor axis, it turned out that the automatic estimate of the centers was slightly inaccurate in five galaxies. Putting the optical centres manually led to better models, even though the rotation curves did not change significantly. Overall, 94% of the galaxies were accurately modeled by  $3^{\text{D}}$ BAROLO.

From this test emerges that  $3^{\text{D}}$ BAROLO is able to derive reliable kinematics in low-resolution and noisy data-cubes. We remind that we run  $3^{\text{D}}$ BAROLO in a almost blind execution, since the only information we supplied to the code were the initial guesses for the inclination and the position angles. Of these, the inclination is especially critical as it may be unsuccessfully estimated by the code. Improvements in the initial parameters estimate algorithm will be considered in the next releases. We stress however that the careful inspection of the outputs (position-velocity diagrams and model cubes) does clearly single out cases where the fit was not successful.

Our test on the WHISP data reveals that the success rate is very high. This,

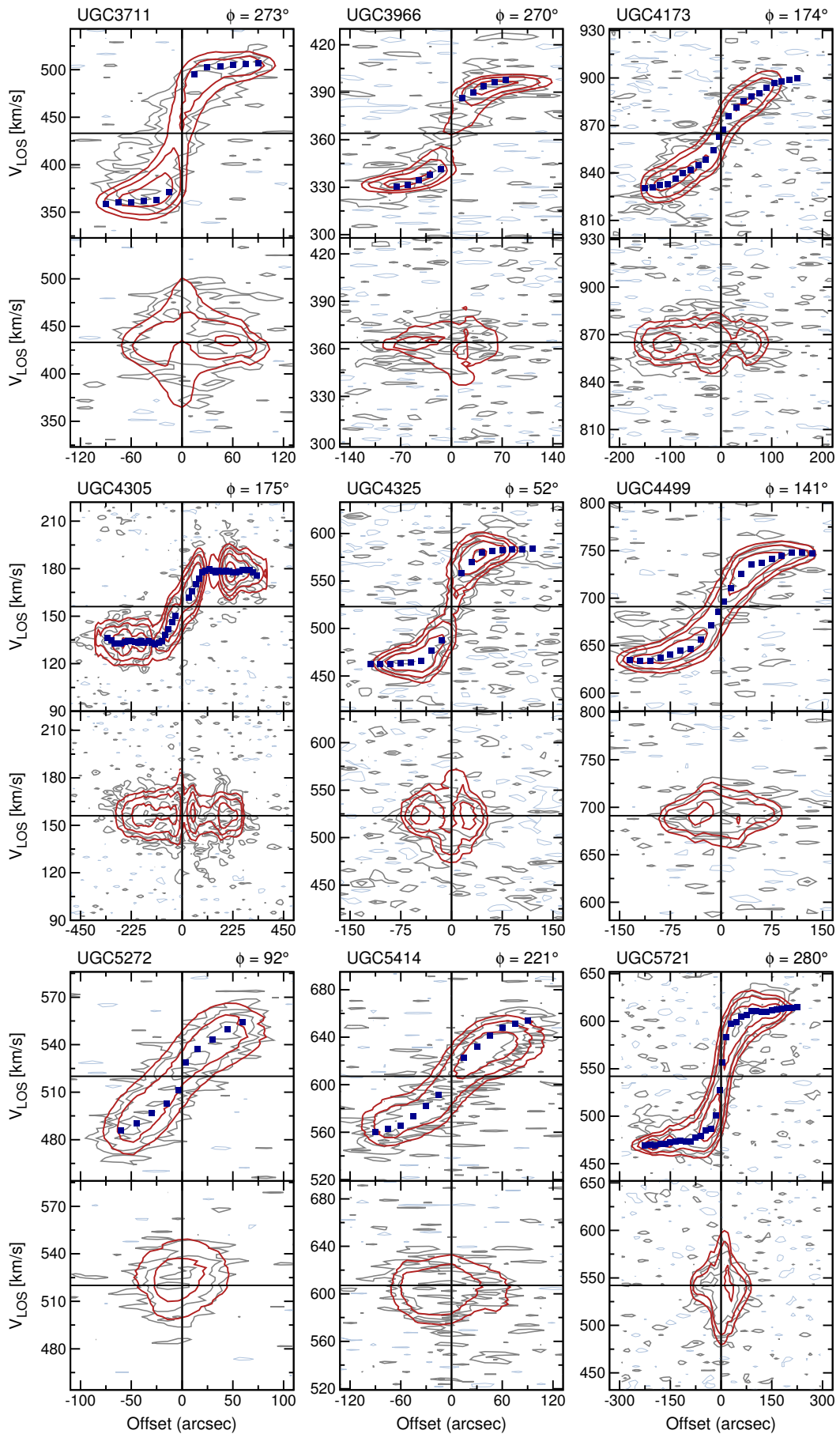


Figure 3.5: Continued

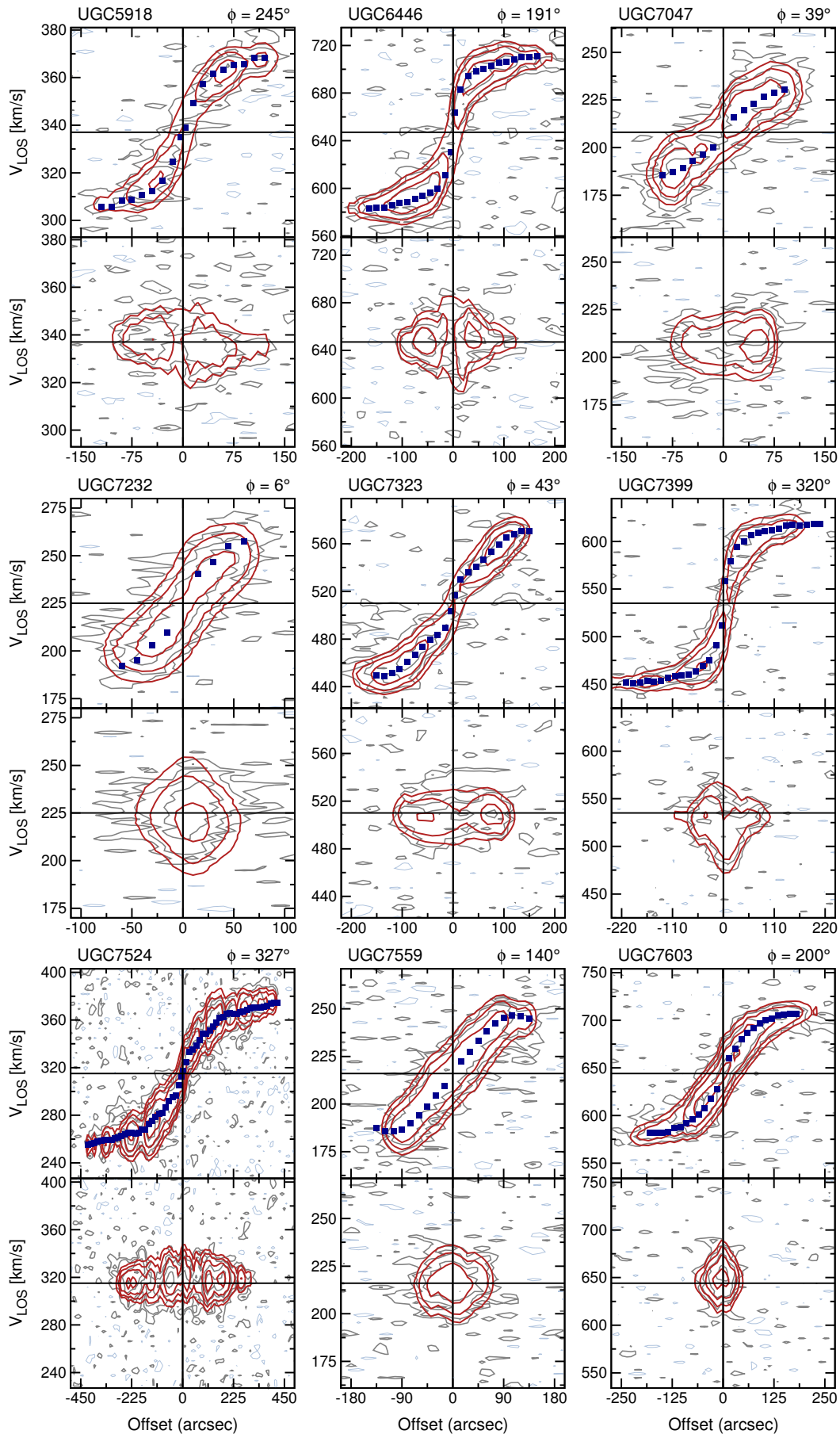


Figure 3.5: Continued

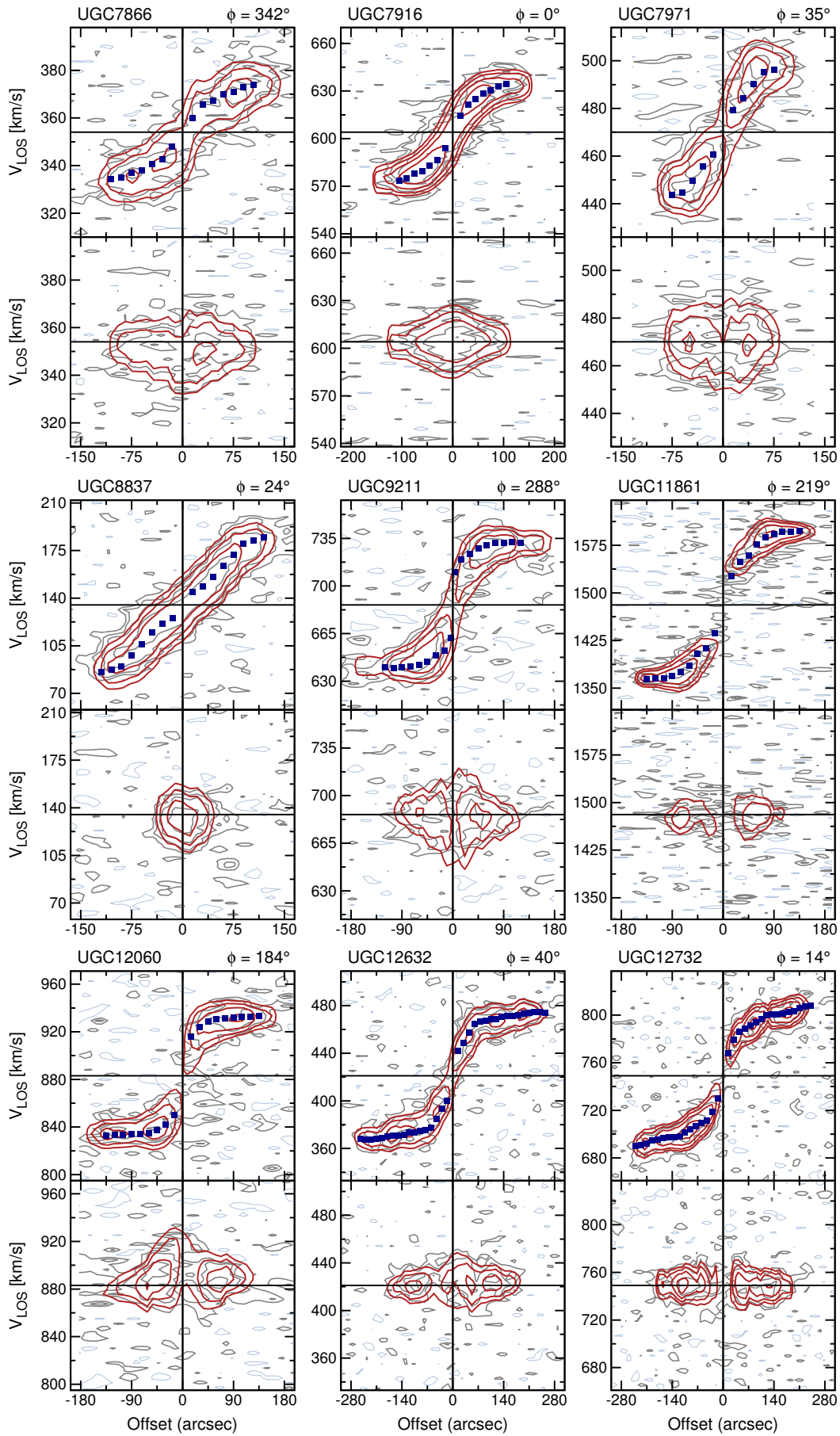
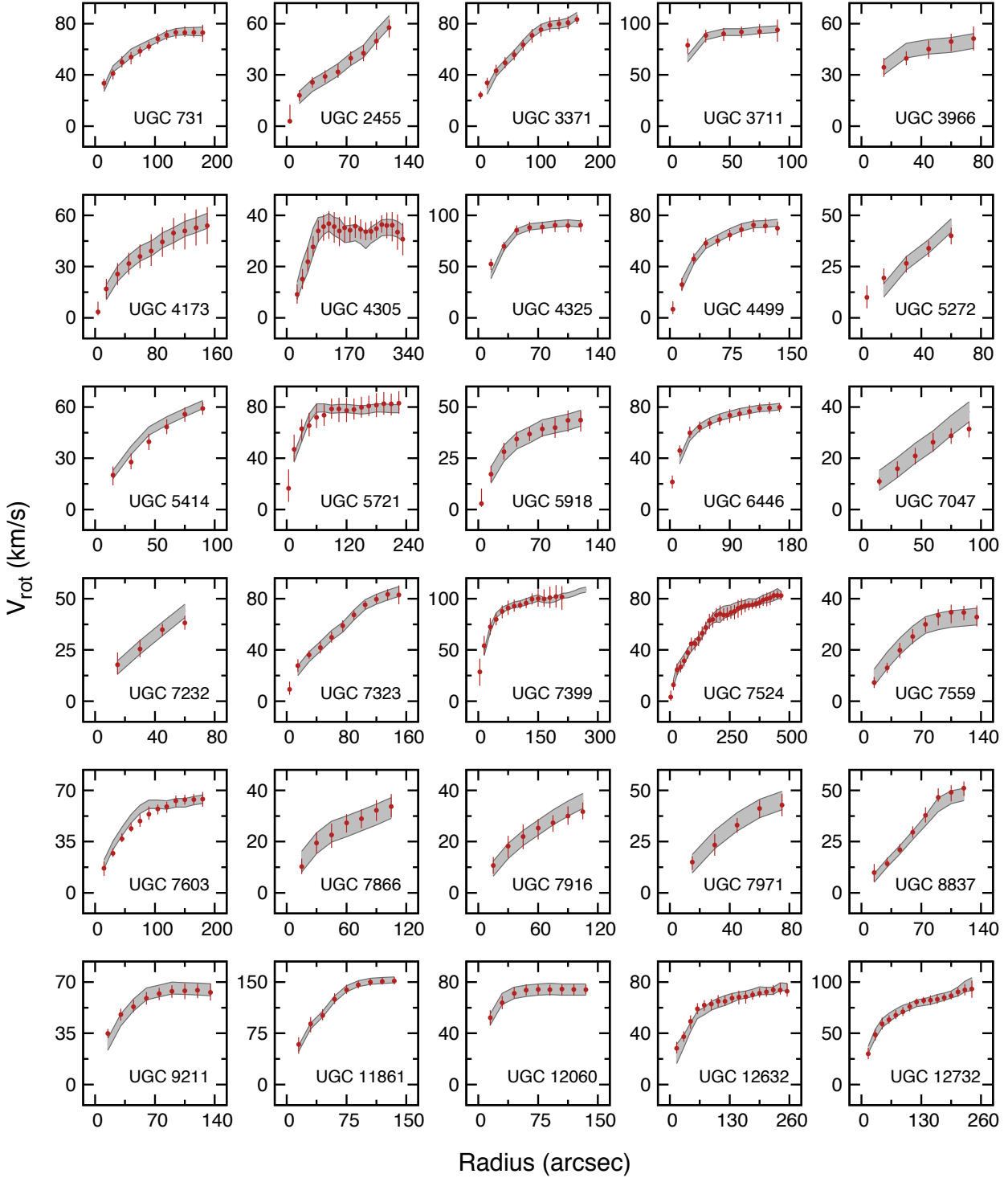


Figure 3.5: Continued



**Figure 3.6:** Rotation curves of the 30 dwarf late-type galaxies selected from the WHISP sample. The gray-shadowed regions represent the rotation curves from Swaters (1999) within the errors, the red dots are the rotation curves derived with  $3^{\text{D}}$ BAROLO. Since Swaters' errors are symmetric, his points would lie in the centre of the grey band at the same radii of our points. In UGC 7399, our rotation curve stops earlier because in our data-cube there was no significant emission beyond about 200 arcsec.

combined with the very low computational time needed to fit these low-resolution galaxies ( $\lesssim 1$  minute on a laptop) are key features for the application of  $^3\text{D}$ BAROLO to the upcoming large HI surveys. Indeed, already planned HI survey, such as WALLABY and DINGO with ASKAP (Johnston et al., 2008), LADUMA with MeerKAT (Booth et al., 2009) and WNSHS with WSRT/APERTIF (Verheijen et al., 2008), are expected to observe thousands of galaxies with spatial resolution comparable to the WHISP galaxies.

### 3.3 Very low-resolution data

In this section we show the effect of the beam smearing on the derivation of rotation curves from 2D and 3D analysis, going down to extremely low spatial resolution.

We run both  $^3\text{D}$ BAROLO and ROTCUR on a small sample of nearby galaxies observed in HI with single-dish telescopes. We selected 4 galaxies (NGC 2403, NGC 2903, NGC 3198 and NGC 5055) for which we have both very high resolution HI data (Fraternali et al., 2002, and THINGS) and single-dish observations. Effelsberg data for NGC 3198 and NGC 5055 were kindly provided by B. Winkel (Winkel, Flöer, & Kraus, 2012; Winkel, Kraus, & Bach, 2012). NGC 2403 (de Blok et al., 2014) and NGC 2903 (Pisano et al., in prep.) were observed with the Green Bank Telescope (GBT) and kindly supplied by D. J. Pisano. We compared high-resolution rotation velocities and velocity dispersions obtained with  $^3\text{D}$ BAROLO with the low-resolution ones derived using both a 2D and our 3D approaches. Typical spatial resolution is 8-10'' for the high-resolution data and 650'' (Effelsberg) or 525'' (GBT) for the low-resolution data, which means that these galaxies are barely resolved. High-resolution rotation curves and dispersions were obtained with  $^3\text{D}$ BAROLO from the natural-weighted THINGS data-cubes as described in Section 3.1.

Low-resolution velocity and dispersion fields were derived as 1<sup>st</sup> and 2<sup>nd</sup> moment maps, respectively (see e.g. NGC 2403, Figure 3.7). In the 2D approach, rotation curves were derived with ROTCUR fitting only  $V_{\text{rot}}$  and fixing the other parameters to the high-resolution values, 2D velocity dispersion profiles were obtained by taking the average value along the rings on the dispersion fields. No correction for the beam smearing was applied.  $^3\text{D}$ BAROLO was run on the low resolution data by fitting only  $V_{\text{rot}}$  and  $\sigma_{\text{gas}}$ , except for NGC 5055, where we kept free also the position angle to trace the outer warp. For NGC 2403, we used only the receding half of the disk, since the approaching half is contaminated by HI emission from the Milky Way.

Figure 3.8 shows the resulting rotational velocities, velocity dispersions and the comparison between the models and the data through the position-velocity diagrams along the major and the minor axes. As expected, the 2D approach is not suitable for data at these resolutions, since the beam smearing significantly affects the derivation

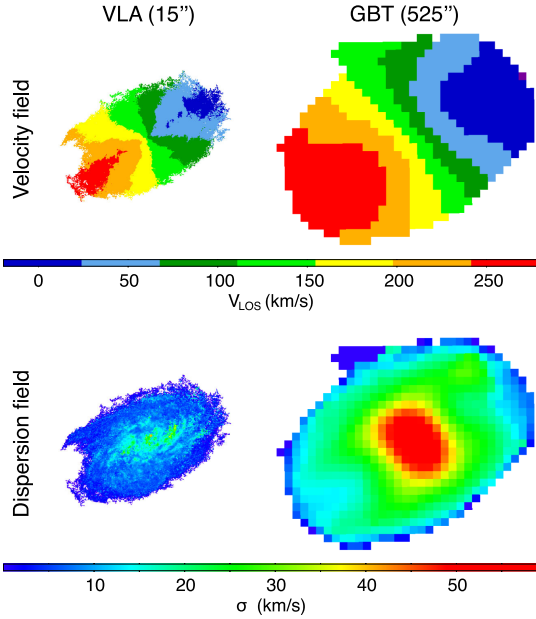


**Figure 3.7:** Velocity fields (1<sup>st</sup> moment) and velocity dispersion fields (2<sup>nd</sup> moment) for NGC 2403 derived from high (*left*, Fraternali et al., 2002) and low resolution (*right*, de Blok et al., 2014) data-cubes. Images are on the same spatial and velocity scale. Note the dramatic effect of the beam smearing: the velocity field at high resolution, showing the typical traits of a flat rotation curve, turns into a nearly solid-body pattern at low resolution, especially in the inner parts. Velocity dispersions increase by a factor 3-4 throughout the whole disk.

of the 2D maps from the data-cubes. Beam smearing flattens the gradients in the velocity profiles and turns rotation velocity into apparent high velocity dispersion (i.e. it broadens the line profiles, Section 2.3), as it clearly appears from the maps in Figure 3.7. Such a degeneracy between  $V_{\text{rot}}$  and  $\sigma_{\text{gas}}$  is broken in <sup>3D</sup>BAROLO, because the beam smearing effect is taken into account in the convolution step (Section 2.4.2). Unlike the 2D approach, <sup>3D</sup>BAROLO recovers correct rotation velocities for all these galaxies in every location of the disk. The differences between the low-resolution and the high-resolution velocities are within the errors in all cases. Even more remarkably, <sup>3D</sup>BAROLO returns low values for the intrinsic velocity dispersions of the gas that are fully comparable with the correct values (bottom panels of the upper plots). An inspection of the position-velocity diagrams along the minor axis (bottom panels of the lower plots) should give an idea of how the line broadening in these low resolution data is fully dominated by instrumental effects (see for comparison, the P-Vs of the same galaxies at high resolution, Figures 3.1 to 3.4).

These results show that <sup>3D</sup>BAROLO is a powerful tool to study the kinematics of galaxies even in very low-resolution data (2-3 resolution elements across the whole disk), where the standard 2D approach fatally fails. Above all, <sup>3D</sup>BAROLO is almost always able to describe the correct shape of the rotation curves and it becomes extremely robust when its outputs are visually checked by the user. A particularly interesting application concerns the Integral Field Spectrographs (IFS) data. Instruments like SINFONI (Eisenhauer et al., 2003), KMOS (Sharples et al., 2008) and MUSE (Bacon et al., 2010) on the Very Large Telescope (VLT) can observe line emission, such as H $\alpha$ , N and O forbidden lines, in galaxies up to redshift about 2.5, with a resolution similar to the observations showed in this section. Running

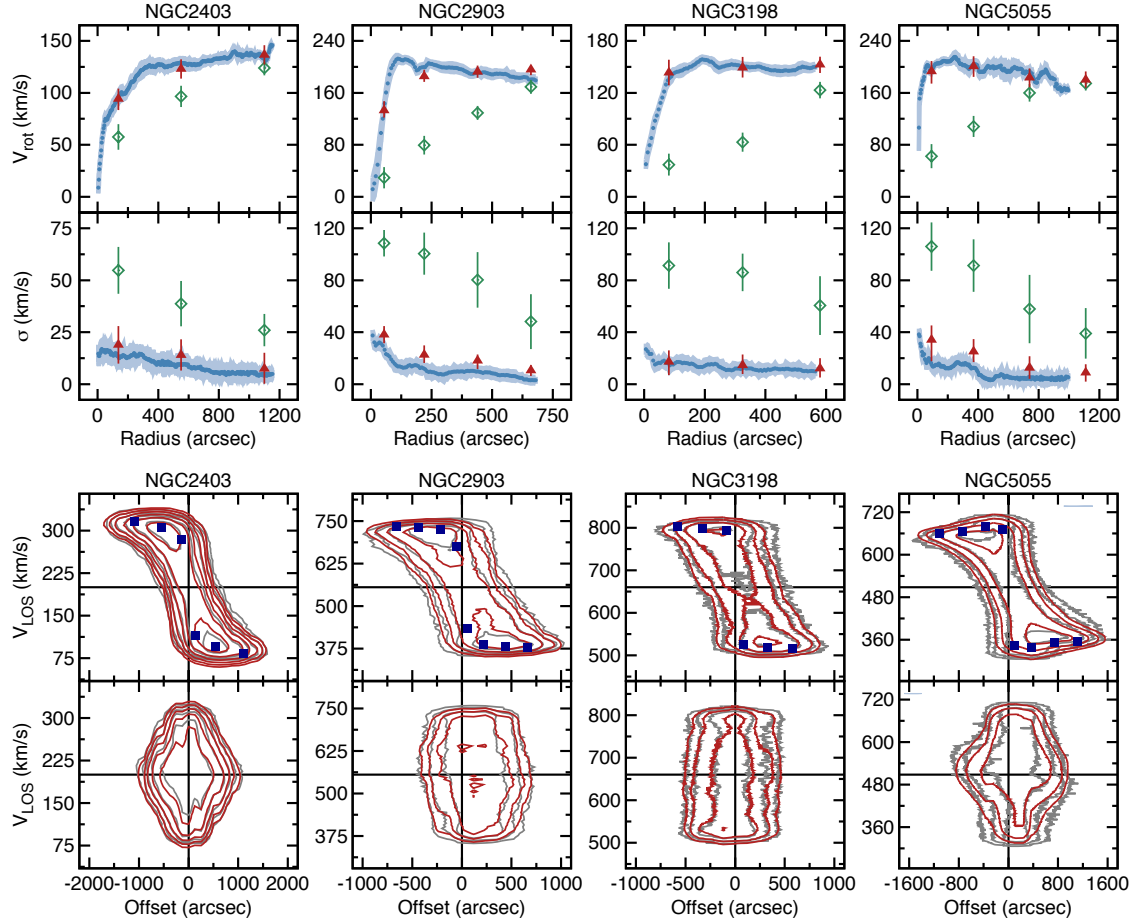


**Figure 3.8:** *Upper panels:* velocities (*top*) and velocity dispersions (*bottom*) for NGC 2403, NGC 2903, NGC 3198 and NGC 5055. Data of NGC 2403 and NGC 2903 are from the GBT (PSF=525''), data of NGC 3198 and NGC 5055 are from the Effelsberg telescope (PSF=650''). Blue dots were derived from THINGS high-resolution (about 10'') data-cubes with <sup>3D</sup>BAROLO. Cyan regions represent the errors. Red triangles are the fit with <sup>3D</sup>BAROLO in single-dish data, the green open diamonds are the results obtained from the 2D maps (ROTCUR on velocity fields and ELLINT on dispersion fields). *Lower panels:* the correspondent position-velocity diagrams along major (*top*) and minor (*bottom*) axes. Data are represented in grey, models in red, rotation curves as blue square dot.

<sup>3D</sup>BAROLO on those data-cubes is a challenging task because, in addition to the poor spatial resolution, these observations have a low spectral resolution (channel widths of 30-40 km s<sup>-1</sup> compared to the few km s<sup>-1</sup> of HI data) and very low S/N. Nevertheless, a 3D approach should be heartily recommended in order to take advantage of the full information available in these data-cubes. In [Chapter 5](#), we present the application of <sup>3D</sup>BAROLO to a sample of high-*z* star-forming galaxies observed with KMOS.

### 3.4 Testing <sup>3D</sup>BAROLO's limits

The goodness of a fit is mainly determined by the combination of four factors: the inclination of the galaxy disk, the spatial resolution, the spectral resolution and the S/N. We used mock galaxies to find some significant thresholds to these quantities and test under what conditions <sup>3D</sup>BAROLO may have problems in deriving a reliable kinematic model.

We built initial artificial data-cubes with a resolution of 12'' (FWHM), a channel width of 7.5 km s<sup>-1</sup> and no noise. The pixel size is 3'', thus the beam covers an area of about 18 pixels. The galaxy models have a maximum radius of 400'', i.e. about 33 spatial resolution elements per side. This configuration could be a typical observation of a nearby galaxy with a modern interferometer, like the JVLA. We set global parameters for  $x_0$ ,  $y_0$ ,  $\phi$ ,  $V_{\text{sys}}$  and  $z_0$ , an exponential gas density profile and a constant dispersion field of 10 km s<sup>-1</sup>. The initial inclination is  $i = 60^\circ$ . We assumed rotation curves shaped as  $V_{\text{rot}}(R) = 2/\pi V_0 \arctan(R/R_0)$ , being  $V_0$  the asymptotic circular velocity and  $R_0$  the turnover radius, i.e. the transitional point between the rising and flat part of the rotation curve. We made a model with a steeply-rising plus flat rotation curve ( $V_0 = 250 \text{ km s}^{-1}$ ,  $R_0 = 20''$ ) and a model with slowly-rising solid body-like rotation curve ( $V_0 = 150 \text{ km s}^{-1}$ ,  $R_0 = 150''$ ). We progressively degraded the artificial data-cubes and we try to get back the input rotation curves using <sup>3D</sup>BAROLO.

- **Spatial resolution.** We first reduced the spatial resolution by smoothing the initial data-cubes down to 200'' (preserving the number of pixels per beam), that is 2 resolution elements per side for the model galaxies. With a large number of velocity channels and no noise, <sup>3D</sup>BAROLO is able to recover the correct rotation curve even at the lowest resolution. This could be the case of a single-dish observation as those in [Section 3.3](#). For comparison, we also derived the rotation curves running ROTCUR on the Gaussian velocity fields, fitting only the rotation velocity. [Figure 3.9](#) shows the comparison between the rotation curves derived with <sup>3D</sup>BAROLO and ROTCUR for the models at 50'', 100'' and 200'', i.e. 8, 4 and 2 resolution elements respectively. Both approaches recover an almost perfect rotation curve when the galaxy has more than 10 resolution elements per side, but, below this limit, ROTCUR increasingly underestimates the rotation velocity, especially in the inner regions of the model with flat rotation curve, whereas <sup>3D</sup>BAROLO can successfully determine it. With the 2D approach the relative errors with respect to the actual rotation curve are up to 60% in the lowest resolution and in the inner parts, whereas with the 3D approach the errors are confined to a few percent at all resolutions and over the entire disk.

- **Inclination angle.** Next, we studied the effect of the inclination on <sup>3D</sup>BAROLO's accuracy, in particular on the fit of  $V_{\text{rot}}$  and  $\sigma_{\text{gas}}$ . We let the inclination of the model

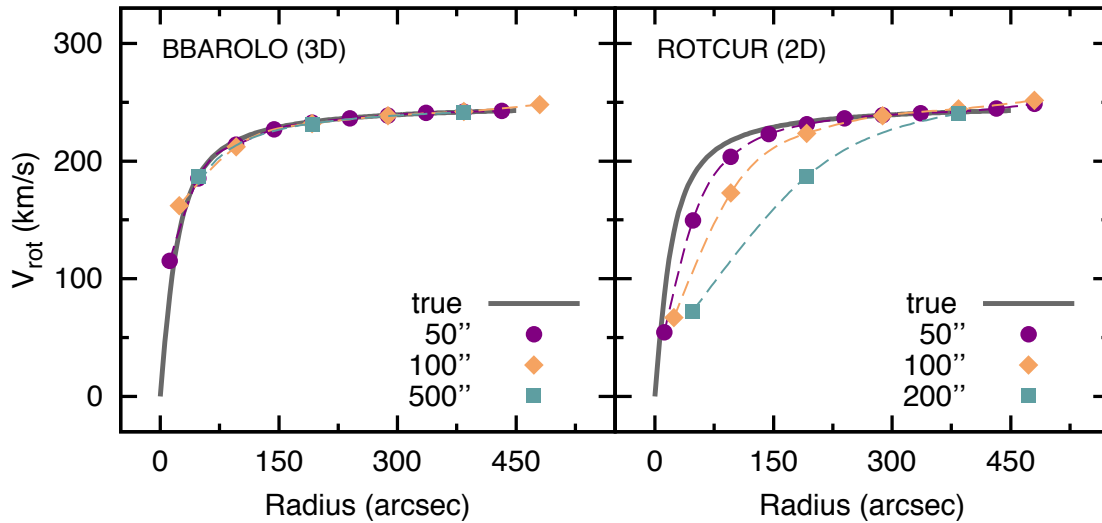


**Figure 3.9:** Effect of the spatial resolution on the derivation of rotation curves with  $3^{\text{D}}$ BAROLO (*left*) and ROTCUR (*right*). We show the rotation curves at  $50''$  (purple circles),  $100''$  (yellow diamonds) and  $200''$  (cyan squares), corresponding to 8, 4, and 2 resolution elements per side, respectively. The rotation curve of the initial model is the grey thick line. Dashed lines are spline interpolations to datapoints, outlining the shapes of the derived rotation curves.

galaxies varying from nearly face-on to nearly edge-on and fitted these models by fixing the inclination. In [Figure 3.10](#) we show the recovered rotation curves and velocity dispersions for the lowest resolution models, namely two and four resolution elements per side, and for three representative inclination angles, i.e.  $45^\circ$ ,  $60^\circ$  and  $75^\circ$ . The rotation velocity is well recovered at any inclination both in models with flat and solid-body rotation curve, although in the flat model for  $i > 75^\circ$  the inner points of the rotation curves start to be underestimated. The velocity dispersion of the inner point can be overestimated in some cases by a factor up to about 2 but with large error bars, the other points are recovered within a few  $\text{km s}^{-1}$ .

Overall, if the inclination is known,  $3^{\text{D}}$ BAROLO can derive the correct rotation curve and can disentangle between rotation and velocity dispersion at almost every inclination and even for data at very low spatial resolution where the 2D approach can not be used. When the inclination is not known, the code can fit it together with the kinematical parameters, but this requires some care. The inclination is the thorniest parameter to deal with and running  $3^{\text{D}}$ BAROLO with a completely unknown inclination is not advisable since the code can easily converge to a local minimum close to the initial inclination. The initial guess for the inclination is therefore essential for the goodness of the fit and it can be either supplied by the user (e.g. optical values) or estimated by  $3^{\text{D}}$ BAROLO. Our tests show that the algorithm for the initial guesses (see [Section 2.5](#)) returns good estimates (within a few degrees) of the global inclination in most cases regardless of the spatial resolution

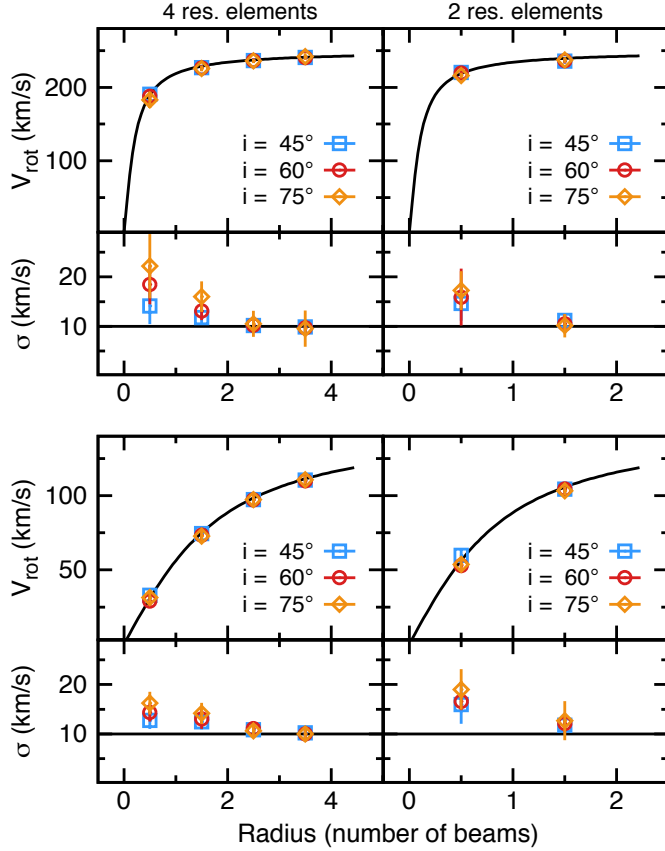


**Figure 3.10:** Rotation velocity and velocity dispersions derived with  $3^{\text{D}}\text{BAROLO}$  from models with flat (*top*) and slowly-rising (*bottom*) rotation curves. Here we show the lowest resolution models, i.e.  $100''$  (*left*) and  $200''$  (*right*), and three inclinations ( $45^\circ$ ,  $60^\circ$  and  $75^\circ$ ). Models are the black thick lines. At these resolutions, we run  $3^{\text{D}}\text{BAROLO}$  with just  $V_{\text{rot}}$  and  $\sigma_{\text{gas}}$  free.

when  $45^\circ \lesssim i \lesssim 75^\circ$ . Thus, in general for  $i \gtrsim 45^\circ$  one should always be able to obtain acceptable kinematical fits (note that above  $75^\circ$ , errors in the inclination have little impact in the rotation velocity). For  $i \lesssim 45^\circ$  rotation curves may become progressively more uncertain due to the smaller rotational component along the line of sight and the larger impact of inclination errors. This is a problem for any fitting algorithm. Finally, we note that the inclination is degenerate with the disk thickness and we expect this effect to be important especially for dwarf galaxies. In the future, we will consider to include a self-consistent treatment (assuming the hydrostatic equilibrium of the gas) for the disk thickness in  $3^{\text{D}}\text{BAROLO}$ .

- **Noise.** We also tested the effect of the noise on the derivation of rotation velocities and velocity dispersions. We focused on  $i = 60^\circ$ , used a constant surface density profile for the galaxy models and added a progressively higher Gaussian noise to the artificial data-cubes with two and four resolution elements. Relatively low S/N and less than 10 resolution elements are typical of ALMA data of high- $z$  galaxies and are expected for most data of the future HI surveys. We calculated the relative percentage errors of the fitted  $V_{\text{rot}}$  and  $\sigma_{\text{gas}}$  with respect to the true values. In [Figure 3.11](#) we show the average errors over the entire disk as a function of the average S/N. The performance of  $3^{\text{D}}\text{BAROLO}$  remains consistently high whenever the signal

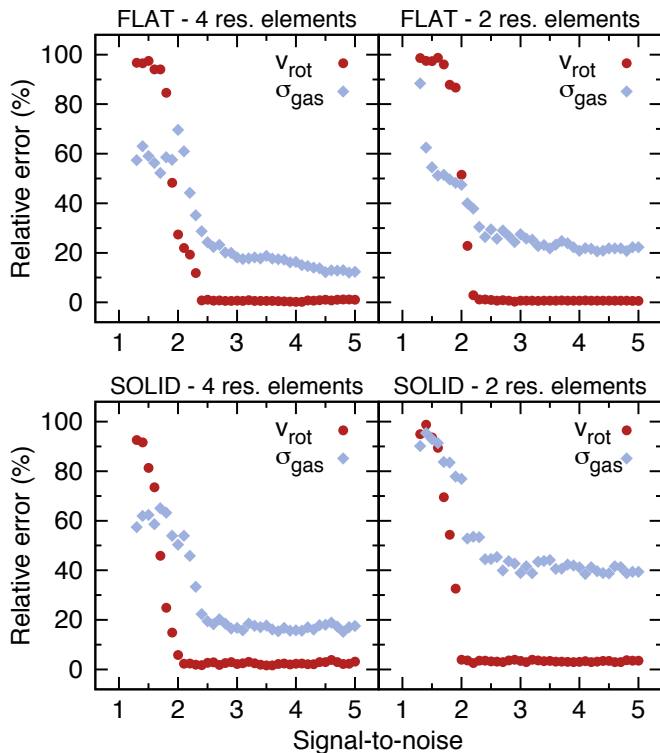


**Figure 3.11:** Relative percentage errors for the fitted  $V_{\text{rot}}$  (red circles) and  $\sigma_{\text{gas}}$  (cyan diamonds) as a function of the average S/N at fixed  $i = 60^\circ$ . We show the results for the flat (*top*) and solid-body model (*bottom*) at the lowest resolutions, i.e.  $100''$  (4 resolution elements, *left*) and  $200''$  (2 resolution elements, *right*). The code becomes unreliable below a  $\text{S/N} \lesssim 2 - 2.5$ .

to noise of the average emission in the ring is  $\text{S/N} > 2$ . Below this limit,  ${}^3\text{D}$ BAROLO may consider portions of the background as galaxy emission, leading to a wrong fit of the circular velocity and velocity dispersion, which can be either overestimated or underestimated without systematic changes in slope or shape. Further tests in the inclination range  $45^\circ < i < 75^\circ$  did not significantly change such a threshold and the trends showed in Figure 3.11. We stress that these tests were run with the default masking options and that a manual fine-tuning of the mask might lead to good results even at slightly lower signal-to-noise ratios.

- **Spectral resolution.** Finally, we reduced the spectral resolution in the noisy artificial data-cubes. Low spectral resolutions characterize, for instance, IFUs data (like KMOS or MUSE), which typically have channel widths of  $30\text{--}40 \text{ km s}^{-1}$  for each emission line, i.e. observed galaxies can span less than ten channels. Increasing the channel width dramatically lowers the number of data points that  ${}^3\text{D}$ BAROLO can use to constrain the best model. From our test emerges that the number of channels that guarantees a good fit at low S/N varies between 8 and 12, depending on the spatial resolution.

In conclusion,  ${}^3\text{D}$ BAROLO can work with observations at very low spatial/spectral resolution and low S/N and in a wide range of galaxy inclinations. These factors together influence the goodness of the model. In an extreme case of a galaxy with

just a couple of resolution elements per side, it would be advisable that the source is detected at a  $S/N \gtrsim 3$  and over a dozen channels or more.

## Gas accretion from minor mergers in local spiral galaxies<sup>†</sup>

ABSTRACT — In this Chapter, we present a study of the contribution of minor mergers to the total gas accretion onto star-forming galaxies in the local Universe. We quantify the gas accretion rate from minor mergers using HI observations of 148 nearby spiral galaxies selected from the WHISP sample. We used <sup>3D</sup>BAROLO’s source finder to iteratively analyze HI data-cubes, find dwarf gas-rich satellites around larger galaxies and estimate an upper limit to the gas accretion rate. We found that 22% of the galaxies have at least one detected dwarf companion. We made the very stringent assumption that all satellites are going to merge in the shortest possible time transferring all their gas to the main galaxies. This leads to an estimate of the maximum gas accretion rate of  $0.28 M_{\odot} \text{ yr}^{-1}$ , about five times lower than the average SFR of the sample. Given the assumptions, our accretion rate is clearly an overestimate. Our result strongly suggests that minor mergers do not play a significant role in the total gas accretion budget in local galaxies.

The evolution of galaxies is strongly affected by their capability of retaining their gas and accreting fresh material from the surrounding environment (Section 1.5). Galaxies belonging to the “blue-sequence”, which are actively forming stars and are dominated by young stellar populations, show an almost constant or a slowly declining star-formation rate throughout the Hubble time (e.g., Panter et al., 2007). Since the gas consumption time-scales are always of the order of a few Gyrs (Noeske et al., 2007; Bigiel et al., 2011), spiral galaxies need to replenish their gas at rates comparable to their star formation rates (Hopkins, McClure-Griffiths & Gaensler, 2008; Fraternali & Tomassetti, 2012). These arguments are fully applicable to the Milky Way: with a SFR of  $1\text{-}3 M_{\odot}$  slowly declining over the last  $\sim 10$  Gyrs (e.g., Aumer & Binney, 2009; Chomiuk & Povich, 2011), the Galaxy would have exhausted

---

<sup>†</sup>Based on E. M. Di Teodoro & F. Fraternali, 2014, A&A, 567, 68

its gas reservoir in a few Gyrs without replacement from outside (e.g., Chiappini, Matteucci & Gratton, 1997).

As mentioned in Section 1.5, there are essentially two sources from which disk galaxies can gain new gas: the intergalactic medium (IGM) and other gas-rich galaxies. The IGM is the place where the most of baryons are thought to still reside (e.g., Bregman, 2007). Most of this gas should be in a diffuse warm-hot phase (e.g., Shull, Smith & Danforth, 2012). Therefore the IGM represents a huge reservoir of nearly pristine gas but how this material can cool and accrete onto the disks is not well understood. Current cosmological simulations predict that gas accretion can occur in two modes (e.g., Ocvirk, Pichon & Teyssier, 2008; Kereš et al., 2009): the “hot” accretion, which dominates the growth of massive galaxies, and the “cold” accretion through filamentary streams and clouds, which prevails in lower mass structures and at high redshifts (e.g., Dekel & Birnboim, 2006). The second channel for gas accretion is given by merger events. According to the Extended Press-Schechter theory, the structures in the Universe grow by several inflowing events and have increased their mass content through a small number of major mergers, more common at high redshifts, and through an almost continuous infall of dwarf galaxies (Bond et al., 1991; Lacey & Cole, 1993). Although several theoretical (e.g., Stewart et al., 2009; Kazantzidis et al., 2009) and observational studies (e.g., Patton et al., 2000; Lotz et al., 2008; Lambas et al., 2012) have been carried out in the last years, the predictions and the estimates for the galaxy merger rate and its evolution with redshift remain uncertain and no consensus has been achieved yet (e.g., Bertone & Conselice, 2009; Hopkins et al., 2010).

In this Chapter, we use neutral hydrogen observations to investigate gas accretion from minor mergers onto star-forming galaxies in the local Universe. The advantage of using HI observations instead of the optical-UV ones is that both morphological and kinematical information are immediately available. In addition, the gas layers are more easily disturbed by tidal interactions than the stellar disk. Two studies, namely Holwerda et al. (2011) and Sancisi et al. (2008), have taken advantage of HI data and both made use of the WHISP catalogue (van der Hulst, van Albada & Sancisi, 2001). Holwerda et al. (2011) focused on the galaxy merger fraction and, employing techniques developed for optical-UV observations, found a merger fraction between 7% and 13%. Instead, Sancisi et al. (2008) attempted to quantify the contribution of minor mergers to the total gas accretion. They found that 25% of local galaxies show signs of minor interactions or have disturbed HI distribution and, assuming lifetimes for these observed features of about 1 Gyr and typical accreted HI mass of order  $10^8$ - $10^9 M_{\odot}$ , they calculated an accretion rate of about 0.1-0.2  $M_{\odot} \text{ yr}^{-1}$ . This value is about an order of magnitude lower than typical star formation rates.

In this study, we use a quantitative approach to obtain a reliable estimate of the

merger fraction and of the gas accretion rate. In [Section 4.1](#), we describe how we used <sup>3D</sup>BAROLO to identify dwarf satellites and to estimate of accretion time. In [Section 4.3](#), we show the results obtained by applying our analysis on a sub-sample of the WHISP catalogue and we discuss them in [Section 4.4](#).

## 4.1 Method

We used the source finder implemented in <sup>3D</sup>BAROLO to detect dwarf gas-rich companions around large spiral galaxies. Once the algorithm has found a candidate, it derives its physical properties, such as the HI mass, the projected distance from the main galaxy and an estimate of the accretion rate onto the central disk. Our approach can be outlined in three steps:

1. *Identifying the main galaxy.* The pixels referable to the central galaxy emission are identified and isolated through an appropriate mask.
2. *Searching for dwarf galaxies.* The data-cube is scanned for three-dimensional sources inside the field of view. Detected sources include both dwarf galaxies and HI clouds without optical counterparts.
3. *Estimating the gas accretion rate.* For each detected dwarf, a maximum accretion rate onto the disk is calculated by estimating a minimum time of collision between the satellite and the central galaxy.

In the following sections, we describe the most important steps and the main features and limitations of our method.

### 4.1.1 Searching for sources and background statistics

A crucial point of the searching algorithm is the determination of the flux threshold. The typical data-cube of the WHISP survey is dominated by a large number of noise pixels and a relatively small number of bright pixels that belong to the sources. In such a situation, it is preferable to calculate the noise over the whole data-cube and use robust statistic estimators, i.e. the median  $m$  as noise middle and the MADFM as noise spread. We assume that the noise is Gaussian and the threshold is determined as  $\tau = m + n \text{ MADFM}/0.6745$  (see [Section 2.5.1](#)). We however checked that the noise middle and spread calculated using the whole data-cubes are the same as those obtained using boxes where there is no emission; the differences do not exceed 5%.

We used the searching algorithm implemented in <sup>3D</sup>BAROLO in two different steps: the identification of the main galaxy and the detection of satellites. The former consists in isolating all those regions ascribable to the main galaxy emission. <sup>3D</sup>BAROLO performs a search in the data-cube using the one-dimensional technique

(see [Section 2.5.1](#)) and selects as the main galaxy the object that covers the largest number of pixels. This approach is not computationally expensive, and it is reliable when the code is analysing an heterogeneous group of galaxies, but it does not allow the code to identify systems in advanced phase of merging, i.e., when a companion is physically connected in space and velocity with the main galaxy. Concerning the detection of satellites, we used the Lutz algorithm (see [Section 2.5.1](#)), which guarantees a better reliability and minimizes the number of spurious detections. We impose a neighborhood criterion grounded on the spatial and spectral resolution of the observations: each detected pixel is merged with other detected pixels lying within a spatial beam and within two velocity channels, which is the typical instrumental broadening (FWHM) for HI observations when Hanning smoothing has been applied. Finally, we reject all those detections that are smaller than the beam area of the observations and less extended in velocity than the spectral broadening. We stress that a three-dimensional source finding algorithm, unlike the two-dimensional methods, can isolate sources with different kinematics even if they are totally or partially overlapped in the plane of the sky. Indeed, if two sources have radial velocities that differ more than the typical velocity resolution ( $\sim 10\text{-}15 \text{ km s}^{-1}$ ), they are always detected as separate sources, no matter whether they overlap or not on the sky.

#### 4.1.2 Accretion and star formation rate estimates

The main purpose of this study is to estimate the maximum gas accretion rate coming from minor mergers. In the following we describe our assumptions.

Firstly, we assume that all dwarf galaxies will collide in the future with the main galaxies and that their gas will be entirely and instantaneously accreted. Secondly, we assume that the collision will occur in the shortest possible time. In order to calculate this time, we make the satellites moving in parabolic trajectories leading to impact the outer regions of the main galaxies. The orbit is defined in the three-dimensional space by fixing the focus of the parabola at the centre of the main galaxy, imposing the passage through the satellite and fixing the position of the orbital peri-centre at a distance equal to the maximum radius of the central galaxy ([Figure 4.1](#)). For a generic conic orbit, the time-scale of collision can be obtained by using the equation of the true anomaly  $\nu$  of celestial mechanics:

$$\int_0^\nu \frac{d\nu'}{(1 - e \cos \nu')^2} = \sqrt{\frac{\mu}{p^3}} (t - T_0) \quad (4.1)$$

where  $e$  is the eccentricity of the orbit,  $T_0$  is the time of the peri-centre passage,  $p$  is the semi-latus rectum of the conic section and  $\mu = G(M_{\text{main}} + M_{\text{sat}}) \sim GM_{\text{main}}$  is the total dynamical mass of the system galaxy plus satellite multiplied by the

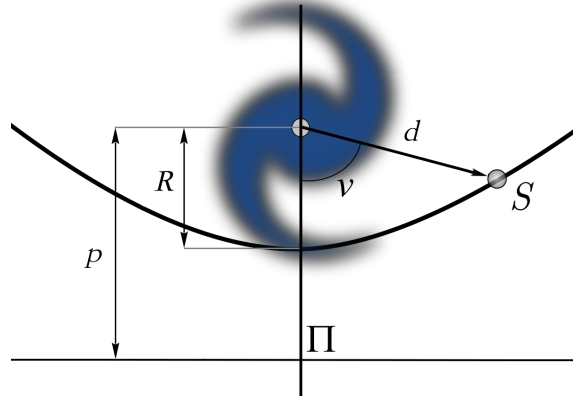


**Figure 4.1:** Schematic view of the parabolic orbit approximation. The blue spiral is the main galaxy,  $S$  is the satellite with projected distance  $d$  and true anomaly  $\nu$ . The distance  $p$  between the center of the spiral galaxy and the directrix  $\Pi$  of the parabola is twice the outer radius  $R$  of the main galaxy.

gravitational constant  $G$ . The dynamical mass of the central galaxy  $M_{\text{main}}(R_{\text{max}}) = G^{-1}V_{\text{rot}}(R_{\text{max}})^2R_{\text{max}}$  is calculated within the maximum radius  $R_{\text{max}}$  of the source, estimated by the searching algorithm. The rotation velocity  $V_{\text{rot}}$  is obtained from the velocity widths of the HI global profiles at the 20% of the peak flux corrected for the inclination taken from the HyperLEDA catalogue. Solving the integral (Equation 4.1) for parabolic orbits ( $e = 1$ ) one obtains the following formula which describes the variation of the true anomaly  $\nu$  as a function of time:

$$\tan \frac{\nu}{2} + \frac{1}{3} \tan^3 \frac{\nu}{2} = \sqrt{\frac{\mu}{p^3}} (t - T_0) \quad (4.2)$$

where the semi-latus rectum for parabolic orbit is  $p = 2R$ , being  $R$  the distance between the focus and the vertex of the parabola (Figure 4.1).

Using Equation 4.2, we can estimate the time of the peri-centre passage  $T_0$  by calculating  $\nu$  through a de-projection of the projected anomaly  $\nu_p$  of the dwarf galaxy measured in the plane of the sky. The accretion rate of cold gas onto a certain galaxy is then obtained by dividing the HI mass of each dwarf by its time of peri-centre passage:

$$\dot{M}_{\text{HI}} = \sum_{i=0}^n M_{\text{HI},i}/T_{0,i} \quad (4.3)$$

where the sum is taken over all the detected companion galaxies. The HI mass  $M_{\text{HI}}$  is calculated from the flux density using the following relation (Roberts, 1975):

$$M_{\text{HI}} = 2.356 \times 10^5 D^2 \int S(\nu) d\nu \quad (4.4)$$

where  $\int S(v) dv$  is the integral across the line of the flux density corrected for the primary beam attenuation and expressed in  $\text{Jy km s}^{-1}$  and  $D$  is the distance in Mpc. Equation 4.4 is valid under the assumption that the gas is optically thin, which is generally a good approximation for neutral hydrogen, especially in dwarf galaxies, thus no correction for HI self-absorption was applied. The distances were preferably taken from the Extragalactic Distance Database (EDD, Tully et al., 2013), available for a number of galaxies with  $V_{\text{sys}}$  up to  $10000 \text{ km s}^{-1}$  and mostly obtained from Cepheids, TRGB, SNIa or Cosmicflows-2 project (Tully et al., 2009). Otherwise, we used the NASA/IPAC Extragalactic Database (NED). For seven main galaxies with no available better estimates, we used the Hubble flow  $D = V_{\text{sys}}/H_0$  with  $H_0 = 70 \text{ km s}^{-1} \text{ Mpc}^{-1}$  and the systemic velocity  $V_{\text{sys}}$  corrected for Virgo-centric inflow using the values given by the HyperLEDA catalogue. For dwarf satellites, we used distances from EDD and NED or, when not available, we assumed the distance of the main galaxy.

We compare the total gas accretion (Equation 4.3) to the gas depletion due to the star formation process in the disks. The SFR of the central galaxies was calculated from the far-infrared luminosities (Kennicutt, 1998):

$$\text{SFR} = \frac{L_{\text{FIR}}}{2.2 \times 10^{43}} \text{ M}_{\odot} \text{ yr}^{-1} \quad (4.5)$$

with the  $L_{\text{FIR}}$  in  $\text{erg s}^{-1}$  obtained from the far-infrared flux FIR defined after Helou, Soifer & Rowan-Robinson (1985) as:

$$\text{FIR} = 1.26 \times 10^{-11} (2.58 f_{60\mu} + f_{100\mu}) \text{ erg s}^{-1} \text{ cm}^{-2} \quad (4.6)$$

where  $f_{60\mu}$  and  $f_{100\mu}$  are the fluxes at 60 and 100 micron expressed in Jansky. In this work we used the IRAS fluxes taken from NED and HyperLEDA. All main galaxies in our sample are detected both at  $60\mu$  and  $100\mu$ . See Table 4.7 for their main physical properties.

### 4.1.3 Major/minor mergers and mass estimates

We split major and minor mergers depending on the baryonic mass ratio: pair of galaxies with  $M_{\text{bar,sat}}/M_{\text{bar,main}} \leq 0.20$  are classified as minor mergers, otherwise as major. We preferably estimate the baryonic mass as:

$$M_{\text{bar}} = M_{*} + 1.4M_{\text{HI}} \quad (4.7)$$

where the factor 1.4 take into account the helium gas fraction. We neglected the contribution of molecular gas (Young & Scoville, 1991). The HI mass  $M_{\text{HI}}$  is directly estimated from the data through Equation 4.4. A rough estimate of the stellar mass

$M_*$  is obtained by using the total  $K_s$ -band magnitude, corrected for extinction, taken from the 2MASS Redshift Survey (2MRS, Huchra et al., 2012) and adopting the following formula (e.g. Longhetti & Saracco, 2009):

$$\log_{10}(M_*) = \log_{10}(M/L_K) - 0.4[K + 5 - 5 \log_{10}(D_{[\text{pc}]}) - 3.28] \quad (4.8)$$

where  $M/L_K$  is the stellar mass-to-light ratio (in solar units) in the K-band and 3.28 is the absolute K-band magnitude of the Sun in the Vega system (Binney & Merrifield, 1998). We assumed a constant value of mass-to-light ratio  $M/L_K = 0.6 M_\odot/L_{\odot,K}$ , compatible with stellar population models (e.g. Portinari, Sommer-Larsen & Tantalo, 2004) with a Kroupa IMF (Kroupa, 2002).

When 2MRS magnitudes were not available, namely for most dwarf satellites and a few main galaxies, we directly derived  $M_{\text{bar}}$  from the Baryonic Tully-Fisher Relation (BTFR):

$$\log_{10}(M_{\text{bar}}) = a \log_{10}(V_{\text{flat}}) + b \quad (4.9)$$

with  $a = 3.82 \pm 0.22$  and  $b = 2.01 \pm 0.41$  (McGaugh, 2012). The  $V_{\text{flat}}$  was assumed as half of the inclination-corrected velocity widths  $W_{20}$  of the HI global profiles at the 20% of the peak flux. Since inclination angles are not known for most dwarf satellites, we adopted an average inclination of 60 degrees for these galaxies.

## 4.2 The HI data sample

The Westerbork HI survey of Irregular and Spiral galaxies Project (WHISP, van der Hulst, van Albada & Sancisi, 2001) is a survey of the neutral hydrogen content in galaxies selected from the Uppsala General Catalogue (UGC, Nilson, 1973) and observed with the Westerbork Synthesis Radio Telescope (WSRT). WHISP is to date the largest publicly available catalogue of HI nearby galaxies observed with an interferometer and it includes galaxies at  $\delta > 20^\circ$  (B1950) with major axis apparent size  $> 1.2'$  (B band) and HI flux densities  $F_{\text{HI}} > 100$  mJy. Objects satisfying these selection criteria have generally systemic velocities less than  $6000 \text{ km s}^{-1}$ , i.e., distances lower than 85 Mpc using the Hubble flow with  $H_0 = 70 \text{ km s}^{-1} \text{ Mpc}^{-1}$ . The galaxies were chosen to be reasonably distributed over all Hubble types, even if later-type galaxies are favoured by the observational criteria. The highest spatial resolution for the WHISP data is  $12'' \times 12''/\sin(\delta)$ , the typical channel separation is of the order of  $5 \text{ km s}^{-1}$ . In this work, we used both HI data-cubes spatially smoothed to  $30'' \times 30''$  and  $60'' \times 60''$ . The original sample comprises 256 data-cubes containing about 370 galaxies.<sup>1</sup>

<sup>1</sup> The datacubes, the column density maps and the velocity fields of the WHISP galaxies, at  $12''$ ,  $30''$  and  $60''$  of resolution, are publicly available for the ‘‘Westerbork on the Web’’ project at

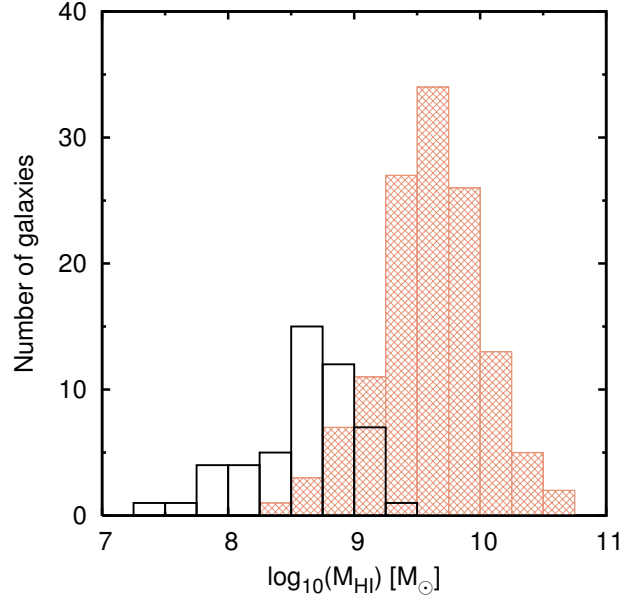


**Figure 4.2:** HI Mass distribution of the detected galaxies in the WHISP sample. Orange shadowed boxes show the spiral galaxies selected as  $V_{\text{flat}} > 100 \text{ km s}^{-1}$ , black boxes show their dwarf satellites.

Since our goal is to study dwarf satellites around large star-forming galaxies, we selected a sub-sample of spiral galaxies by keeping only those data-cubes containing at least one galaxy with rotation velocity  $V_{\text{flat}} = W_{20}/(2 \sin i) > 100 \text{ km s}^{-1}$ . The selection was performed through a cross-correlation between the  $W_{20}$  estimated directly from the data-cubes and the  $W_{20}$  calculated using the Tully-Fisher relation from Sakai et al. (2000):

$$M_B = -(7.97 \pm 0.72)(\log w_{20} - 2.5) - (19.80 \pm 0.11) \quad (4.10)$$

where  $M_B$  is the  $B$ -band absolute magnitude (corrected for galactic extinction and  $k$ -correction), taken from HyperLEDA. We kept only galaxies for which both methods returned  $V_{\text{flat}} > 100 \text{ km s}^{-1}$ . This cross-correlation is needed to avoid spurious selections related to some unreliable inclination angles in the HyperLEDA catalogue. Our final sample has 148 data-cubes. Spiral galaxies therein have usually neutral hydrogen masses between  $10^9 M_{\odot}$  and few  $10^{10} M_{\odot}$  (Figure 4.2). The global properties of the main galaxies are listed in Table 4.7.

### 4.3 Results

We ran our code both on data-cubes smoothed to 30'' and 60''. The results obtained with these two data sets are fully comparable. We fixed a sigma-clipping threshold for the source finder equal to 4 and a secondary threshold for growing objects at the edges of 2.5 (see [Section 2.5.1](#)). After extensive experiments, these values appeared the best compromise between reaching low sensitivities and avoiding spurious detections.

We found that, among 148 data-cubes, 101 ( $\sim 68.2\%$ ) had no detectable companions, whereas 47 ( $\sim 31.8\%$ ) contained multiple systems. Among these 47 data-cubes, 15 ( $\sim 10.1\%$  of the total,  $\sim 31.9\%$  of multiple systems) contained only galaxies with similar masses ( $M_{\text{bar,sat}}/M_{\text{bar,main}} > 0.20$ ). Six data-cubes ( $\sim 4.1\%$  of the total,  $\sim 12.8\%$  of multiple systems) show both major and minor companions and 26 data-cubes ( $\sim 17.6\%$  of the total,  $\sim 55.3\%$  of multiple systems) show only dwarf companions. Overall, among 148 analysed data-cubes, 21 ( $\sim 14.2\%$ ), show companions which could be possible candidates for a future major merging, while 32 data-cubes ( $\sim 21.6\%$ ) show potential candidates for minor mergers. Some examples of spiral galaxies with minor satellites are shown in [Figure 4.3](#).

We focused on potential minor mergers and all data-cubes with only major companions were excluded from the further analysis. We discuss how this assumption affects our results in [Section 4.4.1](#). For the six data-cubes with both types of companions, we assumed as the main galaxy the one with the largest HI mass and we ignored the other spiral galaxies. The total number of dwarf gas-rich satellites detected is 50 ([Table 4.6](#)). Forty-six dwarf galaxies have a clear optical counterpart in the Sloan Digital Sky Survey (SDSS) or in the Digitized Sky Survey (DSS) images. Four detections, marked with an asterisk in [Table 4.6](#), are not univocally identifiable and they could be either very faint dwarf galaxies or HI clouds. Most satellites are already catalogued in galaxy archives. Ten galaxies, marked with a dagger in [Table 4.6](#), seem not to be catalogued. The HI masses of the detected dwarf galaxies vary between about  $10^7 M_{\odot}$  and few  $10^9 M_{\odot}$ . The HI mass distribution of the main galaxies and their minor satellites is shown in [Figure 4.2](#). The mass function for spiral galaxies is peaked at  $\log M_{\text{HI}[M_{\odot}]} \sim 9.5$ , consistently with studies on wider HI samples (e.g., Zwaan et al., 2005). Most dwarf companions have masses of a few  $10^8 M_{\odot}$  and their mass distribution has a cut-off above  $5 \times 10^9 M_{\odot}$ . This is partially due to our selection criteria. However, it is interesting to note that this distribution is fairly comparable with that of HI-rich dwarf galaxies in the Local Group and in Local Group analogues (e.g., Grcevich & Putman, 2009; Pisano et al., 2011). In [Figure 4.4](#) we show the HI masses of the detected dwarf galaxies as a function of the distance from the Milky Way. The red triangles represent the minimum detectable mass for each data-cube, calculated using equation ([Equation 4.4](#)) on a

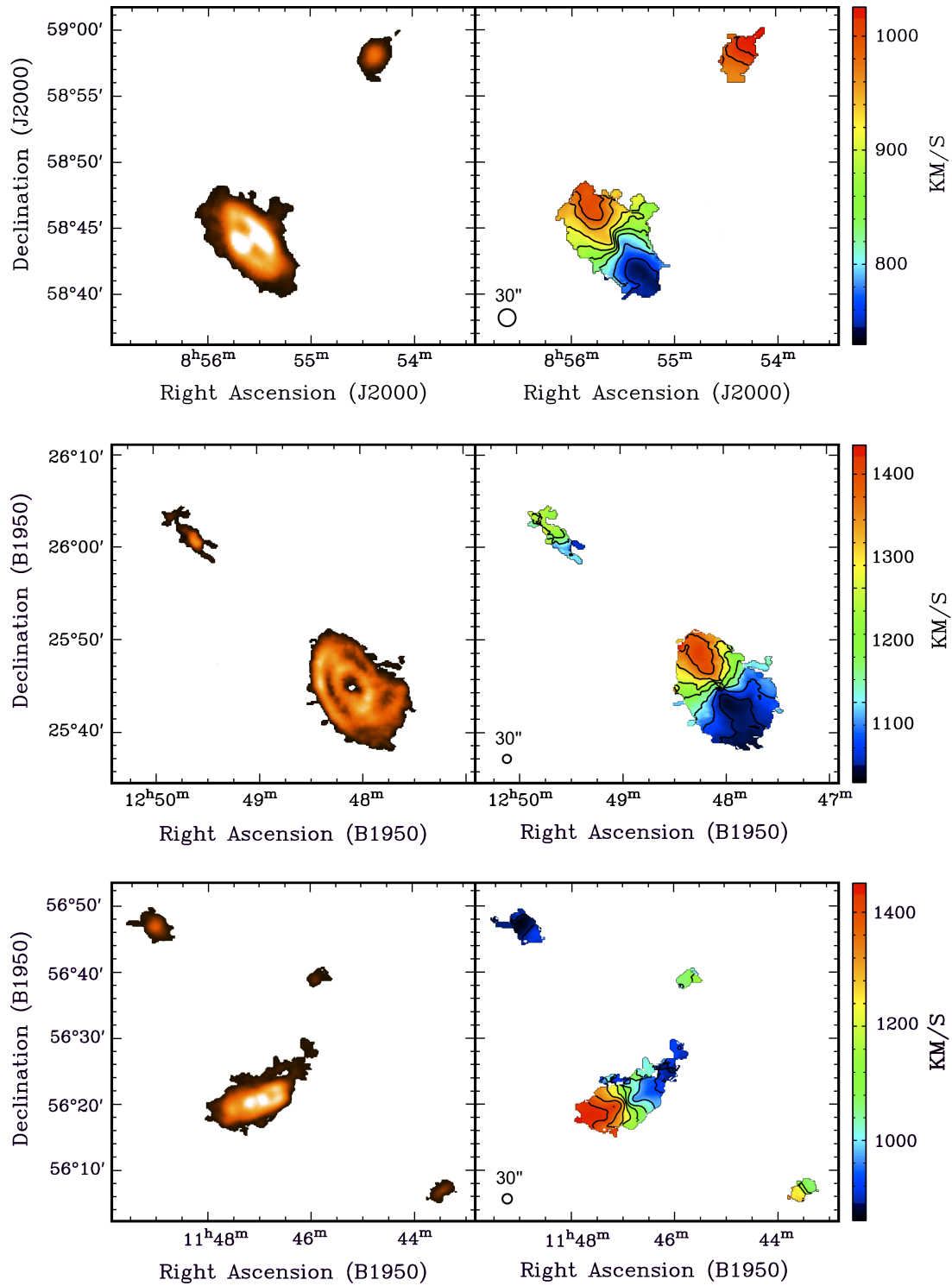


**Figure 4.3:** Three examples of multiple systems in the WHISP sample. From the *top* to the *bottom*, UGC 4666, UGC 7989, UGC 6787 and their dwarf companions. *Left panels:* Hi column-density maps (0th moment). *Right panels:* The velocity fields (1st moment) obtained from 30'' smoothed data-cubes.

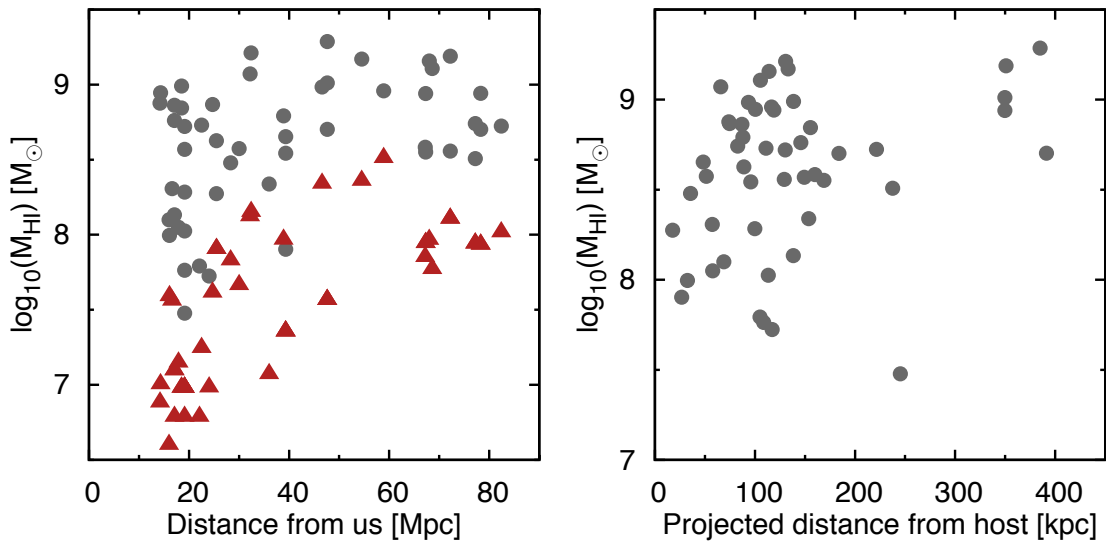


**Figure 4.4:** *Left panel:* the gray dots show the HI masses of detected companions as a function of distance from us, red triangles are the lowest detectable mass in the corresponding data-cubes. *Right panel:* HI mass of detected satellites as a function of the distance from the main galaxies projected onto the plane of the sky.

three-dimensional region with the size of a spatial beam times the velocity resolution (two channels) and a flux of  $4\sigma_{\text{noise}}$  of the cube. This is the minimum mass that an object must have to be accepted by the source-finding algorithm. Note the bias effect on the detectable mass due to the distance (see discussion in [Section 4.4.1](#)).

The projected distances of the dwarf satellites from the main galaxies usually range from some dozen to a few hundred kiloparsecs and typical time-scales for collisions, estimated through the parabolic orbit approximation, are between  $\sim 100$  Myr and 2 Gyr. The number of dwarfs within 100 kpc from the main galaxies and between 100 and 200 kpc is almost the same. The *right panel* of [Figure 4.4](#) shows the projected distance as a function of the dwarf HI masses. Within 200 kpc, dwarf galaxies are quite uniformly distributed over the HI masses. There is a weak tendency for companions to be more massive at larger distances. However, there is an observational bias that can affect this plot. It is a combination of two effects: the linear field-of-view of the observations increases with distance, while the minimum detectable mass ([Figure 4.4, left panel](#)) and the linear resolution decrease. Thus we may detect preferentially companions with lower masses closer to the main galaxies and vice-versa. Moreover, there is also a selection effect due to the primary beam attenuation, i.e. at large angular distances, only massive systems are detected because of the lower sensitivity of the instrument. These effects make it difficult to compare our findings with studies of dwarfs galaxies in the Local Group or other nearby galaxy group.

The systemic velocity of dwarf galaxies is calculated as the average midpoint

between the velocities at the 20% and 50% of the peak flux of their global HI profiles. The  $\Delta V_{\text{sys}} = \| V_{\text{sys,main}} - V_{\text{sys,sat}} \|$  ranges between a few tens to a few hundreds  $\text{km s}^{-1}$ . Satellites do not have systemic velocities that differ more than  $300 \text{ km s}^{-1}$  from those of the main galaxies. The velocity widths  $W_{20}$  of dwarf galaxies, taken at the 20% of the peak flux, are usually lower than  $200 \text{ km s}^{-1}$ , even if corrected for a mean inclination of 60 degrees, except for three galaxies. Overall, most of the satellites have  $W_{20} < 100 \text{ km s}^{-1}$ .

For each data-cube with identified dwarf companions, we calculated the maximum possible accretion rate of cold hydrogen gas  $\dot{M}_{\text{HI}}$  onto the main galaxy, the star formation rate  $\dot{M}_{\text{SF}}$  of the main galaxy and the ratio  $\dot{M}_{\text{HI}}/\dot{M}_{\text{SF}}$ . For all galaxies, with or without identified companions, a potentially hidden accretion from dwarfs below the detectability limit was estimated. The hidden accretion rate was calculated by dividing the above-mentioned the minimum detectable mass by the average collision time over the sample, i.e 1.1 Gyr. Integrating the HI mass function ( $\phi_*[\text{Mpc}^{-3} \text{dex}^{-1} h_{70}^3] = 4.8 \pm 0.3 \times 10^3$ ,  $\log(M_*/M_\odot) + 2 \log h_{70} = 9.96 \pm 0.02$  and  $\alpha = -1.33 \pm 0.02$ , (Martin et al., 2010)) below the detection limit and within the volume of each data-cube always gives HI masses lower than minimum detectable mass. Thus, with our choice we are maximizing the mass of the undetected galaxies.

We found a mean upper limit for the accretion in galaxies with identified minor companions of  $0.86 \text{ M}_\odot \text{ yr}^{-1}$ , with a mean ratio  $\langle \dot{M}_{\text{HI}}/\dot{M}_{\text{SF}} \rangle \sim 0.67$ . A more meaningful estimate is however the mean upper limit to the accretion over the whole sample, that turns out to be  $\dot{M}_{\text{HI}} = 0.28 \text{ M}_\odot \text{ yr}^{-1}$  against the average star formation rate of  $1.29 \text{ M}_\odot \text{ yr}^{-1}$ , with a mean ratio  $\langle \dot{M}_{\text{HI}}/\dot{M}_{\text{SF}} \rangle \sim 0.22$ . The median of  $\dot{M}_{\text{HI}}/\dot{M}_{\text{SF}}$  is instead 0.07. Thus, the ratio of the gas needed for star formation to the maximum gas accretion provided by minor mergers is between 5 and 14. Considering a fraction of gas recycle from stellar feedback of 30% (e.g. Naab & Ostriker, 2006; Leitner & Kravtsov, 2011) leads to a ratio between 3 and 10.

The above results show that the number of dwarf galaxies in the local Universe is on the average too low to guarantee the continuous gas replenishment needed by star formation. In Figure 4.5 we show a plot of  $\dot{M}_{\text{HI}}$  versus  $\dot{M}_{\text{SF}}$  for each galaxy individually. If the gas accretion were large enough to sustain the star formation of the main galaxies, these data points would have fully populated the blue-shadowed region in the upper-left corner, whereas the vast majority lie well below the blue straight-line indicating a ratio  $\dot{M}_{\text{HI}}/\dot{M}_{\text{SF}} = 1$ . The result does not change if we consider a fraction of 30% of gas returned to the ISM by stellar evolution processes (cyan dashed line). We conclude that minor mergers can not bring enough gas to the disks and sustain star formation. Once again, our values of gas accretion rates are very strong upper limits, because of our very stringent assumptions, and the real accretion rates could realistically be one order of magnitude lower than our estimate. To reiterate this point, we note that our assumptions would imply that

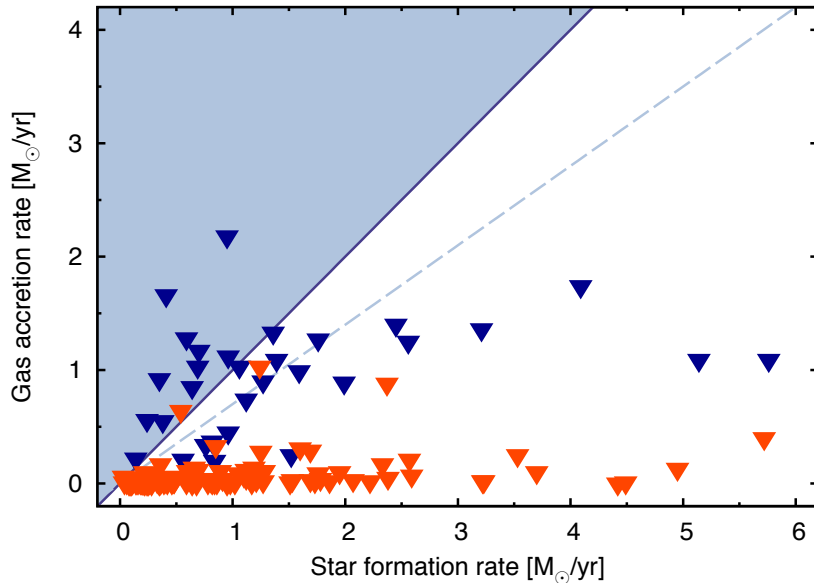


**Figure 4.5:** Upper limits to the cold gas accretion rates from satellites vs star formation rates in spiral galaxies in the WHISP sample. The inverted dark blue triangles are upper limits to the gas accretion rate for galaxies with detected satellites (including both visible and hidden accretion), the inverted orange triangles are the hidden accretion upper limits for galaxies without companions, estimated as discussed in the text. The star formation rates are calculated from the far-infrared fluxes. The blue-shadowed region represents a complete feeding of SF through minor mergers. The full blue line is  $\dot{M}_{\text{HI}} = \dot{M}_{\text{SF}}$ , the cyan dashed line is  $\dot{M}_{\text{HI}} = \dot{M}_{\text{SF}}(1 - \mathcal{R})$ , where  $\mathcal{R} = 0.3$  is the gas return fraction.

all dwarf galaxies disappear in the next 2 Gigayears. We stress that our SFRs are likely lower limits as they are calculated using only FIR fluxes. This bias goes in the direction of strengthening our findings.

We repeated the analysis of the WHISP data-cubes using a sigma-clipping threshold in <sup>3D</sup>BAROLO for the source detection of  $3\sigma$  and  $5\sigma$  (instead of  $4\sigma$ ). Reducing the detection threshold leads the code to identify many more dwarf companions: more than 100 minor satellites are detected at the lower level, but most of these sources are clearly false detections and the results obtained would be very likely unreliable. Instead, increasing the detection threshold to  $5\sigma$  leads to results very similar to those described above as just two of the dwarf companions found at  $4\sigma$  are missed by the rejection criteria, namely the satellites of UGC 7506 and UGC 9858. These companions are actually good detections, as quoted in the literature (Noordermeer et al., 2005), but at a  $5\sigma$  level they are discarded by the one-beam covering requirement. The mean values of the accretion rate at  $5\sigma$  are also in agreement with those found at  $4\sigma$ .

## 4.4 Discussion

The application of our code to the WHISP catalogue led to a firm upper limit for the accretion of cold gas from minor mergers in the local Universe of  $0.28 \text{ M}_{\odot} \text{ yr}^{-1}$ . The total multiple system fraction for the WHISP sample is  $\sim 32\%$ , in particular  $\sim 22\%$  of galaxies are accompanied by minor companions ( $M_{\text{sat}} < M_{\text{main}}$ ) and  $\sim 14\%$  are major systems. Here we discuss the main uncertainties of our results and their relevance.

### 4.4.1 Uncertainties

Our estimate does not take into account the molecular fraction. The amount of molecular gas in dwarf galaxies is highly unconstrained as they are often undetected in CO emission lines (e.g., Taylor, Kobulnicky & Skillman, 1998). They also usually have low metallicities, making the conversion between CO and  $\text{H}_2$  even more uncertain (e.g., Boselli, Lequeux & Gavazzi, 2002). However, any realistic correction for molecular gas should not increase our accretion rate by more than a factor two.

WHISP is a source-targeted survey and it can not be obviously considered as a complete sample. The selection criterion, grounded on the apparent size of the observed galaxies, produces a catalogue that favours progressively larger and more massive galaxies moving to greater distances from the Milky Way. This effect can be appreciated in Figure 4.4 (upper envelop) although it appears to be not too severe. The growth with the distance of the minimum detectable mass furthermore makes it impossible to detect low mass satellites at large distances. In order to test the importance of these biases, we have considered only those data-cubes with a minimum detectable mass  $M_{\text{det}} \leq 10^8 \text{ M}_{\odot}$ . In this way, we can obtain a sub-sample of galaxies where satellites are quite uniformly distributed over the mass and the distance ranges (*left panel* of Figure 4.4). The maximum accretion rate obtained in this case is  $0.21 \text{ M}_{\odot} \text{ yr}^{-1}$ . Reducing the threshold to data-cubes with  $\log M_{\text{det}} \leq 5 \times 10^7 \text{ M}_{\odot}$  leads to a maximum accretion rate of  $0.18 \text{ M}_{\odot} \text{ yr}^{-1}$ . These values indicate that our accretion rate estimates is not strongly affected by the incompleteness of the sample of the dwarf galaxies.

Another bias effect is related to the linear field of view, which is greater at larger distances. In the farthest systems, the field of view allows us to observe satellites with projected distances of some hundreds kpc from the main galaxies, whereas we can not go beyond one hundred kpc in the closest systems. The primary beam attenuation of the WSRT is significantly large ( $\sim 80\%$  of the flux is missed) beyond  $25'$  from the pointing center, corresponding to  $\sim 70 \text{ kpc}$  at about  $10 \text{ Mpc}$ . This indicates that we should be able to detect fairly separated satellites also in the nearest systems. The most distant satellites have larger collision time-scales and their contribution to the global accretion is expected to be smaller. In our sample,

considering only satellites within 100 kpc from the main galaxies gives an accretion rate of  $0.38 \text{ M}_{\odot} \text{ yr}^{-1}$ ,  $0.27 \text{ M}_{\odot} \text{ yr}^{-1}$  between 100 and 200 kpc and  $0.21 \text{ M}_{\odot} \text{ yr}^{-1}$  beyond 200 kpc (the global value being  $0.86 \text{ M}_{\odot} \text{ yr}^{-1}$ ). These results show that the contribution of very distant satellites is progressively less important, thus the limited field of view of the closest systems should not significantly affect our accretion rate estimate.

In the literature, mergers are usually classified on the basis of their dynamical mass ratio: pair of galaxies with  $M_{\text{sat}}/M_{\text{main}} \lesssim 0.2 - 0.3$  are considered minor mergers, otherwise major mergers. Unfortunately, we can not trivially estimate the dynamical masses of satellite galaxies from the HI data. Thus, in this work, we divided satellites depending on the ratio of their baryonic mass to the main galaxy baryonic mass. Satellites with baryonic content lower than 20% of the main galaxies ( $M_{\text{bar,sat}}/M_{\text{bar,main}} \leq 0.20$ ) are classified as minor companions. This is an arbitrary but conservative choice, since most detected satellites have mass ratio  $\ll 0.05$ . It is however interesting to quantify the accretion rate using different baryonic mass ratios. In our sample, the maximum accretion rate ranges between  $0.20 \text{ M}_{\odot} \text{ yr}^{-1}$  for  $M_{\text{bar,s}}/M_{\text{bar,g}} \leq 0.1$  and  $0.56 \text{ M}_{\odot} \text{ yr}^{-1}$  for  $M_{\text{bar,sat}}/M_{\text{bar,main}} \leq 0.5$ . If we consider the whole galaxy pairs as potential mergers and we calculate the accretion rate by accreting the less massive ones onto the most massive ones, we obtain the value of  $1.22 \text{ M}_{\odot} \text{ yr}^{-1}$ . Even such an excessive overestimate turns out to be of the same order of the mean SFR. We conclude that mergers in the local Universe can not sustain the star formation in spiral galaxies.

As a final consistency check, we verified our estimate by analysing the HI data-cubes from the Westerbork Hydrogen Accretion in LOcal GALaxieS (HALOGAS) survey (Heald et al., 2011). This survey comprises very deep observations of 24 local spiral galaxies, observed at a sensitivity capable of detecting HI sources of a few times  $10^5 \text{ M}_{\odot}$ . This sample is small, but statistically complete as explained in Heald et al. (2011). We excluded NGC 4631, a strongly interacting spiral galaxy, because of the complexity of its gas distribution. We performed our analysis on the remaining 23 galaxies by using a  $3.5\sigma$  flux threshold, we found that 10 of them have at least one detectable companion or HI clouds (Jütte et al., in preparation) and we estimated a maximum accretion rate onto the main galaxies of  $0.19 \text{ M}_{\odot} \text{ yr}^{-1}$ , a value fully compatible with the one found for the WHISP sample.

#### 4.4.2 Comparison to other estimates

The accretion of cold gas from minor mergers in the local Universe has been estimated by Sancisi et al. (2008), visually inspecting and comparing total maps, velocity fields and position-velocity diagrams for the WHISP galaxies. They found a minor merger fraction of about 25%. Unlike our approach, they considered only those systems that show clear signs of tidal interactions, such as tails, bridges,

disturbed HI morphologies and/or kinematics. Assuming typical HI masses of the dwarfs of the order  $10^{8-9} M_{\odot}$  and a lifetime for the observed features of about 1 Gyr, Sancisi et al. inferred a mean accretion rate of HI gas around  $0.1 - 0.2 M_{\odot} \text{ yr}^{-1}$  and they stressed that such a value is likely a lower limit. It is worth noting that most systems we considered as potential future minor mergers were not recognized that way by Sancisi et al. and, on the contrary, many interactions they identified were not found by our code. The reason is simple: our code looks for “separated” objects and it handles all dwarf companions as candidates for minor mergers, also those showing no signs of ongoing interaction. In other words, we look at the population of dwarfs in the environment of a spiral galaxy that could become a minor merger in the next future. Our code identifies companions until the two galaxies start “touching” each other and we estimate the accretion rate using the time-scale for collision as accretion time. Instead, Sancisi et al. (2008) find a later stage of merging, i.e., when galaxies are strongly interacting and the gas is visibly disturbed in the morphology and/or in the kinematics. Consequently, they calculate the accretion rate using as time-scale the dynamical time that it should take for these features to disappear as the gas redistributes uniformly in the disk. In our work the accretion process ends when galaxies touch each other, whereas for Sancisi et al. (2008) that is the starting point. However, since the population of dwarf galaxies has likely remained similar in the last Gyr or so, the two accretion rates should be comparable. Interestingly, our upper limit of  $\dot{M}_{\text{HI}} < 0.28 M_{\odot} \text{ yr}^{-1}$  is not in contradiction with the average accretion rate estimated by Sancisi et al. (2008).

#### 4.4.3 Merger fraction

Most of published studies on the local merging systems have been made using images from optical-UV galaxy surveys (e.g., Patton et al., 2000; Lambas et al., 2012; Robotham et al., 2012) such as the Second Redshift Survey of Southern Sky (SRSS2), the Sloan Digital Sky Survey (SDSS) and the recent Galaxy And Mass Assembly (GAMA) survey, whereas just a couple of studies have been carried on using HI data (Sancisi et al., 2008; Holwerda et al., 2011). These studies have mainly investigated the fraction and the rate (fraction of mergers per comoving volume and time units) of galaxies showing signs of interactions and their evolution with time.

To date, two main approaches have been used to estimate the galaxy merger fraction and both make use of high resolution imaging. The pair method consists in counting the galaxies spatially separated from each other by less than a few tens of kpc and with spectroscopic radial velocities that do not differ by more than a few hundreds of  $\text{km s}^{-1}$  (e.g., Le Fèvre et al., 2000; Lin et al., 2008). Using this kind of approach it is possible to estimate a “progenitor” galaxy merger fraction. The second approach identifies mergers by quantifying morphological signatures that can be related to past or ongoing interactions, such as asymmetries and/or

tails. This method makes use of several parameters for describing peculiar light distributions, such as the Concentration-Asymmetry-Smoothness parameters (CAS, Conselice, 2003) or the Gini- $M_{20}$  parameters (Lotz, Primack & Madau, 2004). This technique can identify mergers in a relatively late stage, but not all asymmetric galaxies are necessary merger features. The asymmetry method is similar to the technique used by Sancisi et al. (2008), whereas our approach on HI data-cubes is conceptually similar to the close pair method. The main difference is that we do not impose any limit for the projected distance between galaxies, whereas the velocity criterion is implicit in the data-cubes. Moreover, we select objects in 3D space (so potentially also overlapping in the sky) and we estimate the minimum time of collision for each galaxy independently.

The asymmetry and close pairs methods have been widely used with optical galaxy surveys, but, despite the large number of studies, there is little consensus on the galaxy merger rate and its evolution with redshift. Current observations of the fraction of galaxy undergoing a merger differ by an order of magnitude, from  $\sim 2\%$  (e.g., Patton et al., 2000; De Propris et al., 2007, 2.3% and 1.9%, respectively) to 15% (e.g., de Ravel et al., 2009) and its trend with redshift vary from no evolution (e.g., Jogee et al., 2009) to strong evolution (e.g., López-Sanjuan et al., 2009). These discrepancies mainly arise from the different criteria for galaxy counting, merger selection and bias in the galaxy samples. The value that we found ( $\sim 32\%$ ) is a companion fraction rather than a merger fraction as some companions that we considered are fairly far away from the main galaxies (Figure 4.4, right panel). It is therefore difficult to compare our fraction with the above mentioned values. Broadly speaking, our estimate, which is indeed an upper limit, is higher at least of a factor 2-3 because our program treats all multiple systems as mergers and, working with HI data, identifies more easily dwarf gas-rich companions compared to optical observations. However, if we exclude the very far away companions, namely those beyond 100 kpc of projected distance, we obtain a companion fraction of  $\sim 14\%$ , not too different from the values found with optical studies. Finally, we stress that the WHISP sample is insignificant compared to other local references based on large catalogues, such as the SDSS or the Millennium Galaxy Catalogue (MGC), so that our values are less reliable from a statistical point of view.

A recent study carried out by Holwerda et al. (2011) estimated the merger fraction and rate for the whole WHISP sample using both close pair and asymmetry methods on HI total maps. Holwerda et al. found a merger fraction of 7% based on pairs, and 13% based on disturbed morphology. We can not compare our merger fraction with the latter value, because our program ignores the galaxy morphology, but the former value is fully comparable and our estimate is significantly higher by about a factor 4. A possible reason of such a discrepancy is that Holwerda et al. based their pair fraction on 24 multiple systems previously identified and classified

as interacting by Noordermeer et al. (2005b) and Swaters et al. (2002b), whereas our code detected a much larger number of satellites (see Table 4.6). If we use this sub-sample, the merger fractions become closely comparable.

#### 4.4.4 Other channels for gas accretion

How star-forming galaxies can sustain their star formation is still an open question. In this study, we demonstrated that gas-rich minor mergers do not play a primary role in the nearby Universe and other dominant accretion channels must be admitted. A way to fill the discrepancy between the estimated accretion rates and the SFRs could be to assume that the HI mass function were much steeper in the recent past than now, so that the number of dwarf satellites to be accreted were much higher. However, no observational evidence in that direction can be achieved with the present generation of radio-telescopes and studies of the Damped Lyman  $\alpha$  systems show a remarkable constancy of the HI mass throughout the Hubble time (e.g., Prochaska & Wolfe, 2009). Another possibility is that the most accretion is supported by infalling of gas clouds with HI masses of  $10^7 - 10^6 M_{\odot}$ , but recent deep observations of nearby groups of galaxies (e.g., Pisano et al., 2007; Chynoweth et al., 2009), as well as large blind surveys, such as ALFALFA (Giovanelli et al., 2007), showed no evidence for a significant population of these small HI clouds. Moreover, studies on the Milky Way's High Velocity Clouds (HVCs) estimated a contribution to the total gas accretion of  $0.1 - 0.2 M_{\odot} \text{ yr}^{-1}$  (e.g., Wakker et al., 2007; Putman, Peek & Joung, 2012), a value much smaller than the SFR of the Milky-Way. In addition, the gas in the ionized phase could provide a further accretion at a rate of  $\sim 1 M_{\odot} \text{ yr}^{-1}$  (e.g., Shull et al., 2009), but it is not understood whether and how this gas can feed the star formation process in the disk. Numerical simulations (e.g., Fernández, Joung & Putman, 2012) support the idea that the most of the gas infall in Milky Way-like galaxies is continuously provided by a drizzle and filamentary cosmological accretion, which would be almost undetectable or very difficult to identify (e.g., Lehner et al., 2013; Tumlinson et al., 2013). Finally, large amounts of matter could be supplied by the cooling of the coronal gas (Anderson & Bregman, 2010) potentially triggered by supernova feedback (Marinacci et al., 2010).

## 4.5 Conclusions and future prospects

In this Chapter, we estimated the maximum accretion of cold gas from minor mergers in a sample of large spiral galaxies from the WHISP catalogue. We used the source finding algorithm implemented in <sup>3D</sup>BAROLO to detect dwarf HI-rich satellites around these spiral galaxies and we assumed that they will disappear and merge with the main galaxies in the shortest possible time. We found that  $\sim 22\%$  of galaxies have detected dwarf companions ( $M_{\text{bar,sat}}/M_{\text{bar,main}} \leq 0.20$ ) and we esti-

mated a maximum gas accretion rate onto the main galaxies over the whole sample of  $0.28 M_{\odot} \text{ yr}^{-1}$ . Given the assumptions, this value is a strong overestimate and the actual value can easily be an order of magnitude or more lower. From far-infrared luminosity, we calculated a mean star formation rate of  $1.29 M_{\odot} \text{ yr}^{-1}$ , a value which is nearly five times higher than the maximum gas accretion rate. These results strongly suggest that minor mergers can not bring enough gas to guarantee a long lasting star formation process in the disks of spiral galaxies. We note that our method can also detect, if present, large floating HI clouds and include them in the accretion budget. We did not find any significant population of these clouds. Thus, most of gas accretion seems to be hidden to the current investigations in HI emission.

WHISP is a fairly large sample of nearby galaxies, but it is very small compared to surveys carried out at other wavelengths. In the next future, the number of galaxies observed with radio interferometers will increase by three orders of magnitude, from a few hundreds to about  $10^5$ . It will be very interesting to apply the kind of analysis performed in this Chapter to those large galaxy samples.

**Table 4.6:** Detected companions of the WHISP spiral galaxies with  $M_{\text{bar,sat}}/M_{\text{bar,main}} \leq 0.20$ : (1) First name in NED archive or DF if not classified, (2) UGC name of the main galaxy, (3) celestial coordinates, (4) adopted distance [same as the main galaxy or taken from EDD catalogue, when specified], (5) systemic velocity, (6) line width  $W_{20}$  of the global profile at the 20% level, (6) total HI mass, (8) projected distance from the main galaxy (9) minimum time of collision with the main galaxy assuming the shortest parabolic orbit (see text), (10) firm upper limit to the gas accretion rate onto the main galaxy.

Name	Main galaxy	Coord. (J2000)	$D$	$V_{\text{sys}}$	$W_{20}$	$M_{\text{HI}}$	$d_{\text{proj}}$	$t_{\text{coll}}$	$\dot{M}_{\text{HI}}$
(1)	(2)	RA-Dec	Mpc	km/s	km/s	$10^8 M_{\odot}$	kpc	$10^8$ yr	$M_{\odot}/\text{yr}$
		(3)	(4)	(5)	(6)	(7)	(8)	(9)	(10)
AGC 102802	UGC 485	J004702.7+301243	58.9	5296	85	9.08	117	15.7	0.58
AGC 113996	UGC 624	J010107.2+304052	78.3	4762	29	8.76	119	11.6	0.75
AGC 113884	UGC 624	J010000.3+302357	78.3	4717	96	5.04	391	17.8	0.28
[VH2008] J0101+4744	UGC 625	J010118.4+474432	28.3	2795	62	3.02	36	4.5	0.67
DF1 <sup>†</sup>	UGC 1437	J015708.1+354825	54.5	4592	172	14.80	133	9.8	1.51
PGC 9994	UGC 2141	J030653.0+301542	24.7	812	43	7.37	75	5.6	1.32
PGC 2328690	UGC 2459	J030225.7+485452	32.4	2449	134	16.29	131	14.3	1.14
[KLT2208] HI J0302+352*	UGC 2487	J030210.5+351627	72.2	4933	55	15.43	351	18.1	0.85
[SOS2010] J0301491+3529012	UGC 2487	J030147.2+352839	72.2	4876	38	3.61	129	8.6	0.42
UGC2813	UGC 2800	J034234.1+711828	16.1 <sup>1</sup>	1381	62	0.99	33	4.2	0.24
HFLLZOA G136.96+14.21	UGC 2916	J040403.5+713707	68.0	4450	158	14.36	114	10.8	1.33
2MASX J04550438+3002212	UGC 3205	J045826.3+295653	47.6	3239	173	10.26	350	17.6	0.58
DF2 <sup>†</sup>	UGC 3205	J045504.2+300209	47.6	3530	47	5.03	184	9.7	0.52
DF3 <sup>†</sup>	UGC 3205	J045653.8+293602	47.6	3229	110	19.34	385	18.3	1.06
DF4 <sup>†</sup>	UGC 3382	J055903.3+621719	67.2	4407	64	3.83	160	12.6	0.30
DF5 <sup>†</sup>	UGC 3407	J060841.0+415647	39.3	3683	66	3.50	96	10.1	0.35

DF6 <sup>†</sup>	UGC 3407	J060913.3+420104	39.3	3688	114	4.51	48	7.9	0.57
DF7 <sup>†</sup>	UGC 3407	J060853.9+420338	39.3	3693	73	0.80	27	3.5	0.23
DF8 <sup>†*</sup>	UGC 3422	J061633.1+705743	77.2	4009	24	3.22	238	9.8	0.33
GALEX J061256.68+710650.6	UGC 3422	J061254.8+710659	77.2	3998	104	5.52	83	7.5	0.74
NPM1G +60.0018	UGC 3546	J065150.2+604122	17.9	1768	52	1.12	58	5.8	0.19
GALEX J070643.91+635521.0	UGC 3642	J070645.1+635515	67.3	4714	106	3.56	169	11.1	0.32
UGC 3660	UGC 3642	J070634.1+635056	67.3	4261	75	8.70	350	17.9	0.49
KUG 0829+227B	UGC 4458	J083247.7+223443	68.6	4621	231	12.80	105	12.4	1.03
MCG +10-13-030	UGC 4666	J085422.1+585908	16.0	1016	90	1.26	69	5.7	0.22
SDSS J091001.72+325659.8	UGC 4806	J091005.0+325607	25.5	2049	125	4.23	89	9.5	0.45
KUG 0906+333A	UGC 4806	J090919.5+330734	25.5	1897	60	1.88	18	5.7	0.33
SDSS J093137.13+292533.3	UGC 5060	J093138.0+292534	24.0	1608	77	0.53	117	9.9	0.05
KDG 059	UGC 5253	J095156.6+720439	16.6	1121	46	2.03	57	6.2	0.33
UGC 6797	UGC 6778	J114940.5+482533	17.1	962	81	7.28	87	8.5	0.86
SDSS J115027.42+490105.9	UGC 6778	J115027.4+490106	17.1	1120	31	1.67	138	11.2	0.12
UGC 6791	UGC 6786	J114923.6+264428	22.5 <sup>1</sup>	1866	274	5.38	111	10.0	0.54
SDSS J114820.16+562045.7	UGC 6787	J114820.6+562049	22.1	1080	28	0.62	105	7.6	0.08
UGC 6733	UGC 6787	J114535.7+555313	19.1 <sup>2</sup>	1158	187	5.26	130	10.3	0.51
UGC 6816	UGC 6787	J115047.5+562719	17.1 <sup>1</sup>	887	115	5.78	146	11.0	0.52
SDSS J122442.59+544441.3	UGC 7506	J122440.2+544448	36.0	2495	109	2.18	154	11.6	0.19
UGC 8005	UGC 7989	J125149.1+254644	14.3 <sup>1</sup>	1196	198	8.84	101	8.6	1.02
UGC 8254	UGC 8307	J131038.2+363807	19.1	1088	105	3.71	149	16.1	0.23
DF9 <sup>†*</sup>	UGC 8307	J131153.6+362758	19.1 <sup>1</sup>	954	75	1.92	100	14.2	0.14
UGC 8271	UGC 8307	J131131.3+361655	18.5 <sup>1</sup>	1145	150	6.99	156	22.1	0.32
DF10 <sup>†*</sup>	UGC 8307	J131134.3+362942	19.1	1191	32	0.58	109	15.5	0.04
KUG 1309+362	UGC 8307	J131146.7+355731	19.1	1123	26	0.30	245	24.9	0.01
UGC 8303	UGC 8307	J131317.6+361303	18.5 <sup>1</sup>	948	92	9.77	139	20.3	0.48

UGC 8314	UGC 8307	J131401.0+361908	19.1	938	71	1.06	113	21.2	0.05
MCG +08-27-001	UGC 9366	J143359.2+492647	38.9	2122	127	6.18	88	6.2	1.00
KUG 1512+557	UGC 9797	J151400.2+553222	46.6	3550	154	9.66	94	9.4	1.03
SDSS J152617.51+404004.0	UGC 9858	J152617.9+404008	32.2	2687	51	11.80	66	7.7	1.53
MCG +08-34-005	UGC 11283	J183400.4+492233	30.0	2076	63	3.75	51	7.5	0.50
GALEX J215645.61+275419.5	UGC 11852	J215645.7+275418	82.4	5710	46	5.30	221	15.2	0.35
ZOAG G095.92-08.72	UGC 11951	J221145.4+453649	14.2	1145	78	7.52	74	8.3	0.91

<sup>†</sup> Not catalogued in the NED, HyperLEDA or SIMBAD archives.

\* No clear optical/UV counterpart in DSS, SDSS or GALEX images. The DF8 field is not covered by the SDSS survey.

<sup>1</sup> Distance from EDD catalogue.

**Table 4.7:** Properties of the main galaxies selected from the WHISP sample: (1) UGC name, (2) alternative name, (3) adopted distance, (4)-(5) radius  $R_{25}$ , i.e. the length of the projected semi-major axis at the isophotal level of 25 mag arcsec $^{-2}$ , in arcmin and kpc respectively, (6) inclination from HyperLEDA, (7) systemic velocity, (8) line width of the global profile at the 20% level, (9) total HI mass estimated in this work, (10) adopted baryonic mass, calculated as described in [Section 4.1.3](#), (11) star formation rate calculated from the 60 $\mu$ m and 100 $\mu$ m IRAS fluxes ([Section 4.1.2](#)), (12) total gas accretion rate estimated in this work, including detectable and “hidden” accretion.

UGC name	Other name	$D$ Mpc	$R_{25}$ '	$R_{25}$ kpc	$i$ °	$V_{\text{sys}}$ km/s	$W_{20}$ km/s	$M_{\text{HI}}$ $10^9 M_{\odot}$	$M_{\text{bar}}$ $10^9 M_{\odot}$	SFR $M_{\odot}/\text{yr}$	$\dot{M}_{\text{HI}}$ $M_{\odot}/\text{yr}$
(1)	(2)	(3)	(4)	(5)	(6)	(7)	(8)	(9)	(10)	(11)	(12)
UGC 00094	NGC 0026	68.6 <sup>1</sup>	0.56	11	47	4587	320	9.63	53.34	1.17	0.04
UGC 00232	-	65.3 <sup>2</sup>	0.52	10	51	4837	275	7.61	38.40	1.95	0.10
UGC 00485	-	58.9 <sup>1</sup>	1.15	20	83	5246	357	21.63	45.84	1.27	0.90
UGC 00528	NGC 0278	12.0	1.17	4	20	640	138	1.32	15.68	1.02	0.01
UGC 00624	NGC 0338	78.3 <sup>1</sup>	0.87	20	68	4770	560	15.61	173.95	5.14	1.09
UGC 00625	IC 0065	28.3	1.29	11	73	2628	360	7.68	27.05	1.12	0.74
UGC 00690	-	74.5 <sup>1</sup>	0.85	18	46	5872	325	9.61	56.80	0.54	0.64
UGC 00731	-	12.0	0.93	3	24	639	143	0.88	38.54 <sup>4</sup>	0.21	0.01
UGC 00798	IC 1654	69.4 <sup>2</sup>	0.50	10	40	4898	222	3.96	43.96	0.60	0.11
UGC 01013	NGC 0536	62.5 <sup>1</sup>	1.48	27	69	5187	525	8.26	109.87	1.25	0.28
UGC 01256	NGC 0672	8.3	3.54	9	67	431	240	7.56	13.99	0.18	0.01
UGC 01437	NGC 0753	54.5 <sup>2</sup>	0.69	11	51	4905	339	11.58	83.23	4.09	1.74
UGC 01550	NGC 0801	52.2 <sup>1</sup>	1.38	21	78	5764	470	15.86	75.68	2.33	0.17
UGC 01633	NGC 0818	58.1 <sup>1</sup>	1.09	18	70	4258	501	11.35	88.10	2.57	0.21
UGC 01810	-	109.8 <sup>3</sup>	0.87	28	69	7578	602	31.64	210.16	2.37	0.88
UGC 01856	-	41.3 <sup>2</sup>	1.07	13	81	4804	270	11.37	21.89	0.23	0.07

UGC 01886	-	67.4 <sup>2</sup>	0.26	5	57	4854	502	25.67	121.29	0.85	0.33
UGC 01913	NGC 0925	9.2	5.36	14	58	552	222	3.85	12.90	0.64	<0.01
UGC 01993	-	107.7 <sup>1</sup>	0.89	28	75	8018	526	13.70	95.49	1.24	1.03
UGC 02045	NGC 0972	21.7	1.66	10	61	1525	332	2.12	45.93	4.42	<0.01
UGC 02069	-	36.6 <sup>1</sup>	0.62	7	55	3780	255	4.15	17.71	1.10	0.07
UGC 02080	IC 0239	10.0	2.13	6	24	902	135	5.46	11.52	0.16	0.01
UGC 02082	-	14.7	2.56	11	79	702	215	1.36	4.64	0.04	0.01
UGC 02141	NGC 1012	24.7	1.04	8	60	987	233	2.20	17.53	1.36	1.33
UGC 02154	NGC 1023	10.2	3.71	11	70	695	482	2.21	44.83	0.78	0.01
UGC 02183	NGC 1056	21.7	0.93	6	61	1540	290	3.65	18.80	0.98	0.01
UGC 02459	-	32.4	1.17	11	83	2467	337	12.30	31.48	0.59	1.28
UGC 02487	NGC 1167	72.2 <sup>3</sup>	0.91	19	41	4953	468	16.65	261.23	3.21	1.36
UGC 02503	NGC 1169	32.4	1.66	16	54	2391	461	9.69	95.99	1.12	0.12
UGC 02800	-	18.9 <sup>1</sup>	1.17	6	60	1187	217	2.01	5.05	1.52	0.25
UGC 02855	-	14.4 <sup>1</sup>	1.77	7	65	1196	453	6.35	49.22	2.22	0.02
UGC 02916	-	68.0 <sup>2</sup>	0.66	13	24	4517	336	23.12	94.12	2.45	1.40
UGC 03013	NGC 1530	25.4	0.91	7	55	2459	341	8.98	53.03	2.07	0.03
UGC 03137	-	22.1	1.90	12	78	993	216	4.41	9.32	0.15	0.02
UGC 03205	-	47.6 <sup>2</sup>	0.66	9	66	3588	436	9.21	65.30	0.95	2.18
UGC 03326	-	77.6 <sup>1</sup>	1.66	37	84	4060	532	19.48	135.84	2.38	0.05
UGC 03334	NGC1961	59.5 <sup>3</sup>	2.23	39	50	3935	660	39.72	422.71	9.24	0.26
UGC 03354	-	52.5 <sup>1</sup>	0.83	13	70	3085	441	8.89	68.85	3.22	0.02
UGC 03382	-	67.2 <sup>3</sup>	0.63	12	21	4501	205	5.74	73.75	0.76	0.34
UGC 03407	-	39.3 <sup>2</sup>	0.56	6	45	3602	312	1.75	22.06	0.70	1.17
UGC 03422	-	77.2 <sup>2</sup>	0.91	20	62	4065	416	11.05	73.40	1.08	1.00
UGC 03546	NGC 2273	17.9	1.15	6	53	1836	339	1.95	19.09	0.56	0.21
UGC 03574	-	17.1	0.74	4	30	1441	150	3.21	6.70	0.35	0.02

UGC 03580	-	25.9	1.07	8	57	1198	236	3.81	12.87	0.48	0.02
UGC 03642	-	67.4 <sup>2</sup>	0.76	15	41	4498	410	37.21	146.52	1.99	0.89
UGC 03734	NGC 2344	23.0	1.02	7	24	972	150	1.12	14.80	0.11	0.01
UGC 03759	NGC 2347	88.3 <sup>1</sup>	0.83	21	44	4416	468	22.39	200.89	5.72	0.40
UGC 03993	-	66.3 <sup>3</sup>	0.42	8	24	4365	175	7.13	50.87	0.91	0.04
UGC 04036	NGC 2441	44.7 <sup>1</sup>	1.00	13	24	3469	141	4.07	31.61	0.89	0.11
UGC 04165	NGC 2500	15.0	1.23	5	25	515	113	0.97	6.82	0.35	<0.01
UGC 04256	NGC 2532	51.6 <sup>2</sup>	0.83	12	34	5256	175	6.73	56.96	3.70	0.10
UGC 04273	NGC 2543	26.3	1.23	9	62	2473	317	4.32	20.75	1.23	0.11
UGC 04284	NGC 2541	11.2	1.51	5	59	559	210	4.91	8.32	0.08	<0.01
UGC 04458	NGC 2599	68.6 <sup>3</sup>	0.77	15	32	4757	285	12.52	128.09	1.39	1.09
UGC 04605	NGC 2654	22.7	2.23	15	78	1354	430	6.32	35.50	0.82	0.01
UGC 04666	NGC 2685	16.0	2.18	10	58	876	303	1.96	17.39	0.14	0.22
UGC 04806	NGC 2770	25.5	1.73	13	76	1945	353	5.42	19.53	0.64	0.85
UGC 04838	NGC 2776	36.0	1.07	11	65	2626	202	6.24	44.41	1.53	0.03
UGC 04862	NGC 2782	42.1	1.62	20	42	2540	196	4.12	67.81	4.49	0.01
UGC 05060	NGC 2893	24.0	0.51	4	36	1700	187	0.92	6.66	0.42	0.05
UGC 05079	NGC 2903	8.5	6.01	15	63	555	390	3.95	39.88	0.95	<0.01
UGC 05251	NGC 3003	19.6 <sup>1</sup>	2.39	14	77	1481	294	8.89	20.10	0.40	0.02
UGC 05253	NGC 2985	16.6	1.82	9	36	1324	316	11.62	55.21	0.82	0.37
UGC 05351	NGC 3067	20.6	1.02	6	71	1487	281	0.91	15.67	1.17	0.01
UGC 05452	NGC 3118	20.6	1.04	6	78	1348	216	3.41	5.91	0.07	0.02
UGC 05459	-	25.8	1.90	14	79	1108	282	4.82	18.06	0.48	0.02
UGC 05532	NGC 3147	39.8	2.04	24	29	2812	390	9.50	227.06	4.95	0.13
UGC 05556	NGC 3187	26.4	1.12	9	71	1582	276	1.09	5.48	0.48	0.06
UGC 05557	NGC 3184	13.0	3.71	14	21	593	146	3.95	32.47	0.20	0.01
UGC 05589	NGC 3206	25.8	1.15	9	59	1162	182	2.61	6.50	0.03	0.06

UGC 05685	NGC 3254	21.8	1.17	7	72	1359	378	4.71	24.34	0.22	0.10
UGC 05717	NGC 3259	24.0	0.85	6	58	1675	242	6.34	14.71	0.43	0.05
UGC 05786	NGC 3310	20.0	0.95	6	40	989	221	3.36	17.42	3.23	0.02
UGC 05789	NGC 3319	13.3	1.82	7	61	739	215	3.36	6.76	0.06	0.01
UGC 05840	NGC 3344	10.0	3.38	10	25	589	175	3.01	17.40	0.25	<0.01
UGC 05906	NGC 3380	26.1	0.77	6	27	1600	130	0.42	9.70	0.15	0.01
UGC 05909	NGC 3381	25.7	1.00	7	26	1633	146	2.12	9.07	0.34	0.02
UGC 05918	-	10.0	1.23	4	12	338	78	0.25	0.57	0.09	<0.01
UGC 05997	NGC 3403	20.2	1.38	8	68	1261	303	4.09	12.89	0.46	0.03
UGC 06024	NGC 3448	24.0	1.48	10	73	1369	299	6.76	21.06	1.12	0.05
UGC 06128	NGC 3512	26.1	0.79	6	29	1388	187	0.98	13.03	0.35	0.01
UGC 06225	NGC 3556	9.6	1.99	6	65	698	341	3.48	22.10	0.81	0.02
UGC 06263	NGC 3583	33.0	1.12	11	56	2134	346	6.65	69.34	2.59	0.07
UGC 06283	NGC 3600	14.4	0.93	4	72	713	218	2.86	6.14	0.26	0.01
UGC 06537	NGC 3726	17.1	2.62	13	47	864	284	5.05	35.11	0.46	0.01
UGC 06621	NGC 3786	40.0	0.97	11	59	2745	418	4.56	42.88	1.27	0.02
UGC 06778	NGC 3893	17.1	1.35	7	58	968	311	4.76	31.95	1.59	0.99
UGC 06786	NGC 3900	22.5	1.29	8	61	1801	426	3.33	25.43	0.24	0.56
UGC 06787	NGC 3898	22.1	1.73	11	54	1170	446	3.96	57.99	0.96	1.12
UGC 06833	NGC 3930	12.6	1.35	5	42	918	161	0.99	7.00	0.36	0.01
UGC 06870	NGC 3953	19.2 <sup>1</sup>	3.09	17	62	1051	403	2.35	72.36	0.30	0.09
UGC 06884	NGC 3963	49.1 <sup>2</sup>	1.26	18	27	3189	131	8.21	68.56	1.76	0.09
UGC 06930	-	17.1	0.71	4	42	778	141	2.52	4.77	0.19	0.01
UGC 06964	NGC 4010	19.1 <sup>1</sup>	1.55	9	78	905	278	1.40	8.52	0.28	0.01
UGC 07030	NGC 4051	17.2	2.45	12	40	704	241	1.43	33.28	0.86	0.01
UGC 07081	NGC 4088	14.5 <sup>1</sup>	3.54	15	68	756	381	4.15	32.18	1.51	0.01
UGC 07095	NGC 4100	20.3 <sup>1</sup>	2.29	14	74	1075	402	3.02	35.53	1.21	0.03

UGC 07183	NGC 4157	18.0	3.08	16	80	771	422	6.29	54.12	1.69	0.03
UGC 07222	NGC 4183	16.4 <sup>1</sup>	2.13	10	81	931	247	2.95	7.98	0.20	0.01
UGC 07256	NGC 4203	15.1	1.69	7	65	1088	270	2.34	33.99	0.10	<0.01
UGC 07321	-	6.0	2.39	4	86	407	210	0.34	0.72	0.08	0.01
UGC 07399	NGC 4288	9.2	0.85	2	41	535	165	0.74	1.35	0.35	0.01
UGC 07483	NGC 4359	16.3	0.69	3	53	1271	199	1.13	3.14	0.21	0.01
UGC 07489	NGC 4369	11.2	1.00	3	17	1029	88	0.43	4.83	0.33	0.02
UGC 07506	NGC 4384	36.0	0.63	7	39	2532	176	1.13	12.87	0.84	0.20
UGC 07766	NGC 4559	8.7	5.24	13	63	814	256	5.43	16.21	0.22	<0.01
UGC 07989	NGC 4725	12.4	4.89	18	45	1210	398	5.02	71.56	1.06	1.03
UGC 08307	NGC 5033	19.1 <sup>1</sup>	9.77	54	65	875	425	10.43	88.98	1.76	1.27
UGC 08403	NGC 5112	18.5	1.51	8	52	969	215	3.12	8.53	0.35	0.01
UGC 08699	NGC 5289	30.9	1.17	11	72	2518	352	2.76	18.81	0.23	0.02
UGC 08709	NGC 5297	30.9	1.86	17	76	2405	414	12.73	50.61	1.05	0.09
UGC 08711	NGC 5301	20.2	1.99	12	78	1508	336	3.56	18.33	0.81	0.04
UGC 08863	NGC 5377	28.0	1.82	15	67	1791	382	2.24	47.16	0.42	0.01
UGC 08900	NGC 5395	52.7 <sup>2</sup>	1.26	19	62	3458	565	11.21	143.67	3.53	0.25
UGC 09242	-	27.9	2.08	17	86	1438	215	3.20	6.43	0.21	0.01
UGC 09366	NGC 5676	38.9	1.82	21	63	2121	462	6.41	137.46	5.76	1.09
UGC 09431	NGC 5714	38.7 <sup>1</sup>	1.41	16	80	2242	356	7.51	29.58	0.66	0.14
UGC 09644	-	97.9 <sup>3</sup>	0.57	16	20	6664	136	7.12	42.84	1.28	0.11
UGC 09753	NGC 5879	15.5	1.90	9	68	771	287	1.32	10.88	0.28	0.01
UGC 09797	NGC 5905	46.6 <sup>1</sup>	1.62	22	50	3393	374	22.70	73.72	2.56	1.25
UGC 09858	-	32.2	1.95	18	78	2615	386	10.67	28.75	0.41	1.66
UGC 09969	NGC 5985	43.7	1.99	25	60	2515	542	10.76	144.58	1.19	0.14
UGC 10359	NGC 6140	16.0	1.04	5	44	908	221	5.41	11.61	0.14	0.01
UGC 10445	-	18.1	0.95	5	45	962	159	2.23	6.94	0.16	0.05

UGC 10448	NGC 6186	154.0 <sup>2</sup>	0.79	35	41	11352	118	9.56	439.96	8.82	0.02
UGC 10470	NGC 6217	23.0	1.12	7	34	1355	192	5.94	30.66	1.86	0.02
UGC 10497	-	65.6 <sup>2</sup>	0.59	11	65	4296	267	8.93	21.34	0.36	0.17
UGC 10564	NGC 6237	21.0	0.62	4	52	1129	175	5.64	11.08	0.27	0.03
UGC 11124	-	25.0	1.12	8	26	1599	153	2.23	11.71	0.16	0.03
UGC 11218	NGC 6643	20.6	1.66	10	61	1484	350	3.20	30.27	1.78	0.04
UGC 11269	NGC 6667	44.9	0.93	12	56	2581	412	13.36	66.90	1.73	0.02
UGC 11283	IC 1291	30.0	0.66	6	35	1946	198	2.55	9.44	0.38	0.55
UGC 11429	NGC 6792	62.2 <sup>1</sup>	1.04	19	58	4637	510	12.26	129.81	1.60	0.31
UGC 11466	-	18.1	0.74	4	53	821	237	2.79	10.96	0.84	0.01
UGC 11670	NGC 7013	15.0	2.08	9	71	775	340	1.35	26.16	0.28	<0.01
UGC 11852	-	82.4 <sup>2</sup>	0.46	11	44	5845	328	26.73	82.67	0.96	0.45
UGC 11861	-	14.4	0.89	4	61	1482	259	2.10	10.25	0.47	0.02
UGC 11909	-	14.1	1.00	4	78	1105	242	2.87	7.78	0.39	0.01
UGC 11914	NGC 7217	15.0	2.29	10	35	950	301	0.70	52.88	0.68	<0.01
UGC 11951	NGC 7231	14.2	0.85	4	69	1086	223	1.56	4.97	0.35	0.92
UGC 11994	-	65.8 <sup>1</sup>	1.04	20	82	4882	436	6.95	57.44	1.69	0.29
UGC 12554	NGC 7640	9.9	4.06	12	78	363	238	3.05	8.78	0.24	<0.01
UGC 12693	-	60.5 <sup>1</sup>	0.55	10	78	4958	236	9.67	15.50	0.69	0.12
UGC 12732	-	15.1	1.38	6	28	728	131	1.96	4.06	0.59	0.01
UGC 12754	NGC 7741	13.6 <sup>1</sup>	1.82	7	49	749	202	1.78	5.76	0.36	0.01
UGC 12808	NGC 7769	61.5 <sup>3</sup>	0.87	16	68	4225	326	4.79	134.32	6.21	0.05

<sup>1</sup> Distance from Cosmicflows-2 catalogue.

<sup>2</sup> Distance from NED catalogue.

<sup>3</sup> Distance from Hubble flow with Virgo infall corrected systemic velocity.

<sup>4</sup> Baryonic mass from baryonic Tully-Fisher relation.

## Rotation curves and velocity dispersions of high- $z$ galaxies<sup>†</sup>

ABSTRACT — In this Chapter, we used <sup>3D</sup>BAROLO to kinematically model a sample of ten star-forming galaxies at  $z \sim 1$  observed in the H $\alpha$  emission-line with the VLT/KMOS . The 3D modeling of our  $z \sim 1$  sample revealed that 1) the rotation curves of these galaxies rise very steeply within the inner kiloparsec and then remain remarkably flat out to the outermost radius and 2) the H $\alpha$  velocity dispersions are quite low, ranging from 15 to 40 km/s. Both these features are similar to those of disks in the local Universe. In addition, these systems lie on the Tully-Fisher relation of local spiral galaxies. These results show how disks with normal star formation rates (non star-bursting) are fully settled and rotation dominated with  $V/\sigma = 3-10$  already at  $z \sim 1$ .

In the last decade the advent of Integral Field Spectroscopy (IFS) has remarkably widened our possibilities of investigating the physical properties of galaxies in the high-redshift Universe. Several surveys have taken advantage of the new generation of Integral Field Units (IFUs), such as the SINS/ $z$ C-SINF (Förster Schreiber et al., 2009) and MASSIV (Contini et al., 2012) surveys with the Spectrograph for INtegral Field Observations in the Near Infrared (SINFONI, Eisenhauer et al., 2003), the OSIRIS survey (Law et al., 2007, 2009) with Keck/OSIRIS (Larkin et al., 2006), KMOS<sup>3D</sup> (Wisnioski et al., 2015) and KROSS (Stott et al., in prep) with the K-band Multi-Object Spectrograph (KMOS, Sharples et al., 2013). These surveys have observed high- $z$  star-forming galaxies and mapped their kinematics through optical/near-infrared emission lines, such as H $\alpha$ , N and O lines, tracing the ionized phase of the warm gas and the on-going star formation.

Spatially resolved information on the kinematics and dynamics of high- $z$  systems

---

<sup>†</sup>Based on E. M. Di Teodoro, S. H. Miller, & F. Fraternali, in preparation

can provide new insights to draw the evolutionary picture of galaxies in the epoch near the peak of cosmic star formation rate (SFR) at  $z \sim 1 - 3$ . In this epoch, the baryonic mass assembly was likely regulated by the interplay between the gas accretion from the intergalactic medium (IGM) or mergers and the stellar/AGN feedback (e.g., Dekel, Sari & Ceverino, 2009; Dutton, van den Bosch & Dekel, 2010; Lilly et al., 2013). The tight relation between SFR and stellar mass ( $M_*$ ), the so-called “main-sequence” (MS) of galaxies (e.g., Elbaz et al., 2011; Speagle et al., 2014), supports the scenario of a relatively smooth growth of galaxies in disk-like structures with respect to bursts of star formation driven by merger episodes (e.g., Rodighiero et al., 2011). The *in situ* growth rapidly ceases at  $M_* > 10^{11} M_\odot$  and above this stellar mass, galaxies appear already quenched at  $z \sim 2.5$  (e.g., Whitaker et al., 2012). In this context, the study of the kinematics of high- $z$  galaxies can supply unique information on the internal dynamical state of these systems, revealing for instance signs of merger-driven or secular mass growths.

Kinematic studies through IFS revealed that the majority of star-forming galaxies in the stellar mass range  $10^9 < M_*/M_\odot < 10^{11}$  at  $z > 1$  are disk-like systems (e.g., Förster Schreiber et al., 2009; Genzel et al., 2008; Epinat et al., 2009, 2012; Tacchella et al., 2015), with an actual fraction of disks shifting from an initial estimate of 30% (Genzel et al., 2006; Förster Schreiber et al., 2006) to 80 – 90% (Wisnioski et al., 2015). These star-forming disk galaxies are rotationally supported with circular velocities of 100-300  $\text{km s}^{-1}$  already about 2 Gigayears after the Big Bang (e.g., Cresci et al., 2009; Gnerucci et al., 2011). The predominance of disk-like kinematics over irregular or dispersion-dominated kinematics seems to be in favor of a smooth mass growth of galaxies. However, the  $\text{H}\alpha$  velocity dispersions currently measured in these systems are of the order of 50-100  $\text{km s}^{-1}$  (Glazebrook, 2013), a factor 2-4 higher than the values found in local spiral galaxies (Epinat et al., 2010), suggesting that disks at high redshift are morphologically and dynamically different from local ones. The general picture is that young disks were much more turbulent in the past and then they evolved towards a cooler dynamical state, with an increasing  $V/\sigma$  over the cosmic time (see Section 1.2.2).

The kinematics is used also to study the evolution of the scaling relations throughout cosmic time, in particular the Tully-Fisher relation (TFR, Section 1.4), related to how disk galaxies assembled. The stellar mass TFR (i.e.  $M_*$  vs  $V_{\text{rot}}$ ) at low redshift is well constrained (e.g., Bell & de Jong, 2001; Meyer et al., 2008), but at intermediate-high redshifts the derived relations have larger scatter (Conselice et al., 2005; Kassin et al., 2007) and are often biased by selection criteria. Despite a conspicuous number of studies have been carried out both with long slit and IFU observations, it is still debated whether the relation and in particular its zero point evolves with redshift (e.g., Weiner et al., 2006; Puech et al., 2008; Dutton et al., 2011) or not (e.g., Flores et al., 2006; Miller et al., 2011, 2012).

The main limitation of IFU observations of high- $z$  galaxies is the spatial resolution. With no adaptive optics (AO), the best achievable spatial resolution is of the order of 0.5-1 arcsec imposed by the atmosphere. A galaxy at redshift  $z \sim 1-2$  with typical size of  $\sim 2''$  may therefore be observed with less than 3-4 resolution elements along the whole galaxy disk. In these conditions, the PSF of the instrument have strong effects on the extraction of the kinematic maps, i.e. the velocity field and the velocity dispersion field, from the emission-line datacubes and on the derivation of the kinematic parameters (see [Section 3.3](#)). As mentioned in [Section 2.3](#), the beam smearing causes a degeneracy between the measured rotation velocity, which ends up being underestimated, and the velocity dispersion, which can be severely overestimated, especially in the inner regions of a galaxy. A correction for beam smearing is usually applied in IFS high-redshift studies. Nevertheless, high- $z$  galaxies re-observed with AO have systematically shown a shift from dispersion to rotation-dominated classification (Förster Schreiber et al., 2009). However, AO provide higher spatial resolutions but at a considerable loss in term of signal-to-noise (S/N), which is not desirable for high- $z$  low-surface-brightness galaxies. Moreover the larger sensitivity of natural seeing observations can reveal the fainter edges of galaxies and allows a better sampling of the flat part of the rotation curves as well as more reliable measurements of the velocity dispersion.

In this Chapter, we use <sup>3D</sup>BAROLO to kinematically model a sample of ten star forming galaxies at  $z \sim 1$  observed in the H $\alpha$  emission line with the KMOS IFU at the VLT. As shown in [Chapter 3](#), our method takes advantage of the full information available in datacubes and the derived rotation velocities and velocity dispersions are not biased by beam smearing. The Chapter is organized as follows. In [Section 5.1](#) we describe the sample and the selection criteria of our  $z \sim 1$  disk galaxies. The kinematic modeling is discussed in [Section 5.2](#). In [Section 5.3](#), we show the results and we compare them with previous kinematic studies. We assume a flat  $\Lambda$ CDM cosmology with  $\Omega_{m,0} = 0.27$ ,  $\Omega_{\Lambda,0} = 0.73$  and  $H_0 = 70 \text{ km s}^{-1} \text{ Mpc}^{-1}$ . For this cosmology,  $1''$  corresponds to 8.16 kpc at  $z = 1$ . At the same redshift, the look-back time is 7.8 Gyr. Magnitudes are always given in the AB system.

## 5.1 Data sample

Galaxies in our sample were observed with the KMOS IFU at the VLT as part of the KMOS Redshift One Spectroscopic Survey (KROSS, Bower & Bureau, 2014, Stott et al., submitted). The KROSS survey, upon completion, will have observed H $\alpha$  emission from about 1000 typical star-forming galaxies at  $z = 0.85 - 1$ . Most of the KROSS galaxies belong to well studied fields of large surveys, such as the Ultra Deep Survey (UDS), the Cosmological Evolution Survey (COSMOS) and The Great Observatories Origins Deep Survey (GOODS), and have accurate spectro-

scopic redshifts. Galaxy selection was made by applying an observed magnitude cut  $K_{AB} < 22.5$  and a color cut  $r - z < 1$  in order to favor blue star-forming galaxies.

We extracted a small sub-sample of galaxies from the KROSS survey based on the following criteria. We requested an integrated  $H\alpha$  flux  $F_{H\alpha} > 5 \times 10^{-17} \text{ erg s}^{-1} \text{ cm}^{-2}$ , so that we have an acceptable S/N and we can identify galaxy emission regions with confidence. Galaxies were requested not to be merging systems and to have redshifts such that the  $H\alpha$  emission does not overlap any line of the sky. Finally, we selected galaxies that have inclination angles in the interval  $30^\circ < i < 70^\circ$ . Below  $30^\circ$ , rotation curves become highly uncertain due to the smaller rotational component along the line of sight and the large impact of inclination errors. In addition, more inclined disks extend over a larger number of spectral channels, giving more information to constrain the models. Above  $i \sim 70^\circ$ , our approach could progressively underestimate rotation velocity and overestimate velocity dispersion in the inner regions of galaxies (see Section 3.4). These criteria guarantee the best possible reliability for our 3D kinematic modeling.

Our final sample includes ten star-forming galaxies. All galaxies are in the COSMOS or GOODS-S fields, seven of them are also included in the 3D-HST Treasury Survey (3D-HST, Brammer et al., 2012; Skelton et al., 2014). In Figure 5.1, we show rest-frame blue-band images from The Cosmic Assembly Near-infrared Deep Extragalactic Legacy Survey (CANDELS, Grogin et al., 2011),  $H\alpha$  total intensity maps (0<sup>th</sup> moment),  $H\alpha$  velocity fields (1<sup>st</sup> moment) and  $H\alpha$  velocity dispersion maps (2<sup>nd</sup> moment). Table 5.7 summarizes the main properties of our galaxy sample. Stellar masses are taken from the 3D-HST or COSMOS catalogs and are derived using the Fitting and Assessment of Synthetic Templates (FAST, Kriek et al., 2009), a code that basically fits stellar population synthesis templates (Bruzual & Charlot, 2003) to broadband photometry. The assumed initial mass function is that of Chabrier (2003). Star formation rates are calculated from the measured  $H\alpha$  luminosities, following Kennicutt (1998) ( $\text{SFRs}[\text{M}_\odot \text{ yr}^{-1}] = 7.9 \times 10^{-42} L_{H\alpha} [\text{erg s}^{-1}]$ ). Since no correction for the global dust extinction has been applied, these SFRs may be read as lower limits. Nevertheless they give an idea of the non-starbusting nature of these galaxies. The velocity fields of these galaxies show that these systems are regularly rotating disks. Given the range of stellar masses ( $9.5 < \log(\text{M}_*/\text{M}_\odot) < 10.5$ ) and SFRs ( $1 < \text{SFRs} < 10 \text{ M}_\odot \text{ yr}^{-1}$ ), these systems are good candidates to be the progenitors of Milky Way-like galaxies at  $z \sim 0$ .

Data reduction was performed by the KROSS team<sup>1</sup>, including flat fielding, wavelength calibration and sky subtraction (Davies et al., 2011, 2013). The final set of data includes fully reduced data-cubes, unskysubtracted raw data-cubes and data-cubes of stars observed during the pointing of scientific targets.

<sup>1</sup>The reduced data-cubes have been kindly provided to us by M. Bureau, R. G. Bower and A. Tiley.

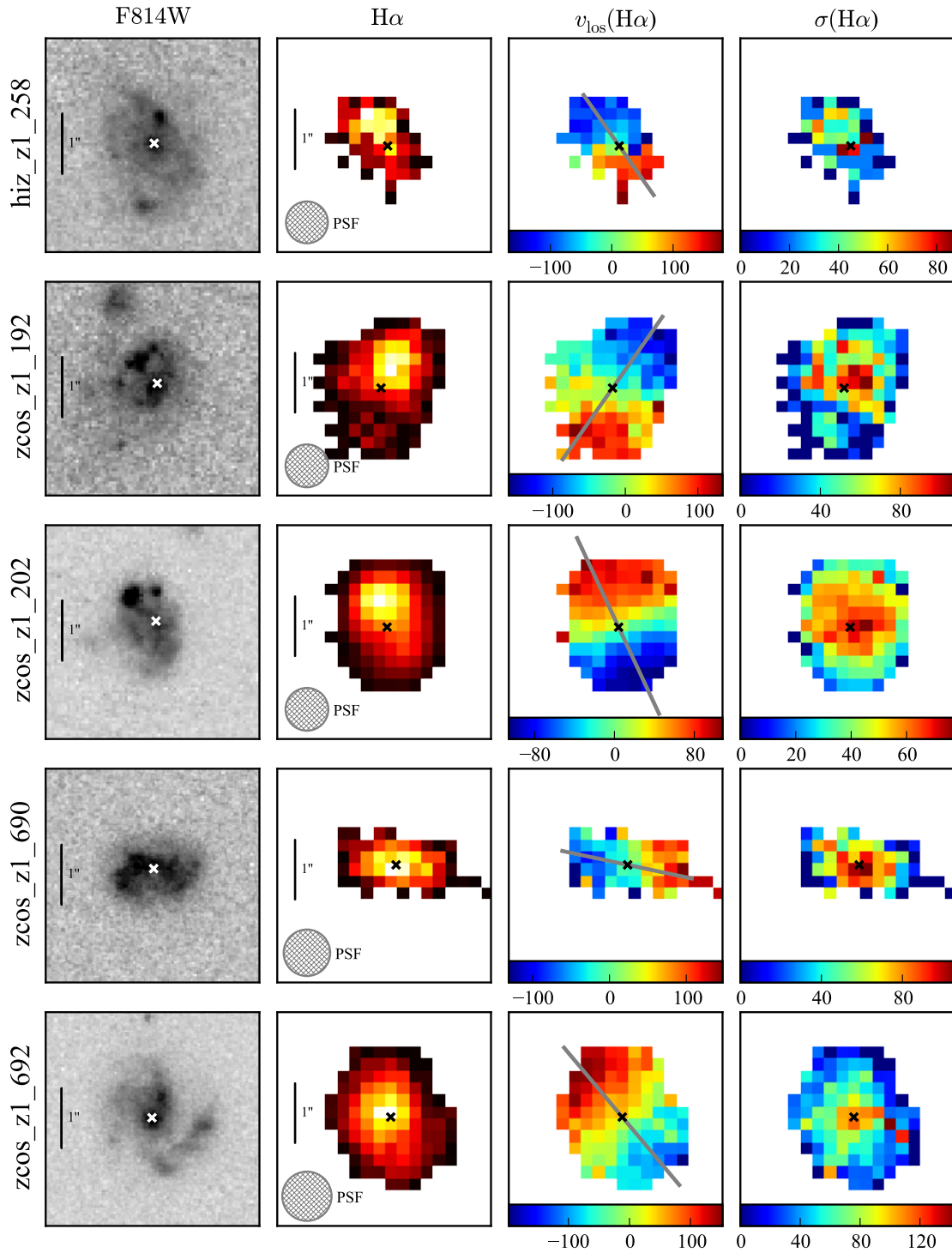


**Figure 5.1:** The galaxy sample used in this work. From the *left* to the *right*: HST images in the F814W filter (roughly corresponding to  $I$ ) from the CANDELS survey, total  $H\alpha$  intensity maps,  $H\alpha$  velocity fields and  $H\alpha$  velocity dispersion maps (not corrected for beam smearing and instrumental broadening). Moment maps are extracted from the KMOS datacubes used in this Chapter. White and black crosses are the adopted centers, the gray thick line is the adopted kinematic position angle. Color bars are in km/s.

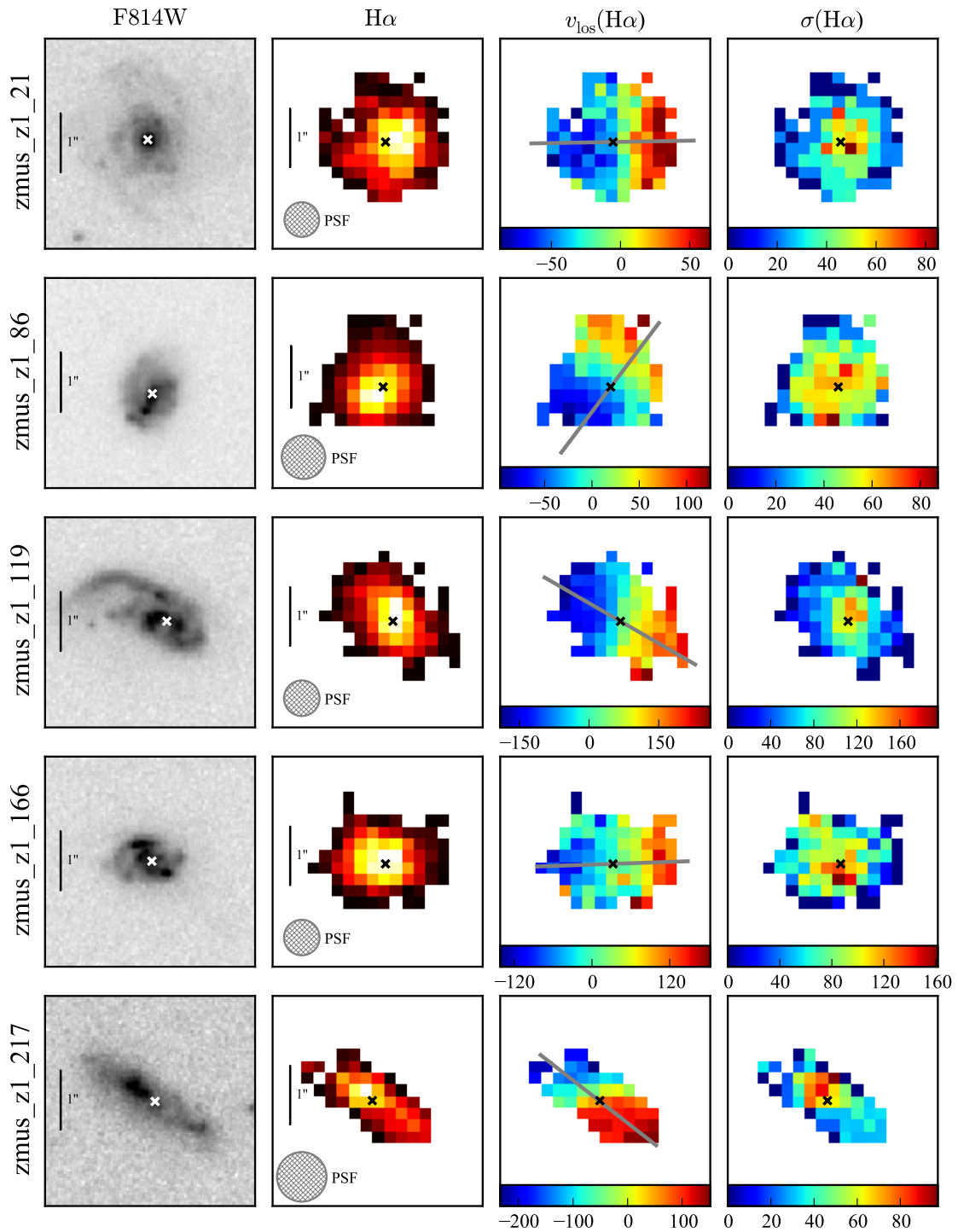


Figure 5.1: Continued

## 5.2 Kinematic modeling

We modeled the kinematics of the galaxy in our sample by using <sup>3D</sup>BAROLO (Chapter 2). The main advantage of modeling the 3D data-cubes instead of the 2D maps is that the instrumental effects, i.e. the Point Spread Function (PSF), which determines the spatial resolution, and the Line Spread Function (LSF), which describes the spectral broadening, are incorporated directly in the model. The PSF for each galaxy was obtained by a 2D Gaussian fit of the stars observed in each pointing. Since the observations have been carried in natural seeing mode, the typical spatial resolution is  $\text{FWHM} \sim 0.6'' - 0.8''$ . The spectral broadening is taken from a Gaussian fit of the hydroxyl (OH) sky emission lines in the unskysubtracted datacubes at wavelengths close to the H $\alpha$  emission of each galaxy. The resulting LSFs have typically variance  $\sigma_{\text{instr}} \sim 25 - 30 \text{ km s}^{-1}$ .

The modeling with <sup>3D</sup>BAROLO requires the initial estimate of the coordinates of the center, the inclination and the position angles. We used publicly available Hubble Space Telescope (HST) images from the CANDELS survey (Grogin et al., 2011) to determine the centers of the galaxies. The inclination angles were estimated by fitting a PSF-convoluted disk model to the total H $\alpha$  intensity maps (see Section 2.5.2). Velocity fields, derived through Gaussian fits to the line profiles, were used to infer the kinematic position angles. Adopted centers and position angles are shown in Figure 5.1 as crosses and grey thick lines, respectively. Accurate spectroscopic redshifts were taken from the 3D-HST and COSMOS catalogs and used as spectral center for the H $\alpha$  emission line.

The galaxy emission regions in each channel map of the data-cubes were identified by taking only pixels with fluxes larger than  $1.5-2.5\sigma_{\text{noise}}$ , depending on the reduction quality of the data-cubes, being  $\sigma_{\text{noise}}$  the spread of the noise distribution. Since the noise in our data does not follow a Gaussian distribution and is not constant over the channel maps, we estimated the noise statistics by using only pixels with negative values, which instead are fairly distributed as Gaussian functions centered on zero. We calculated  $\sigma_{\text{noise}}$  by fitting Gaussian functions to the negative noise distribution and built the mask of regions with  $F > 1.5 - 2.5\sigma_{\text{noise}}$  channel by channel. Such a mask identifies the pixels that are considered as genuine galaxy emission by the <sup>3D</sup>BAROLO fitting algorithm. We do not fit the surface brightness of galaxies, but models are locally normalized to the integrated H $\alpha$  flux pixel-by-pixel (see Section 2.4.3).

Since the number of pixels that can be used to constrain the model is quite small in these high- $z$  data-cubes, we decided to keep the geometrical parameters fixed and fit only the rotation velocity and intrinsic velocity dispersion. The uncertainties on the geometrical parameters are however propagated in the errors on the rotation velocity and velocity dispersion. Errors on  $V_{\text{rot}}$  and  $\sigma_{\text{H}\alpha}$  were estimated by using a

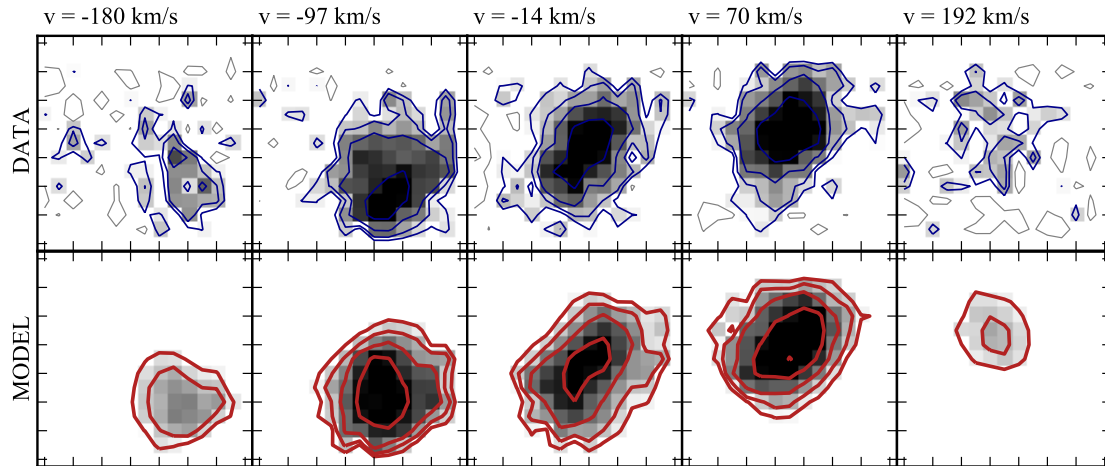


**Figure 5.2:** Comparison between the KMOS datacube (thin blue, upper panels) and the  $3^{\text{D}}$ BAROLO best model (thick red, lower panels) for the galaxy `zcos_z1_692` at  $z = 0.93$ . Negative contours are shown as thin grey lines in the data. We show five representative channel maps: the central panels represent the channel closest to the systemic velocity of the galaxy, the rightmost and the leftmost panels are the extreme velocities, the second and the fourth panels are at intermediate velocities. Boxes have sizes of about  $2'' \times 2''$  and the PSF is  $0.75''$ .

Monte-Carlo sampling of the full parameter space in the region close to the minimum as described in [Section 2.5.5](#).

### 5.3 Results

The comparison between our best 3D models and the data is shown in [Figure 5.3](#) through position-velocity slices (P-Vs) taken along the major axis. The models satisfactorily reproduce the data and, in particular, the last contours are well traced in most cases. These contours are very sensitive to the actual rotation velocities, testifying a well attained fit. The density asymmetries between the approaching and the receding sides in our models are due to the pixel-to-pixel normalization ([Section 2.4.3](#)). As an example, in [Figure 5.2](#) we show the comparison between the data-cube and the model cube in five channel maps at different velocities for the galaxy `zcos_z1_692`. Both in [Figure 5.2](#) and in [Figure 5.1](#), blue thin contours represent the data, red thick contours the models. [Figure 5.4](#) shows the derived rotation curves (*top panel*) and intrinsic velocity dispersions (*lower panel*) for the ten disk galaxies.

The rotation curves of all galaxies in our sample are remarkably flat from the first to the last measured point. We stress that, unlike previous kinematic studies at high-redshifts (e.g., Puech et al., 2008; Epinat et al., 2009; Swinbank et al., 2012; Bacon et al., 2015), we do not force the rotation curves to follow any functional form (e.g.,

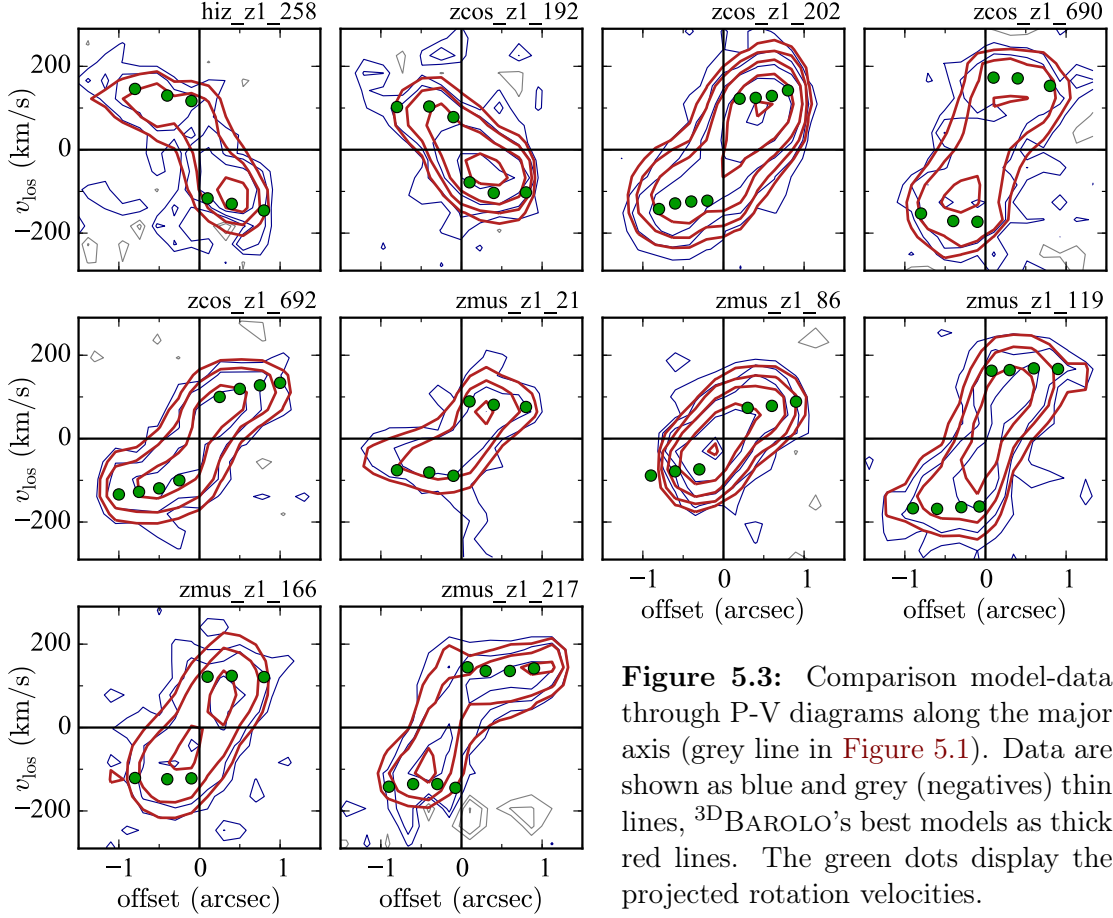


**Figure 5.3:** Comparison model-data through P-V diagrams along the major axis (grey line in [Figure 5.1](#)). Data are shown as blue and grey (negatives) thin lines, <sup>3D</sup>BAROLO's best models as thick red lines. The green dots display the projected rotation velocities.

$V_{\text{rot}}(R) \propto \arctan(R)$ , but at each radius the velocity is estimated independently. The inner velocity points of all galaxies are already in the flat part of the rotation curves, implying that the velocity rises very steeply in the inner kiloparsec. Overall, the shape of the rotation curves of these  $z \sim 1$  galaxies is akin to that of disks in the Local Universe with similar stellar mass (e.g., Casertano & van Gorkom, 1991). Similarly to local spiral galaxies, the dynamics of these high- $z$  systems is supposed to be dominated by the baryonic matter in the inner regions and by the dark matter halo in the outer regions. If, consistently with local disk galaxies, we assume a total gas component  $M_{\text{gas}} = M_{\text{HI}} + M_{\text{H}_2} \sim 0.2 - 0.3 M_*$  (e.g., Papastergis et al., 2012), the comparison between the total baryonic mass ( $M_* + M_{\text{gas}}$ ) and the dynamical mass  $M_{\text{dyn}} = R_{\text{last}} V_{\text{rot}}^2(R_{\text{last}})/G$  enclosed within the last measured radius  $R_{\text{last}} \sim 8$  kpc suggests that these galaxies must have dark matter fractions of 40%-60% of the total mass.

Despite our sample being small, it is interesting to place our galaxies on the stellar mass Tully-Fisher relation. We calculated the circular velocity  $V_{\text{flat}}$  of the flat part of the rotation curves as the average velocity over the rings, innermost point excluded. The resulting  $V_{\text{flat}}$  for each galaxy are listed in [Table 5.7](#), Column

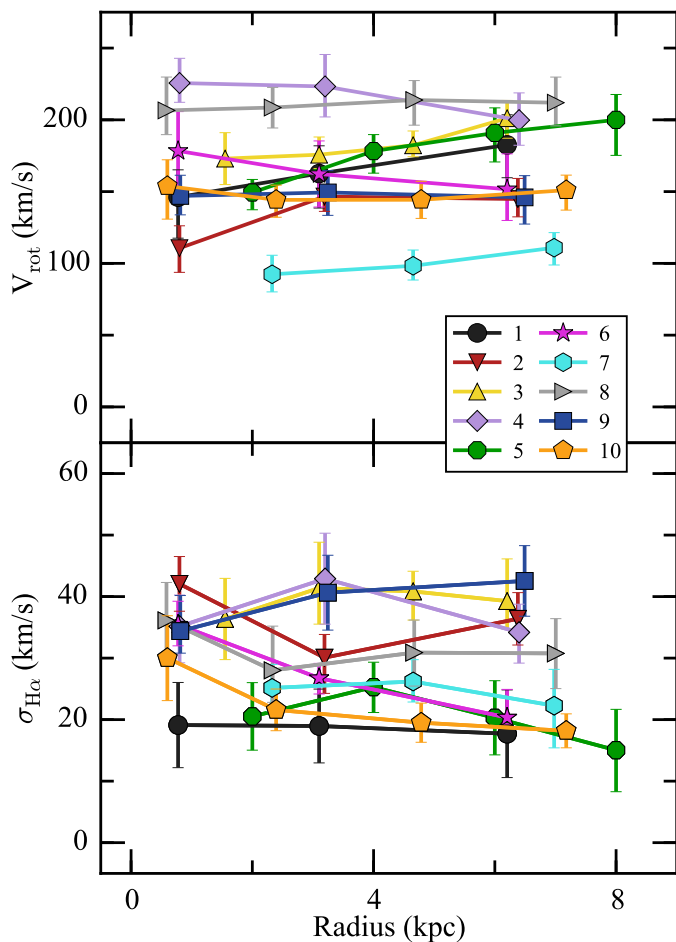


**Figure 5.4:** Rotation curves (*top*) and velocity dispersions (*bottom*) derived by fitting 3D tilted-ring models to H $\alpha$  datacubes of our galaxy sample with <sup>3D</sup>BAROLO. Galaxies are numbered as in Table 5.7. Radii are slightly oversampled (about 2 rings per resolution element). Rotation curves are remarkably flat from the first to the last point, velocity dispersion are lower than  $\sim 40 \text{ km s}^{-1}$ .

8. Stellar masses are taken from the COSMOS and 3D-HST catalogs and listed in Table 5.7, Column 6. Figure 5.5 shows the Tully-Fisher relation for our sample compared to previous studies. Our galaxies (full red circles) well overlap with the sample of Miller et al. (2011) in the redshift range  $0.6 < z < 1.1$  (cyan dots), derived from long-slit observations. For comparison, in Figure 5.5 we show also the best-fit for three Tully-Fisher relations: a local TFR (Reyes et al., 2011,  $z < 0.1$ ), a high- $z$  evolving relation (Puech et al., 2008,  $z \sim 0.6$ ) and a high- $z$  relation with no evolution (Miller et al., 2011,  $0.3 < z < 1.3$ ). A basic velocity-weighted  $\chi^2$  test on the Reyes et al. (2011) TFR lead to a  $\chi^2 = 5.6$  with respect to a  $\chi^2 = 18.6$  on the fit by Puech et al. (2008). Our datapoints seem therefore to support the idea of a not evolving or weakly evolving TFR relation (e.g., Miller et al., 2011, 2012) rather than an evolving relation (e.g., Kassin et al., 2007; Dutton et al., 2011), even if this latter can not be totally excluded with this small statistics.

Velocity dispersions (Figure 5.4, bottom panel) show no unique trend with radius, mainly because of the presence of clumpy regions of intense star formation in most galaxies, although the dispersion profiles appear roughly flat on average. The derived values of dispersions are between 15 and about  $40 \text{ km s}^{-1}$ , even in the regions

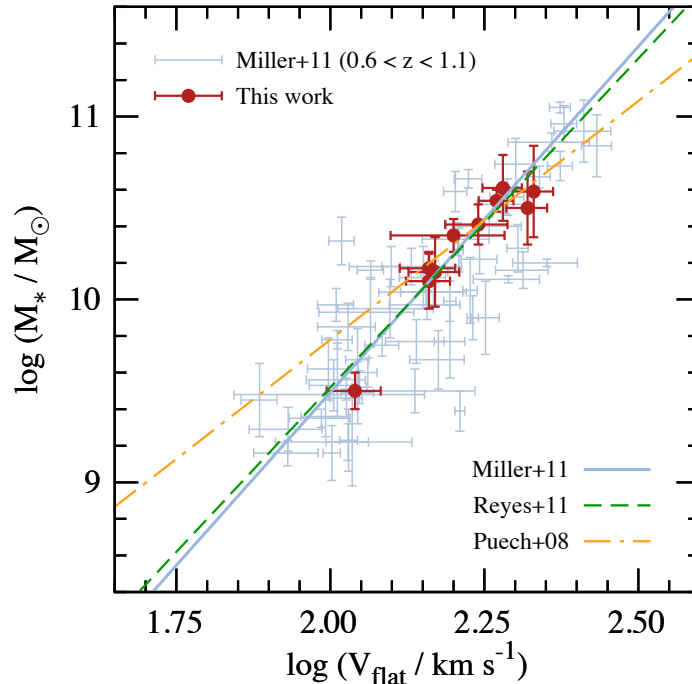


**Figure 5.5:** Tully-Fisher relation for our ten galaxies (red circles) compared to the sample by Miller et al. (2011) at  $0.6 < z < 1.1$  (cyan points). Lines are the fit of the relation  $\log(M_*) = a + b \log(V)$ . Green dashed line is the local TFR by Reyes et al. (2011) for  $z < 0.1$  ( $a = 2.39$ ,  $b = 3.59$ ), cyan solid line is the TFR by Miller et al. (2011) at  $0.3 < z < 1.3$  ( $a = 1.93$ ,  $b = 3.78$ ), yellow dash-dotted line is the TFR by Puech et al. (2008) at  $z \sim 0.6$  ( $a = 4.56$ ,  $b = 2.61$ ). Our points are compatible with no strong evolution of the relation.

close to the galaxy centers. These values are fully comparable to  $H\alpha$  velocity dispersions measured in disk galaxies in the Local Universe (e.g., Andersen et al., 2006; Bershady et al., 2010; Epinat et al., 2010). Note that they are much smaller than the line broadening showed in the velocity dispersion maps of Figure 5.1. Following Wisnioski et al. (2015), we show in Figure 5.6 the evolution with redshifts of velocity dispersion derived in previous kinematic studies of the warm medium. The plot includes both studies carried out with IFU observations, i.e. GHASP (Epinat et al., 2010), DYNAMO (Green et al., 2014), KMOS<sup>3D</sup> (Wisnioski et al., 2015), MASSIV (Epinat et al., 2012; Vergani et al., 2012), SINS/zC-SINF (Förster Schreiber et al., 2009), OSIRIS (Law et al., 2007, 2009) and AMAZE-LSD (Gnerucci et al., 2011) surveys, and with long slit observations, i.e. DEEP2 survey (Kassin et al., 2012). All the above-mentioned studies were based on the  $H\alpha$  emission line, but we stress that they used different instruments and different estimators to derive the gas velocity dispersion. The average velocity dispersions  $\langle \sigma_{H\alpha} \rangle$  derived in this work (Table 5.7, Column 9) for each galaxy are shown as large red circles. The dispersions derived by our 3D approach are similar to the results found in the recent paper by Wisnioski et al. (2015) (grey circles) in a larger sample of galaxies observed with KMOS, but

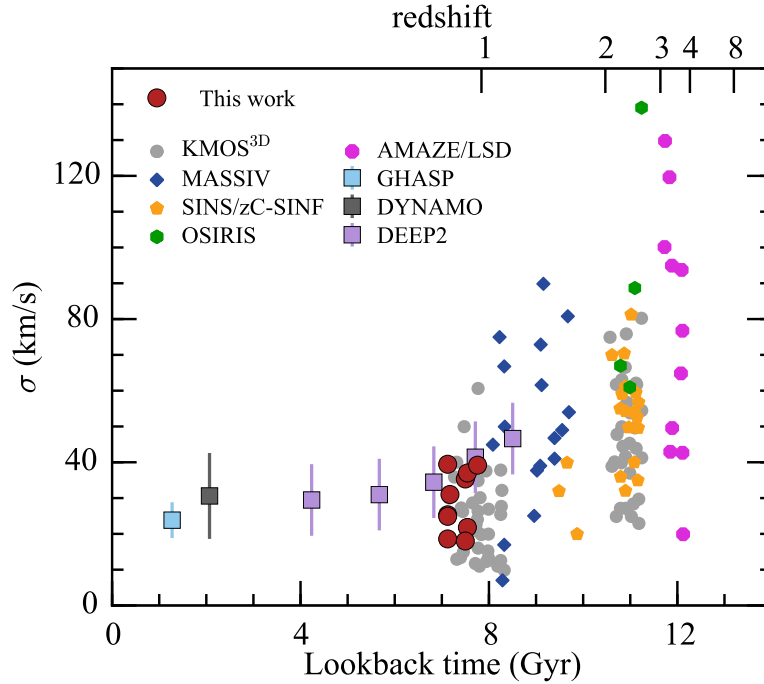


**Figure 5.6:** Evolution of gas velocity dispersion throughout cosmic time. Data are taken from different studies on star-forming galaxies observed in the surveys labelled in the legend. For  $z \lesssim 1$ , average values over large galaxy samples are shown as squares. Other symbols are measurements in single galaxies. The average velocity dispersion derived in this work are shown as red circles. Our values are comparable to those from the KMOSS<sup>3D</sup> survey (Wisnioski et al., 2015) and compatible with no evolution from  $z \sim 1$  to now.

overall smaller than the values quoted in the majority of previous works at similar redshifts (e.g., Epinat et al., 2012; Kassin et al., 2012). We stress however that the values quoted by Wisnioski et al. (2015) are measured from the outermost regions and along the major axis of the galaxies in the velocity dispersion maps, where the effect of beam smearing is supposed to be less significant (Förster Schreiber et al., 2009), while our values in Figure 5.6 are the average dispersions over the whole galaxy disks modeled in the 3D observational space. The average value over the whole sample is 30 km/s, showing that there has been hardly any evolution in the velocity dispersion in the last  $\sim 8$  Gyr. In other words, these disks were not more turbulent and/or dynamically hotter than the local ones. A possible explanation for these low velocity dispersions is that our galaxies have SFRs comparable to local galaxies, pointing at a relation between SFR and  $\sigma_{\text{H}\alpha}$ .

Finally, another important parameter is the  $V/\sigma$  ratio, which measures the relative importance of ordered ( $V$ ) and random ( $\sigma$ ) motions in the dynamical support of a galaxy. Systems in our sample have  $V/\sigma_{\text{H}\alpha}$  in the range 3 – 10, suggesting that these disks with normal SFRs are fully settled and rotational supported already at  $z \sim 1$ .

**Table 5.7:** The sample of ten disk galaxies at  $z \sim 1$  analyzed in this work: (1) Adopted name; (2) Identification number in COSMOS or 3D-HST catalogs; (3)-(4) Celestial coordinates in J2000; (5) Spectroscopic redshift; (6) Stellar masses from FAST fit (see text); (7) Star formation rates derived from integrated H $\alpha$  flux, probably lower limits; (8) Estimated inclination angle; (9) Velocity of the flat part of the rotation curve, defined as specified in [Section 5.3](#), derived in this work; (10) Intrinsic H $\alpha$  velocity dispersion averaged over the entire galaxy disk as derived in this work.

#	Name	ID	R.A. (J2000) h m s	Dec. (J2000) ° ' "	$z$	Log $M_*/M_\odot$	SFR $M_\odot \text{ yr}^{-1}$	$i$ °	$V_{\text{flat}}$ $\text{km s}^{-1}$	$\langle \sigma_{\text{H}\alpha} \rangle$ $\text{km s}^{-1}$
(1)	(2)	(3)	(4)	(5)	(6)	(7)	(8)	(9)	(10)	
1	hiz_z1_258	126376	10 01 05.65	+01 52 57.6	0.839	$10.41 \pm 0.11$	1.6	54	$173 \pm 20$	$19 \pm 7$
2	zcos_z1_192	126450	10 01 03.45	+01 54 00.4	0.917	$10.17 \pm 0.09$	5.3	45	$145 \pm 15$	$35 \pm 5$
3	zcos_z1_202	115789	10 00 53.39	+01 52 40.8	0.841	$10.54 \pm 0.06$	8.2	45	$185 \pm 12$	$39 \pm 6$
4	zcos_z1_690	3987 <sup>†</sup>	10 00 36.54	+02 13 09.5	0.927	$10.59 \pm 0.25$	3.0	50	$212 \pm 16$	$37 \pm 6$
5	zcos_z1_692	663 <sup>†</sup>	10 00 36.42	+02 11 19.2	0.930	$10.61 \pm 0.18$	6.4	42	$190 \pm 14$	$22 \pm 5$
6	zmus_z1_21	2723 <sup>†</sup>	03 32 48.48	-27 54 16.0	0.840	$10.35 \pm 0.09$	1.7	32	$157 \pm 24$	$27 \pm 4$
7	zmus_z1_86	13341 <sup>†</sup>	03 32 25.19	-27 51 00.1	0.841	$9.50 \pm 0.10$	3.9	51	$109 \pm 11$	$24 \pm 4$
8	zmus_z1_119	24457 <sup>†</sup>	03 32 08.20	-27 47 52.1	0.845	$10.50 \pm 0.20$	2.8	56	$212 \pm 16$	$31 \pm 6$
9	zmus_z1_166	35215 <sup>†</sup>	03 32 16.49	-27 44 49.1	0.975	$10.15 \pm 0.19$	4.2	59	$148 \pm 14$	$39 \pm 6$
10	zmus_z1_217	48285 <sup>†</sup>	03 32 20.51	-27 40 58.9	0.919	$10.10 \pm 0.15$	2.4	70	$146 \pm 12$	$22 \pm 4$

<sup>†</sup> Identification number from the 3D-HST survey.



# Chapter 6

---

## Concluding remarks and future prospects

### 6.1 Summary

The study of the dynamics of disk galaxies is a fundamental tool to understand their formation and evolution. Rotation curves in particular are very powerful to trace the distribution of luminous and dark matter and to infer the gravitational potential of galaxies. Rotation velocities also allow us to trace the distribution of angular momentum and to study fundamental scaling relations of disk galaxies, like the Tully-Fisher relation. On the other hand, velocity dispersions provide information on the “pressure” support due to turbulent/random motions, which can play an important part in the evolution and the stability of disks.

Spectroscopic observations of both stellar absorption lines and gas emission lines have been extensively used to investigate the kinematics of disk galaxies. In general, the relative importance of rotation and pressure supports can be easily derived from high spatial resolution observations. However, these two quantities become degenerate as the spatial resolution of the observations decreases (beam smearing).

In this thesis, we have presented a new method to derive the gas kinematics of disk galaxies from emission-line data-cubes. We have developed <sup>3D</sup>BAROLO ([Chapter 2](#)), a software to derive rotation curves that can be used with data at a wide range of spatial resolutions without being affected by instrumental biases. <sup>3D</sup>BAROLO sim-

ulates spectral data-cubes, starting from a tilted-ring model constructed in the 3D observational space and compares them with the actual 3D data. Since our algorithm does not go through the extraction of velocity fields, it is not affected by beam smearing like the traditional 2D techniques. The instrumental effects are included by convolving the models with the Point Spread Function before comparing them with the data. <sup>3D</sup>BAROLO can work with a variety of emission-line data. Suitable observations include the HI 21-cm line from radio-telescopes (e.g., VLA, WRST), CO and C<sup>+</sup> lines from sub-millimeter interferometers, such as the Plateau de Bure Interferometer or the Atacama Large Millimeter Array (ALMA), and optical/IR recombination lines from the last generation of Integral Field Units (e.g., KMOS and MUSE). In this thesis, we focused in particular on HI-line observations of nearby star-forming galaxies and H $\alpha$ -line KMOS observations of high- $z$  galaxies.

The main results of this work can be summarized as follows:

1) **3D vs 2D kinematic models.** *We showed that a 3D approach to the derivation of the gas kinematics of disk galaxies has to be preferred to a 2D approach whenever a galaxy is resolved with less than about 20 elements across the disk.* We run our 3D code, <sup>3D</sup>BAROLO, on several HI data-cubes of nearby galaxies at different spatial resolutions (Chapter 3). At high resolution, <sup>3D</sup>BAROLO performs as well as the traditional 2D approaches, but it is more computational expensive and it does not yet allow to study some kinematic peculiarities, such as non-circular motions. <sup>3D</sup>BAROLO reaches its best performance in deriving reliable rotation curves and velocity dispersions from mid-low resolution data (10-20 resolution elements), down to barely resolved galaxies (2-3 resolution elements), where the 2D approach completely fails because of the beam smearing effect. The possibility of identifying galaxies in a data-cube (source finder) and estimating the initial conditions for the fit makes <sup>3D</sup>BAROLO a tool that can be automatically run on large data-sets.

2) **Gas accretion from minor mergers.** *We showed that minor mergers can not significantly contribute to the gas accretion needed to sustain the star formation of spiral galaxies in the local Universe (Chapter 4).* We selected a sample of 148 spiral galaxies (WHISP catalog) and we used the 3D source-finding algorithm implemented in <sup>3D</sup>BAROLO to detect dwarf satellites around them. Assuming that all detected satellites will be accreted in the shortest possible time, we estimated a maximum accretion rate of  $0.28 M_{\odot} \text{ yr}^{-1}$ , which is about 20% of the total accretion required to sustain star formation in these galaxies. This value is a firm upper limit and the actual percentage is likely to be much lower. We conclude that dominant accretion processes other than minor merging must be advocated to explain the long-lasting star formation in spiral galaxies.

3) **Kinematics of high- $z$  disks.** *We showed that a population of disk galaxies dynamically similar to local disks already exists at redshift about 1.* We used <sup>3D</sup>BAROLO to analyze a small sample of normal star-forming galaxies at  $z = 0.85 - 1$  observed in the H $\alpha$  emission-line with the KMOS IFU (Chapter 5). The low spatial resolution of these observations makes them ideal cases to be studied with our code. The 3D modeling revealed that the kinematics of these high- $z$  systems is comparable to that of local disk galaxies, with steeply-rising rotation curves (within the inner kiloparsec) followed by a flat part and H $\alpha$  (turbulent motions) velocity dispersions  $\sigma_{\text{H}\alpha} \sim 15 - 40 \text{ km s}^{-1}$  over the whole disks. Baryonic matter contributes to nearly half the dynamical mass in the inner regions probed by our data. In addition, these galaxies appear to lie on the Tully-Fisher relation of local spiral galaxies. This suggest that disk galaxies were already fully settled and dynamically mature about 7-8 gigayears ago.

## 6.2 Outlook

<sup>3D</sup>BAROLO has currently reached a fulfilling degree of functionality and it is ready to be used with a large number of observations, taken both in the low and in the high redshift Universe. The code is publicly available to the community at <http://editeodoro.github.io/Bbarolo>. Nevertheless, the software is still actively been developed and new features will be implemented in the next future, including a mass-decomposition algorithm and a self-consistent treatment for the disk thickness using the hydrostatic equilibrium of the gas.

In this thesis we pointed out the need of a 3D approach to derive reliable kinematic quantities at low spatial resolutions. Most galaxies in the Universe are and will be in the future observed with just a handful of resolution elements, as the size of future telescopes can not indefinitely grow. The spatial resolution is and will be a serious limitation to the derivation of the kinematic properties of galaxies. Three-dimensional software, namely <sup>3D</sup>BAROLO, TiRiFiC and GalPak<sup>3D</sup>, are the best way to exploit the full information available in spectral data-cubes and break the degeneracy between the rotation velocity and the velocity dispersion.

At low redshifts, the most immediate field of application of <sup>3D</sup>BAROLO is the analysis of large galaxy samples from the upcoming HI surveys. To date, interferometric HI surveys, like WHISP, THINGS or VLA-ANGST, have observed a few hundred galaxies in the very local Universe. In the next decade, the upgrades of today radio-interferometers, like the new focal-plane array APERTIF on the WSRT and the new correlator on the EVLA, and the generation of future instruments, like ASKAP (2015-2016) and MeerKAT (2018), will guarantee high sensitivity together with much faster surveying times. A number of major HI surveys have been already approved, including low-deep (WALLABY and WNSHS, up to  $z_{\text{lim}} \sim 0.2$ ), medium-

deep (DINGO,  $z_{\text{lim}} \sim 0.5$ ) and ultra-deep (LADUMA,  $z_{\text{lim}} \sim 1.4$ ) projects. These surveys are expected to detect  $10^5 - 10^6$  galaxies at very low spatial resolution. The kinematic analysis of such a large number of galaxies will necessarily require three-dimensional and automatic approaches, both of which <sup>3D</sup>BAROLO can provide.

At high redshifts, the study of the gas kinematics is a flourishing field of research. The new generation of IFUs is providing a constantly increasing number of observations of high- $z$  galaxies up  $z \sim 4$  thanks to the detection of recombination lines, such as the  $\text{H}\alpha$ , N and O forbidden lines tracing the warm-hot gaseous component. Millimeter/submillimeter interferometers, in particular ALMA, can do even better and break the  $z \sim 4$  wall, thanks to the detection of CO and  $\text{C}^+$  lines from molecular and neutral gas, respectively. These instruments are providing the extraordinary opportunity to study the evolution of the kinematics and the dynamics of galaxies as a function of time. Many aspects of high- $z$  galaxies are still highly uncertain, such as the relative importance of rotation and pressure support ( $V/\sigma$ ), the actual role of gas turbulence, the stability of disks, the evolutionary path towards today galaxies. The analysis of large samples of galaxies at different redshifts with a software like <sup>3D</sup>BAROLO will enable us to separate physical and instrumental effects and provide new insights on how galaxies assemble and evolve throughout cosmic time.

# Bibliography

- Agertz O., Kravtsov A. V., Leitner S. N., Gnedin N. Y., 2013, *ApJ*, [770](#), [25](#)
- Agertz O., Teyssier R., Moore B., 2011, *MNRAS*, [410](#), [1391](#)
- Algorry D. G., Navarro J. F., Abadi M. G., Sales L. V., Steinmetz M., Piontek F., 2014, *MNRAS*, [437](#), [3596](#)
- Allen R. J., Goss W. M., van Woerden H., 1973, *A&A*, [29](#), [447](#)
- Andersen D. R., Bershadsky M. A., 2013, *ApJ*, [768](#), [41](#)
- Andersen D. R., Bershadsky M. A., Sparke L. S., Gallagher, III J. S., Wilcots E. M., van Driel W., Monnier-Ragaigne D., 2006, *ApJS*, [166](#), [505](#)
- Anderson M. E., Bregman J. N., 2010, *ApJ*, [714](#), [320](#)
- Argyle E., 1965, *ApJ*, [141](#), [750](#)
- Athanassoula E., Bosma A., Papaioannou S., 1987, *A&A*, [179](#), [23](#)
- Aumer M., Binney J. J., 2009, *MNRAS*, [397](#), [1286](#)
- Babcock H. W., 1939, *Lick. Obs. Bull.*, [19](#), [41](#)
- Bacon R. et al., 2010, in *Society of Photo-Optical Instrumentation Engineers (SPIE) Conference Series*, Vol. 7735, Society of Photo-Optical Instrumentation Engineers (SPIE) Conference Series, p. 8
- Bacon R. et al., 2015, *A&A*, [575](#), [A75](#)
- Bahcall J. N., Casertano S., 1985, *ApJL*, [293](#), [L7](#)
- Baldry I. K., Glazebrook K., Brinkmann J., Ivezić Ž., Lupton R. H., Nichol R. C., Szalay A. S., 2004, *ApJ*, [600](#), [681](#)
- Barbieri C. V., Fraternali F., Oosterloo T., Bertin G., Boomsma R., Sancisi R., 2005, *A&A*, [439](#), [947](#)
- Battaglia G., Fraternali F., Oosterloo T., Sancisi R., 2006, *A&A*, [447](#), [49](#)
- Begeman K. G., 1987, PhD thesis, Groningen Univ.
- Begeman K. G., 1989, *A&A*, [223](#), [47](#)
- Bell E. F., de Jong R. S., 2001, *ApJ*, [550](#), [212](#)
- Benson A. J., Bower R. G., Frenk C. S., Lacey C. G., Baugh C. M., Cole S., 2003, *ApJ*, [599](#), [38](#)

- Bershady M. A., Verheijen M. A. W., Swaters R. A., Andersen D. R., Westfall K. B., Martinsson T., 2010, *ApJ*, **716**, 198
- Bertone S., Conselice C. J., 2009, *MNRAS*, **396**, 2345
- Bigiel F. et al., 2011, *ApJL*, **730**, L13
- Binney J., 1977, *ApJ*, **215**, 483
- Binney J., 1978, *MNRAS*, **183**, 779
- Binney J., Merrifield M., 1998, *Galactic Astronomy*
- Birnboim Y., Dekel A., 2003, *MNRAS*, **345**, 349
- Blumenthal G. R., Faber S. M., Flores R., Primack J. R., 1986, *ApJ*, **301**, 27
- Blumenthal G. R., Faber S. M., Primack J. R., Rees M. J., 1984, *Nature*, **311**, 517
- Blumenthal G. R., Pagels H., Primack J. R., 1982, *Nature*, **299**, 37
- Bolatto A. D. et al., 2015, *ApJ*, **809**, 175
- Bond J. R., Cole S., Efstathiou G., Kaiser N., 1991, *ApJ*, **379**, 440
- Bond J. R., Szalay A. S., Turner M. S., 1982, *Physical Review Letters*, **48**, 1636
- Booth R. S., de Blok W. J. G., Jonas J. L., Fanaroff B., 2009, [ArXiv e-prints](#)
- Boselli A., Lequeux J., Gavazzi G., 2002, *A&A*, **384**, 33
- Bosma A., 1978, PhD thesis, Groningen Univ.
- Bottema R., 1993, *A&A*, **275**, 16
- Bouché N., Carfantan H., Schroetter I., Michel-Dansac L., Contini T., 2015, *AJ*, **150**, 92
- Bournaud F., Elmegreen B. G., Martig M., 2009, *ApJL*, **707**, L1
- Bower R., Bureau M., 2014, *The Messenger*, **157**, 38
- Brammer G. B. et al., 2012, *ApJS*, **200**, 13
- Bregman J. N., 2007, *ARA&A*, **45**, 221
- Briggs D. S., 1995, in *Bulletin of the American Astronomical Society*, Vol. 27, American Astronomical Society Meeting Abstracts, p. 112
- Bruzual G., Charlot S., 2003, *MNRAS*, **344**, 1000
- Bullock J. S., Kolatt T. S., Sigad Y., Somerville R. S., Kravtsov A. V., Klypin A. A., Primack J. R., Dekel A., 2001, *MNRAS*, **321**, 559
- Cappellari M. et al., 2011, *MNRAS*, **413**, 813
- Casertano S., van Gorkom J. H., 1991, *AJ*, **101**, 1231
- Chabrier G., 2003, *PASP*, **115**, 763
- Chiappini C., Matteucci F., Gratton R., 1997, *ApJ*, **477**, 765
- Chiba M., Beers T. C., 2000, *AJ*, **119**, 2843
- Chomiuk L., Povich M. S., 2011, *AJ*, **142**, 197

- Chynoweth K. M., Langston G. I., Holley-Bockelmann K., Lockman F. J., 2009, *AJ*, [138](#), [287](#)
- Comerón S. et al., 2011, *ApJ*, [741](#), [28](#)
- Conselice C. J., 2003, *ApJS*, [147](#), [1](#)
- Conselice C. J., Bundy K., Ellis R. S., Brichmann J., Vogt N. P., Phillips A. C., 2005, *ApJ*, [628](#), [160](#)
- Contini T. et al., 2012, *A&A*, [539](#), [A91](#)
- Corbelli E., Schneider S. E., 1997, *ApJ*, [479](#), [244](#)
- Corsini E. M., 2014, in *Astronomical Society of the Pacific Conference Series*, Vol. 486, *Multi-Spin Galaxies*, ASP Conference Series, Iodice E., Corsini E. M., eds., p. 51
- Cresci G. et al., 2009, *ApJ*, [697](#), [115](#)
- Dale J. E., 2015, *New A. Rev*, [68](#), [1](#)
- Davies R. et al., 2011, *ApJ*, [741](#), [69](#)
- Davies R. I. et al., 2013, *A&A*, [558](#), [A56](#)
- de Blok W. J. G. et al., 2014, *A&A*, [569](#), [A68](#)
- de Blok W. J. G., Walter F., Brinks E., Trachternach C., Oh S.-H., Kennicutt, Jr. R. C., 2008, *AJ*, [136](#), [2648](#)
- De Propris R., Conselice C. J., Liske J., Driver S. P., Patton D. R., Graham A. W., Allen P. D., 2007, *ApJ*, [666](#), [212](#)
- de Ravel L. et al., 2009, *A&A*, [498](#), [379](#)
- Dekel A., Birnboim Y., 2006, *MNRAS*, [368](#), [2](#)
- Dekel A., Sari R., Ceverino D., 2009, *ApJ*, [703](#), [785](#)
- Dib S., Bell E., Burkert A., 2006, *ApJ*, [638](#), [797](#)
- Dutton A. A., Conroy C., van den Bosch F. C., Prada F., More S., 2010, *MNRAS*, [407](#), [2](#)
- Dutton A. A., van den Bosch F. C., Dekel A., 2010, *MNRAS*, [405](#), [1690](#)
- Dutton A. A. et al., 2011, *MNRAS*, [410](#), [1660](#)
- Dziourkevitch N., Elstner D., Rüdiger G., 2004, *A&A*, [423](#), [L29](#)
- Einasto J., Saar E., Kaasik A., Chernin A. D., 1974, *Nature*, [252](#), [111](#)
- Eisenhauer F. et al., 2003, in *Society of Photo-Optical Instrumentation Engineers (SPIE) Conference Series*, Vol. 4841, *Instrument Design and Performance for Optical/Infrared Ground-based Telescopes*, Iye M., Moorwood A. F. M., eds., pp. 1548–1561
- Elbaz D. et al., 2011, *A&A*, [533](#), [A119](#)
- Elmegreen B. G., Elmegreen D. M., Leitner S. N., 2003, *ApJ*, [590](#), [271](#)

- Emsellem E. et al., 2004, MNRAS, [352](#), [721](#)
- Epinat B., Amram P., Balkowski C., Marcelin M., 2010, MNRAS, [401](#), [2113](#)
- Epinat B. et al., 2009, A&A, [504](#), [789](#)
- Epinat B. et al., 2012, A&A, [539](#), [A92](#)
- Ewen H. I., Purcell E. M., 1951, Nature, [168](#), [356](#)
- Fabian A. C., 2012, ARA&A, [50](#), [455](#)
- Fall S. M., Efstathiou G., 1980, MNRAS, [193](#), [189](#)
- Feng J. Q., Gallo C. F., 2011, Research in Astronomy and Astrophysics, [11](#), [1429](#)
- Fernández X., Joungh M. R., Putman M. E., 2012, ApJ, [749](#), [181](#)
- Firmani C., Avila-Reese V., 2000, MNRAS, [315](#), [457](#)
- Flores H., Hammer F., Puech M., Amram P., Balkowski C., 2006, A&A, [455](#), [107](#)
- Fomalont E., 1981, National Radio Astronomy Observatory Newsletter, [3](#), [3](#)
- Förster Schreiber N. M. et al., 2009, ApJ, [706](#), [1364](#)
- Förster Schreiber N. M. et al., 2006, ApJ, [645](#), [1062](#)
- Franx M., de Zeeuw T., 1992, ApJL, [392](#), [L47](#)
- Franx M., van Gorkom J. H., de Zeeuw T., 1994, ApJ, [436](#), [642](#)
- Fraternali F., Oosterloo T., Sancisi R., van Moorsel G., 2001, ApJL, [562](#), [L47](#)
- Fraternali F., Tomassetti M., 2012, MNRAS, [426](#), [2166](#)
- Fraternali F., van Moorsel G., Sancisi R., Oosterloo T., 2002, AJ, [123](#), [3124](#)
- Freeman K. C., 1970, ApJ, [160](#), [811](#)
- Gatto A., Fraternali F., Read J. I., Marinacci F., Lux H., Walch S., 2013, MNRAS, [433](#), [2749](#)
- Gentile G., Fraternali F., Klein U., Salucci P., 2003, A&A, [405](#), [969](#)
- Gentile G. et al., 2013, A&A, [554](#), [A125](#)
- Gentile G., Salucci P., Klein U., Vergani D., Kalberla P., 2004, MNRAS, [351](#), [903](#)
- Genzel R. et al., 2008, ApJ, [687](#), [59](#)
- Genzel R. et al., 2014, ApJ, [785](#), [75](#)
- Genzel R. et al., 2006, Nature, [442](#), [786](#)
- Giovanelli R. et al., 2007, AJ, [133](#), [2569](#)
- Glazebrook K., 2013, PASA, [30](#), [56](#)
- Gnerucci A. et al., 2011, A&A, [528](#), [A88](#)
- Governato F., Willman B., Mayer L., Brooks A., Stinson G., Valenzuela O., Wadsley J., Quinn T., 2007, MNRAS, [374](#), [1479](#)
- Grcevich J., Putman M. E., 2009, ApJ, [696](#), [385](#)
- Green A. W. et al., 2010, Nature, [467](#), [684](#)

- Green A. W. et al., 2014, MNRAS, [437](#), [1070](#)
- Grogin N. A. et al., 2011, ApJS, [197](#), [35](#)
- Heald G. et al., 2011, A&A, [526](#), [A118](#)
- Helou G., Soifer B. T., Rowan-Robinson M., 1985, ApJL, [298](#), [L7](#)
- Hennebelle P., Audit E., 2007, A&A, [465](#), [431](#)
- Holwerda B. W., Pirzkal N., de Blok W. J. G., Bouchard A., Blyth S.-L., van der Heyden K. J., 2011, MNRAS, [416](#), [2437](#)
- Hopkins A. M., McClure-Griffiths N. M., Gaensler B. M., 2008, ApJL, [682](#), [L13](#)
- Hopkins P. F. et al., 2010, ApJ, [724](#), [915](#)
- Hopkins P. F., Kereš D., Oñorbe J., Faucher-Giguère C.-A., Quataert E., Murray N., Bullock J. S., 2014, MNRAS, [445](#), [581](#)
- Huchra J. P. et al., 2012, ApJS, [199](#), [26](#)
- Jogee S. et al., 2009, ApJ, [697](#), [1971](#)
- Johnston S. et al., 2008, Experimental Astronomy, [22](#), [151](#)
- Joung M. K. R., Mac Low M.-M., 2006, ApJ, [653](#), [1266](#)
- Józsa G. I. G., Kenn F., Klein U., Oosterloo T. A., 2007, A&A, [468](#), [731](#)
- Józsa G. I. G., Oosterloo T. A., Morganti R., Klein U., Erben T., 2009, A&A, [494](#), [489](#)
- Kalnajs A. J., 1983, in IAU Symposium, Vol. 100, Internal Kinematics and Dynamics of Galaxies, Athanassoula E., ed., pp. 109–115
- Kamphuis P., Józsa G. I. G., Oh S.-H., Spekkens K., Urbancic N., Serra P., Koribalski B. S., Dettmar R.-J., 2015, MNRAS, [452](#), [3139](#)
- Kamphuis P. et al., 2013, MNRAS, [434](#), [2069](#)
- Kassin S. A. et al., 2012, ApJ, [758](#), [106](#)
- Kassin S. A. et al., 2007, ApJL, [660](#), [L35](#)
- Kay S. T., Pearce F. R., Jenkins A., Frenk C. S., White S. D. M., Thomas P. A., Couchman H. M. P., 2000, MNRAS, [316](#), [374](#)
- Kazantzidis S., Zentner A. R., Kravtsov A. V., Bullock J. S., Debattista V. P., 2009, ApJ, [700](#), [1896](#)
- Kennicutt R. C., Evans N. J., 2012, ARA&A, [50](#), [531](#)
- Kennicutt, Jr. R. C., 1998, ApJ, [498](#), [541](#)
- Kent S. M., 1986, AJ, [91](#), [1301](#)
- Kereš D., Katz N., Fardal M., Davé R., Weinberg D. H., 2009, MNRAS, [395](#), [160](#)
- Kereš D., Katz N., Weinberg D. H., Davé R., 2005, MNRAS, [363](#), [2](#)
- Kriek M., van Dokkum P. G., Labbé I., Franx M., Illingworth G. D., Marchesini D., Quadri R. F., 2009, ApJ, [700](#), [221](#)

- Kroupa P., 2002, *Science*, [295](#), [82](#)
- Kuzio de Naray R., McGaugh S. S., de Blok W. J. G., 2008, *ApJ*, [676](#), [920](#)
- Lacey C., Cole S., 1993, *MNRAS*, [262](#), [627](#)
- Lagache G., Puget J.-L., Dole H., 2005, *ARA&A*, [43](#), [727](#)
- Lambas D. G., Alonso S., Mesa V., O'Mill A. L., 2012, *A&A*, [539](#), [A45](#)
- Larkin J. et al., 2006, in *Society of Photo-Optical Instrumentation Engineers (SPIE) Conference Series*, Vol. 6269, Society of Photo-Optical Instrumentation Engineers (SPIE) Conference Series, p. 1
- Law D. R., Steidel C. C., Erb D. K., Larkin J. E., Pettini M., Shapley A. E., Wright S. A., 2007, *ApJ*, [669](#), [929](#)
- Law D. R., Steidel C. C., Erb D. K., Larkin J. E., Pettini M., Shapley A. E., Wright S. A., 2009, *ApJ*, [697](#), [2057](#)
- Le Fèvre O. et al., 2000, *MNRAS*, [311](#), [565](#)
- Lehner N. et al., 2013, *ApJ*, [770](#), [138](#)
- Leitner S. N., Kravtsov A. V., 2011, *ApJ*, [734](#), [48](#)
- Lelli F., Fraternali F., Sancisi R., 2010, *A&A*, [516](#), [A11](#)
- Lelli F., Verheijen M., Fraternali F., Sancisi R., 2012, *A&A*, [537](#), [A72](#)
- Levenberg K., 1944, *Quart. Appl. Math.*, [2](#), 164
- Lilly S. J., Carollo C. M., Pipino A., Renzini A., Peng Y., 2013, *ApJ*, [772](#), [119](#)
- Lin L. et al., 2008, *ApJ*, [681](#), [232](#)
- Longhetti M., Saracco P., 2009, *MNRAS*, [394](#), [774](#)
- López-Sanjuan C., Balcells M., Pérez-González P. G., Barro G., García-Dabó C. E., Gallego J., Zamorano J., 2009, *A&A*, [501](#), [505](#)
- Lotz J. M. et al., 2008, *ApJ*, [672](#), [177](#)
- Lotz J. M., Primack J., Madau P., 2004, *AJ*, [128](#), [163](#)
- Lovelace R. V. E., 1998, *A&A*, [338](#), [819](#)
- Ludlow A. D., Navarro J. F., Angulo R. E., Boylan-Kolchin M., Springel V., Frenk C., White S. D. M., 2014, *MNRAS*, [441](#), [378](#)
- Lutz R. K., 1980, *The Computer Journal*, [23](#), [262](#)
- Mannheim P. D., Kazanas D., 1989, *ApJ*, [342](#), [635](#)
- Marinacci F., Binney J., Fraternali F., Nipoti C., Ciotti L., Londrillo P., 2010, *MNRAS*, [404](#), [1464](#)
- Marinacci F., Pakmor R., Springel V., 2014, *MNRAS*, [437](#), [1750](#)
- Marquardt D., 1963, *SIAM J. Appl. Math.*, [11](#), 431
- Martin A. M., Papastergis E., Giovanelli R., Haynes M. P., Springob C. M., Stierwalt S., 2010, *ApJ*, [723](#), [1359](#)

- Martin D. C. et al., 2007, *ApJS*, **173**, 342
- Martinsson T. P. K., Verheijen M. A. W., Westfall K. B., Bershady M. A., Schechtman-Rook A., Andersen D. R., Swaters R. A., 2013, *A&A*, **557**, A130
- Mayall N. U., Aller L. H., 1942, *ApJ*, **95**, 5
- McGaugh S. S., 2005, *ApJ*, **632**, 859
- McGaugh S. S., 2012, *AJ*, **143**, 40
- McGaugh S. S., Schombert J. M., Bothun G. D., de Blok W. J. G., 2000, *ApJL*, **533**, L99
- Meurer G. R., Carignan C., Beaulieu S. F., Freeman K. C., 1996, *AJ*, **111**, 1551
- Meyer M. J., Zwaan M. A., Webster R. L., Schneider S., Staveley-Smith L., 2008, *MNRAS*, **391**, 1712
- Mihos J. C., Richstone D. O., Bothun G. D., 1992, *ApJ*, **400**, 153
- Milgrom M., 1983, *ApJ*, **270**, 365
- Miller S. H., Bundy K., Sullivan M., Ellis R. S., Treu T., 2011, *ApJ*, **741**, 115
- Miller S. H., Ellis R. S., Sullivan M., Bundy K., Newman A. B., Treu T., 2012, *ApJ*, **753**, 74
- Mo H. J., Mao S., White S. D. M., 1998, *MNRAS*, **295**, 319
- Moffat J. W., 2006, *JCAP*, **3**, 4
- Naab T., Ostriker J. P., 2006, *MNRAS*, **366**, 899
- Navarro J. F., Frenk C. S., White S. D. M., 1996, *ApJ*, **462**, 563
- Navarro J. F., Frenk C. S., White S. D. M., 1997, *ApJ*, **490**, 493
- Nelder J. A., Mead R., 1965, *The Computer Journal*, **7**, 308
- Nelson D., Genel S., Vogelsberger M., Springel V., Sijacki D., Torrey P., Hernquist L., 2015, *MNRAS*, **448**, 59
- Newman S. F. et al., 2013, *ApJ*, **767**, 104
- Nilson P., 1973, *Uppsala general catalogue of galaxies*
- Noeske K. G. et al., 2007, *ApJL*, **660**, L47
- Noordermeer E., van der Hulst J. M., Sancisi R., Swaters R. A., van Albada T. S., 2005, *A&A*, **442**, 137
- Ocvirk P., Pichon C., Teyssier R., 2008, *MNRAS*, **390**, 1326
- Oh S.-H., de Blok W. J. G., Walter F., Brinks E., Kennicutt, Jr. R. C., 2008, *AJ*, **136**, 2761
- Oort J. H., 1932, *Bull. Astron. Inst. Netherlands*, **6**, 249
- Oort J. H., 1940, *ApJ*, **91**, 273
- Ostriker J. P., Peebles P. J. E., 1973, *ApJ*, **186**, 467
- Ott J. et al., 2012, *AJ*, **144**, 123

- Palunas P., Williams T. B., 2000, *AJ*, [120](#), [2884](#)
- Panter B., Jimenez R., Heavens A. F., Charlot S., 2007, *MNRAS*, [378](#), [1550](#)
- Papastergis E., Cattaneo A., Huang S., Giovanelli R., Haynes M. P., 2012, *ApJ*, [759](#), [138](#)
- Park O.-K., Staveley-Smith L., Koribalski B., Kalnajs A., Freeman K. C., Malin D., 2001, in *Astronomical Society of the Pacific Conference Series*, Vol. 240, *Gas and Galaxy Evolution*, Hibbard J. E., Rupen M., van Gorkom J. H., eds., p. 863
- Patton D. R., Carlberg R. G., Marzke R. O., Pritchett C. J., da Costa L. N., Pellegrini P. S., 2000, *ApJ*, [536](#), [153](#)
- Pease F. G., 1918, *Proc. Natl. Acad. Sci. U.S.A.*, [4](#), 21
- Peebles P. J. E., 1982, *ApJL*, [263](#), [L1](#)
- Perlmutter S. et al., 1999, *ApJ*, [517](#), [565](#)
- Piffi T. et al., 2014, *A&A*, [562](#), [A91](#)
- Pisano D. J., Barnes D. G., Gibson B. K., Staveley-Smith L., Freeman K. C., Kilborn V. A., 2007, *ApJ*, [662](#), [959](#)
- Pisano D. J., Barnes D. G., Staveley-Smith L., Gibson B. K., Kilborn V. A., Freeman K. C., 2011, *ApJS*, [197](#), [28](#)
- Pizagno J. et al., 2005, *ApJ*, [633](#), [844](#)
- Planck Collaboration et al., 2014, *A&A*, [571](#), [A16](#)
- Portinari L., Sommer-Larsen J., 2007, *MNRAS*, [375](#), [913](#)
- Portinari L., Sommer-Larsen J., Tantalo R., 2004, *MNRAS*, [347](#), [691](#)
- Press W. H., Teukolsky S. A., Vetterling W. T., Flannery B. P., 2007, *Numerical recipes in C++ : the art of scientific computing*. Cambridge University Press
- Prochaska J. X., Wolfe A. M., 2009, *ApJ*, [696](#), [1543](#)
- Pryke C., Halverson N. W., Leitch E. M., Kovac J., Carlstrom J. E., Holzzapfel W. L., Dragovan M., 2002, *ApJ*, [568](#), [46](#)
- Puech M. et al., 2008, *A&A*, [484](#), [173](#)
- Putman M. E., Peek J. E. G., Joung M. R., 2012, *ARA&A*, [50](#), [491](#)
- Rees M. J., Ostriker J. P., 1977, *MNRAS*, [179](#), [541](#)
- Reyes R., Mandelbaum R., Gunn J. E., Pizagno J., Lackner C. N., 2011, *MNRAS*, [417](#), [2347](#)
- Riess A. G. et al., 1998, *AJ*, [116](#), [1009](#)
- Roberts M. S., 1975, *Radio Observations of Neutral Hydrogen in Galaxies*, Sandage A., Sandage M., Kristian J., eds., the University of Chicago Press, p. 309
- Robotham A. S. G. et al., 2012, *MNRAS*, [424](#), [1448](#)
- Rodighiero G. et al., 2011, *ApJL*, [739](#), [L40](#)

- Rogstad D. H., Lockhart I. A., Wright M. C. H., 1974, *ApJ*, **193**, 309
- Rogstad D. H., Shostak G. S., 1971, *A&A*, **13**, 99
- Rogstad D. H., Shostak G. S., 1972, *ApJ*, **176**, 315
- Rubin V. C., Thonnard N., Ford, Jr. W. K., 1978, *ApJL*, **225**, L107
- Sakai S. et al., 2000, *ApJ*, **529**, 698
- Sancisi R., Fraternali F., Oosterloo T., van der Hulst T., 2008, *ARA&A*, **15**, 189
- Sancisi R., Fraternali F., Oosterloo T., van Moorsel G., 2001, in *Astronomical Society of the Pacific Conference Series*, Vol. 230, *Galaxy Disks and Disk Galaxies*, Funes J. G., Corsini E. M., eds., pp. 111–118
- Santos-Santos I. M., Brook C. B., Stinson G., Di Cintio A., Wadsley J., Domínguez-Tenreiro R., Gottlöber S., Yepes G., 2015, [ArXiv e-prints](#)
- Schaye J. et al., 2015, *MNRAS*, **446**, 521
- Schmidt P., Józsa G. I. G., Gentile G., Oh S.-H., Schuberth Y., Ben Bekhti N., Winkel B., Klein U., 2014, *A&A*, **561**, A28
- Schoenmakers R. H. M., 1999, PhD thesis, University of Groningen
- Schoenmakers R. H. M., Franx M., de Zeeuw P. T., 1997, *MNRAS*, **292**, 349
- Schweizer F., 1982, *ApJ*, **252**, 455
- Schweizer F., 1998, in *Saas-Fee Advanced Course 26: Galaxies: Interactions and Induced Star Formation*, Kennicutt Jr. R. C., Schweizer F., Barnes J. E., Friedli D., Martinet L., Pfenniger D., eds., p. 105
- Sellwood J. A., Sánchez R. Z., 2010, *MNRAS*, **404**, 1733
- Sharples R. et al., 2013, *The Messenger*, **151**, 21
- Sharples R. M., Ramsay S. K., Davies R., Lehnert M., 2008, in *2007 ESO Instrument Calibration Workshop*, Kaufer A., Kerber F., eds., p. 311
- Shields G. A., 1990, *ARA&A*, **28**, 525
- Shull J. M., Jones J. R., Danforth C. W., Collins J. A., 2009, *ApJ*, **699**, 754
- Shull J. M., Smith B. D., Danforth C. W., 2012, *ApJ*, **759**, 23
- Sicking F. J., 1997, PhD thesis, Groningen Univ.
- Silk J., 1977, *A&A*, **59**, 53
- Simon J. D., Bolatto A. D., Leroy A., Blitz L., 2003, *ApJ*, **596**, 957
- Skelton R. E. et al., 2014, *ApJS*, **214**, 24
- Slipher V. M., 1914, *Lowell Obs. Bull.* II, 12
- Sofue Y., Rubin V., 2001, *ARA&A*, **39**, 137
- Speagle J. S., Steinhardt C. L., Capak P. L., Silverman J. D., 2014, *ApJS*, **214**, 15
- Spekkens K., Sellwood J. A., 2007, *ApJ*, **664**, 204
- Stewart K. R., Bullock J. S., Wechsler R. H., Maller A. H., 2009, *ApJ*, **702**, 307

- Stinson G. S. et al., 2013, MNRAS, [436](#), [625](#)
- Strateva I. et al., 2001, AJ, [122](#), [1861](#)
- Swaters R. A., 1999, PhD thesis, Groningen Univ.
- Swinbank A. M., Sobral D., Smail I., Geach J. E., Best P. N., McCarthy I. G., Crain R. A., Theuns T., 2012, MNRAS, [426](#), [935](#)
- Tacchella S. et al., 2015, ApJ, [802](#), [101](#)
- Tacconi L. J. et al., 2010, Nature, [463](#), [781](#)
- Tacconi L. J. et al., 2013, ApJ, [768](#), [74](#)
- Tamburro D., Rix H.-W., Leroy A. K., Mac Low M.-M., Walter F., Kennicutt R. C., Brinks E., de Blok W. J. G., 2009, AJ, [137](#), [4424](#)
- Taylor C. L., Kobulnicky H. A., Skillman E. D., 1998, AJ, [116](#), [2746](#)
- Teuben P., 1995, in Astronomical Society of the Pacific Conference Series, Vol. 77, Astronomical Data Analysis Software and Systems IV, Shaw R. A., Payne H. E., Hayes J. J. E., eds., p. 398
- Toomre A., Toomre J., 1972, ApJ, [178](#), [623](#)
- Tully R. B. et al., 2013, AJ, [146](#), [86](#)
- Tully R. B., Fisher J. R., 1977, A&A, [54](#), [661](#)
- Tully R. B., Rizzi L., Shaya E. J., Courtois H. M., Makarov D. I., Jacobs B. A., 2009, AJ, [138](#), [323](#)
- Tumlinson J. et al., 2013, ApJ, [777](#), [59](#)
- van Albada T. S., Bahcall J. N., Begeman K., Sancisi R., 1985, ApJ, [295](#), [305](#)
- van Albada T. S., Sancisi R., 1986, Philosophical Transactions of the Royal Society of London Series A, [320](#), [447](#)
- van de Hulst H. C., Raimond E., van Woerden H., 1957, BAN, [14](#), [1](#)
- van den Bosch F. C., 2000, ApJ, [530](#), [177](#)
- van der Hulst J. M., Terlouw J. P., Begeman K. G., Zwitter W., Roelfsema P. R., 1992, in Astronomical Society of the Pacific Conference Series, Vol. 25, Astronomical Data Analysis Software and Systems I, Worrall D. M., Biemesderfer C., Barnes J., eds., p. 131
- van der Hulst J. M., van Albada T. S., Sancisi R., 2001, in Astronomical Society of the Pacific Conference Series, Vol. 240, Gas and Galaxy Evolution, Hibbard J. E., Rupen M., van Gorkom J. H., eds., p. 451
- van der Kruit P. C., Freeman K. C., 2011, ARA&A, [49](#), [301](#)
- van der Kruit P. C., Shostak G. S., 1982, A&A, [105](#), [351](#)
- van der Marel R. P., Franx M., 1993, ApJ, [407](#), [525](#)
- van Eymeren J., Trachternach C., Koribalski B. S., Dettmar R.-J., 2009, A&A, [505](#),

## 1

- van Zee L., Bryant J., 1999, *AJ*, **118**, 2172
- Vergani D. et al., 2012, *A&A*, **546**, A118
- Verheijen M. A. W., 1997, PhD thesis, Groningen Univ.
- Verheijen M. A. W., 2001, *ApJ*, **563**, 694
- Verheijen M. A. W., Oosterloo T. A., van Cappellen W. A., Bakker L., Ivashina M. V., van der Hulst J. M., 2008, in American Institute of Physics Conference Series, Vol. 1035, *The Evolution of Galaxies Through the Neutral Hydrogen Window*, Minchin R., Momjian E., eds., pp. 265–271
- Wakker B. P. et al., 2007, *ApJL*, **670**, L113
- Walker T. P., Steigman G., Kang H.-S., Schramm D. M., Olive K. A., 1991, *ApJ*, **376**, 51
- Walter F., Brinks E., de Blok W. J. G., Bigiel F., Kennicutt, Jr. R. C., Thornley M. D., Leroy A., 2008, *AJ*, **136**, 2563
- Weiner B. J. et al., 2006, *ApJ*, **653**, 1049
- Whitaker K. E., van Dokkum P. G., Brammer G., Franx M., 2012, *ApJL*, **754**, L29
- White S. D. M., Rees M. J., 1978, *MNRAS*, **183**, 341
- Whiting M. T., 2012, *MNRAS*, **421**, 3242
- Wilson C. D. et al., 2011, *MNRAS*, **410**, 1409
- Winkel B., Flöer L., Kraus A., 2012, *A&A*, **547**, A119
- Winkel B., Kraus A., Bach U., 2012, *A&A*, **540**, A140
- Wisnioski E. et al., 2015, *ApJ*, **799**, 209
- Wolf M., 1914, *Vierteljahresschrift Astron. Gesell.*, **49**, 162
- Wyder T. K. et al., 2007, *ApJS*, **173**, 293
- Young J. S., Scoville N. Z., 1991, *ARA&A*, **29**, 581
- Zaritsky D. et al., 2014, *AJ*, **147**, 134
- Zschaechner L. K., Rand R. J., Heald G. H., Gentile G., Józsa G., 2012, *ApJ*, **760**, 37
- Zwaan M. A., Meyer M. J., Staveley-Smith L., Webster R. L., 2005, *MNRAS*, **359**, L30
- Zwicky F., 1933, *Helvetica Physica Acta*, **6**, 110



# List of Figures and Tables

<b>Chapter 1: Introduction</b>	<b>1</b>
<i>Fig. 1.1</i> First rotation curve of the Andromeda galaxy (Pease, 1918) . . .	2
<i>Fig. 1.2</i> Andromeda galaxy (M31) at different wavelengths . . . . .	3
<i>Fig. 1.3</i> Examples of rotation curves of HSB (Sofue & Rubin, 2001) and LSB (Swaters, 1999) galaxies . . . . .	5
<i>Fig. 1.4</i> Comparison between high- $z$ and low- $z$ disks (Glazebrook, 2013)	8
<i>Fig. 1.5</i> Rotation curve decompositions for NGC 3198 and DDO 154 (de Blok et al., 2008) . . . . .	12
<i>Fig. 1.6</i> Stellar mass and Baryonic Tully-Fisher relations (McGaugh, 2005) . . . . .	14
<i>Fig. 1.7</i> Gas accretion in cosmological simulations (Kereš et al., 2009) .	18
<b>Chapter 2: <sup>3D</sup>BAROLO: a software for galaxy kinematics</b>	<b>21</b>
<i>Fig. 2.1</i> HI data-cube for the spiral galaxy NGC 4559 . . . . .	23
<i>Fig. 2.2</i> Moment maps and P-V diagram for NGC 4559 . . . . .	24
<i>Fig. 2.3</i> Tilted-ring model for M83 (Rogstad, Lockhart & Wright, 1974)	26
<i>Fig. 2.4</i> Beam smearing effect (Epinat et al., 2010) . . . . .	31
<i>Fig. 2.5</i> <sup>3D</sup> BAROLO: flowchart of the main algorithm . . . . .	33
<i>Fig. 2.6</i> <sup>3D</sup> BAROLO: 3D geometry of the tilted-ring model . . . . .	35
<i>Fig. 2.7</i> <sup>3D</sup> BAROLO: error estimate . . . . .	43
<i>Fig. 2.8</i> <sup>3D</sup> BAROLO: Graphical User Interface (GUI) . . . . .	44
<b>Chapter 3: HI kinematics of local galaxies</b>	<b>47</b>
<i>Fig. 3.1</i> High-resolution <sup>3D</sup> BAROLO's model for NGC 2403 (THINGS) .	51
<i>Fig. 3.2</i> High-resolution <sup>3D</sup> BAROLO's model for NGC 2903 (THINGS) .	52
<i>Fig. 3.3</i> High-resolution <sup>3D</sup> BAROLO's model for NGC 3198 (THINGS) .	53
<i>Fig. 3.4</i> High-resolution <sup>3D</sup> BAROLO's model for NGC 5055 (THINGS) .	54

<i>Fig. 3.5</i>	P-V diagrams of 30 dwarf late-type galaxies (WHISP) . . . . .	56
<i>Fig. 3.6</i>	Rotation curves of 30 dwarf late-type galaxies (WHISP) . . . . .	60
<i>Fig. 3.7</i>	Velocity fields and velocity dispersion maps at high and low resolutions for NGC 2403 . . . . .	62
<i>Fig. 3.8</i>	Single-dish rotation curves, velocity dispersions and P-V diagrams for NGC 2403, NGC 2903, NGC 3198 and NGC 5055 . . . . .	63
<i>Fig. 3.9</i>	Testing <sup>3D</sup> BAROLO: effect of spatial resolution (3D vs 2D) . . . . .	65
<i>Fig. 3.10</i>	Testing <sup>3D</sup> BAROLO: effect of inclination angle . . . . .	66
<i>Fig. 3.11</i>	Testing <sup>3D</sup> BAROLO: effect of signal-to-noise ratio . . . . .	67
<b>Chapter 4: Gas accretion from minor mergers in local spiral galaxies</b>		<b>69</b>
<i>Fig. 4.1</i>	Sketch of the parabolic orbit approximation . . . . .	73
<i>Fig. 4.2</i>	HI mass distribution of main galaxies and detected satellites . . . . .	76
<i>Fig. 4.3</i>	Examples of multiple systems detected in the WHISP sample . . . . .	78
<i>Fig. 4.4</i>	Distance distributions of detected satellites . . . . .	79
<i>Fig. 4.5</i>	Gas accretion rates vs star formation rates for spiral galaxies in the WHISP sample . . . . .	81
<i>Tab. 4.6</i>	Detected companions of spiral galaxies in the WHISP sample . . . . .	88
<i>Tab. 4.7</i>	Properties of main galaxies in the WHISP sample . . . . .	91
<b>Chapter 5: Kinematics of high-<i>z</i> galaxies</b>		<b>97</b>
<i>Fig. 5.1</i>	HST images and moment maps for our sample of normal star-forming galaxies at $z \sim 1$ . . . . .	101
<i>Fig. 5.2</i>	Channel maps of the data and the models for <i>zcos_z1_692</i> , a disk galaxy at $z = 0.93$ . . . . .	104
<i>Fig. 5.3</i>	P-V diagrams along the major axis of the data and the models for our galaxy sample . . . . .	105
<i>Fig. 5.4</i>	Rotation curves and velocity dispersions of high- <i>z</i> galaxies . . . . .	106
<i>Fig. 5.5</i>	Tully-Fisher relation at $z \sim 1$ . . . . .	107
<i>Fig. 5.6</i>	Evolution of gas velocity dispersion throughout cosmic time . . . . .	108
<i>Tab. 5.7</i>	Sample of galaxies at $z \sim 1$ . . . . .	109